

Hybrid model of proton structure functions

S. A. Kulagin^{1,*} and V. V. Barinov^{2,1,†}

¹*Institute for Nuclear Research of the Russian Academy of Sciences, Moscow 117312, Russia*

²*Physics Department, Lomonosov Moscow State University, Leninskie Gory, Moscow 119991, Russia*

We develop a “hybrid” model of the proton inelastic structure functions applicable in a wide region of invariant mass of produced states W and invariant momentum transfer Q including deep inelastic scattering (DIS), nucleon resonance production as well as the region close to inelastic threshold. DIS is described in terms of the parton distributions together with higher-twist corrections from an available global QCD fit. The resonant part is addressed in terms of the Breit-Wiegner contributions from five states including the $\Delta(1232)$ resonance, the $N(1440)$ Roper resonance, and three effective resonances describing the second and third resonance regions. The couplings of the nucleon resonances to photon are described in terms of helicity amplitudes. The nonresonant background is addressed in terms of DIS structure functions smoothly extrapolated to low- W and low- Q values with the proper behavior at the real photon limit $Q^2 = 0$ as well as near the inelastic threshold. We independently treat the transverse F_T and the longitudinal F_L structure function and fix the model parameters from a global analysis of the world hydrogen electroproduction and photoproduction cross-section data. We demonstrate a very good performance of the model by comparing our predictions with data on differential cross sections and the structure functions F_2 and $R = F_L/F_T$.

I. INTRODUCTION

The rate of various high-energy processes is driven by the parton distribution functions (PDFs), which are universal (process-independent) characteristics of the target at high invariant momentum transfer Q and are normally determined from global QCD analyses of high-energy data (for a recent review see [1, 2]). As the values of Q and W decrease various subleading effects, such as higher-order perturbative QCD corrections in the strong coupling constant, higher-twist power corrections and/or target mass corrections become increasingly important [1]. In a strong coupling regime at a low scale $Q \lesssim 1$ GeV available methods of perturbative QCD, the twist expansion, and the methods based on the renormalization group equations are not applicable and the validity of the partonic picture becomes controversial.

In a low- Q and also low- W region, $W < 2$ GeV, the lepton-nucleon inelastic scattering is dominated by production of nucleon resonance states. Unlike deep inelastic scattering (DIS), which is described in terms of the partonic picture and PDFs, the resonance region is usually addressed in terms of hadronic degrees of freedom. Starting from Ref. [3], a number of phenomenological analyses are available [4–6], in which the resonance production is considered as a superposition of the Breit-Wiegner poles and the photon-resonance couplings are described in terms of helicity amplitudes (for a recent review see [7]). The resonant inelastic scattering is accompanied by non-resonant background processes whose rate rises with W . In the region of $W > 2$ GeV they dominate the cross sections. In available analyses the background contributions are often treated empirically in a limited region of W and

Q [3–5]. Also other approaches are discussed such as the phenomenology based on a Regge-dual model [8] and neural network analyses [9].

In this paper we develop a combined (hybrid) approach to the proton inelastic structure functions (SFs) spanning both the resonant production and the DIS region. We address both the transverse (F_T) and longitudinal (F_L) SFs, which form a complete set of functions required to compute the spin-independent cross sections. In this work we are motivated by the fact that a quantitative model of this kind, thoroughly verified with experimental data, could be applied in various studies, in which the integration over the full spectrum of intermediate states and momentum transfer is required. In this context we mention the studies of the Bloom-Gilman quark-hadron duality [10], evaluation of the photon content in the proton [2, 11], the studies of nuclear effects in a resonance-DIS transition region [12], and calculation of the total neutrino cross sections [13]. It should be also remarked that in the energy region of modern long-baseline neutrino experiments the neutrino-nuclear interaction is dominated by excitation of nucleon resonances together with low- W DIS and a reliable modeling of corresponding cross sections is needed to reduce systematic uncertainties and for a correct interpretation of experimental results [14].

It is well known that the experimental spectrum of inelastic electron-nucleon scattering for $W < 2$ GeV and $Q < 2$ GeV has three pronounced resonance structures. The first resonance region is due to excitation of $\Delta(1232)$ resonance state, while the other two involve a superposition of a number of individual resonance states. In this paper the resonance contribution to SFs is addressed in terms of five Breit-Wiegner resonances: the $\Delta(1232)$ resonance state, the $N(1440)$ Roper resonance state, and three more heavy resonances describing the second and the third resonance regions. We treat the resonances heavier than the Roper state as *effective* Breit-Wiegner resonances which incorporate contributions from a num-

* kulagin.physics@gmail.com

† barinov.vvl@gmail.com

ber of excited nucleon states. Nevertheless, the effective resonances are assigned particle quantum numbers, such as spin and mass, and their couplings to photons are described in terms of helicity amplitudes. This choice on the number of effective resonances is motivated by a balance between the accuracy of description of cross-section data and the overall stability of our analysis of world cross-section data.

The resonance contributions vanish at sufficiently high values of W and in this region the cross sections are dominated by nonresonant background processes which eventually turn into DIS at high values of invariant momentum transfer Q . Motivated by this we model the nonresonant background in the resonance region in terms of the DIS structure functions properly continued into a low- W and low- Q^2 region down to photoproduction limit $Q^2 = 0$. To this end we develop an extrapolation method allowing to smoothly match the DIS SFs at a scale $Q = Q_0$. This scale defines the onset of a low- Q region and its value is optimized from analysis of cross-section data. Our extrapolation method ensures that F_T/Q^2 matches the photoproduction cross section in the $Q^2 \rightarrow 0$ limit and also provides vanishing $R = F_L/F_T$ in this limit.

Inelastic scattering off the nucleon is characterized by the presence of the pion production threshold at $W = M + m_\pi$ with M and m_π the proton and the pion mass, respectively. The resonant contributions explicitly respect the inelastic threshold behavior, as discussed below in Sec. II B. Our method to compute the background contributions also ensures that they vanish smoothly at the inelastic production threshold. We also note in this context that the inelastic threshold effect should impact DIS SF studies at high Bjorken $x \approx 1$ in terms of PDFs. The threshold effect is also relevant for calculation of nuclear corrections in this region [12].

The parameters of our model, such as the resonance masses, widths, parameters of helicity amplitudes, the transition scale Q_0 , as well as the parameters responsible for extrapolation into a low- W and low- Q region, are determined from a global fit to the world data on the hydrogen electroproduction differential cross section and the total photoproduction cross section off hydrogen. We recall that our model smoothly matches the DIS region and we use the results of a global QCD analysis from Refs. [15, 16] in order to compute the background contributions in the resonance region. For this reason we do not need to refit DIS data and we focus on the studies of the resonance and DIS transition region. After fixing the model parameters in a fit to cross-section data, we verify our predictions on F_2 and R by comparing with available measurements.

The article is organized as follows. In Sec. II we outline the basic theory framework to be used in this study. In Sec. II A we summarize basic information on DIS SFs required in our analysis, while in Sec. II B we address the derivation of the resonance SFs in terms of the Breit-Wigner poles and helicity amplitudes. In Sec. III we

discuss in detail our model of the resonance and background contributions. In Sec. IV we describe the details of data analysis. Our results and observations are discussed in Sec. V and we summarize in Sec. VI. Supplemental Material [17] provides a detailed comparison of our predictions with cross-section data from various experiments used in our analysis.

II. FRAMEWORK

The scattering of charged leptons by hadrons in the leading order in the electromagnetic coupling constant $\alpha = e^2/(4\pi)$ is determined by the standard one-photon exchange process. In inclusive scattering, the final hadronic state is not detected and the differential cross section is given by the hadronic tensor $W_{\mu\nu}$ (see, e.g., Ref. [18]):

$$W_{\mu\nu}(p, q) = \frac{1}{8\pi} \sum_{\lambda, n} (2\pi)^4 \delta(p + q - p_n) \times \langle P, \lambda | J_\mu^{\text{em}}(0) | n \rangle \langle n | J_\nu^{\text{em}}(0) | P, \lambda \rangle, \quad (1)$$

where J_μ^{em} is the electromagnetic current, the sum is taken over all final hadronic states n , and p is the proton four-momentum and q is four-momentum transfer. We do not consider the polarization effects and explicitly average over proton polarization λ . Only the symmetric part of the hadronic tensor contributes to the spin-averaged cross section. Because of the current conservation, time reversal invariance, and parity conservation, the symmetric hadronic tensor has only two independent Lorentz structures which are usually written as follows:

$$W_{\mu\nu}(p, q) = \left(\frac{q_\mu q_\nu}{q^2} - g_{\mu\nu} \right) F_1 + \frac{F_2}{p \cdot q} \left(p_\mu - q_\mu \frac{p \cdot q}{q^2} \right) \left(p_\nu - q_\nu \frac{p \cdot q}{q^2} \right), \quad (2)$$

where $F_{1,2}$ are the Lorentz-invariant dimensionless structure functions. The structure functions depend on two independent Lorentz-invariant variables. In the DIS region, the Bjorken variable $x = Q^2/(2p \cdot q)$ and the four-momentum transfer squared $Q^2 = -q^2$ are used.¹ In the discussion of the resonance and transition region, we will also consider the structure functions as a function of the invariant mass of produced states,

$$W^2 = M^2 + Q^2(1/x - 1). \quad (3)$$

The differential cross section in terms of x and Q^2

¹ For the particle state we use the normalization $\langle p | p' \rangle = 2p_0(2\pi)^3 \delta(\mathbf{p} - \mathbf{p}')$, where p_0 is the energy of the particle. We also use the standard notation of the scalar product of two four-vectors $a \cdot b = a_0 b_0 - \mathbf{a} \cdot \mathbf{b}$.

variables reads

$$\frac{d^2\sigma}{dx dQ^2} = \frac{4\pi\alpha^2}{xQ^4} \left[xy^2 \left(1 - \frac{2m_l^2}{Q^2} \right) F_1 + \left(1 - y - \frac{M^2 x^2 y^2}{Q^2} \right) F_2 \right], \quad (4)$$

where m_l is the lepton mass and $y = p \cdot q / p \cdot k$ is the inelasticity parameter (here k is the four-momentum of the incoming lepton). The variable y is not independent but is related to x and Q^2 as $xy = Q^2 / (2p \cdot k)$. In the laboratory frame, the differential cross section is measured as a function of scattering angle and the outgoing lepton energy E' , and is related to Eq. (4) as

$$\frac{d^2\sigma}{d\Omega dE'} = \frac{x E'}{\pi y} \frac{d^2\sigma}{dx dQ^2}. \quad (5)$$

The structure functions $F_{1,2}$ can be related to the virtual photon helicity cross sections by projecting the hadronic tensor onto the photon polarization vectors of definite helicity $\varepsilon_\mu^{(m)}$ with $m = \pm 1, 0$. It is convenient to chose the z -axis along the momentum transfer, $q_z = |\mathbf{q}|$. Then we have

$$\varepsilon^{(\pm 1)} = (0, 1, \pm i, 0) / \sqrt{2}, \quad (6a)$$

$$\varepsilon^{(0)} = (q_z, \mathbf{0}_\perp, q_0) / Q. \quad (6b)$$

where $Q = \sqrt{Q^2}$. The polarization vectors $\varepsilon^{(+1)}$ and $\varepsilon^{(-1)}$ describe the transversely polarized states with photon helicity $m = +1$ and $m = -1$, while the vector $\varepsilon^{(0)}$ corresponds to the longitudinally polarized virtual photon. Note that the polarization vectors $\varepsilon^{(m)}$ are orthogonal to the photon momentum, $\varepsilon^{(m)} \cdot q = 0$, and normalized as $\varepsilon^{(0)} \cdot \varepsilon^{(0)} = 1$ and $\varepsilon^{(m)*} \cdot \varepsilon^{(m)} = -1$ for $m = \pm 1$, where ε^* is the complex conjugate. The transverse, F_T , and the longitudinal, F_L , SFs can be found by contracting the hadronic tensor, Eq. (1), with the photon polarization vectors, Eq. (6). We have

$$F_T = x \sum_{m=\pm 1} \varepsilon_\mu^{(m)*} W_{\mu\nu} \varepsilon_\nu^{(m)} = 2xF_1, \quad (7)$$

$$F_L = 2x \varepsilon_\mu^{(0)} W_{\mu\nu} \varepsilon_\nu^{(0)} = \gamma^2 F_2 - F_T, \quad (8)$$

where $\gamma^2 = 1 + 4x^2 M^2 / Q^2$. The transverse and longitudinal cross sections in terms of Eq. (7) and (8) can be written as follows (see, e.g., Ref. [18]):

$$\sigma_{T,L} = \frac{4\pi^2 \alpha F_{T,L}}{(1-x)Q^2}. \quad (9)$$

Note that the definition of the virtual photon flux is somewhat uncertain. In Eq. (9) we assume the virtual photon flux equals the real photon one with the condition that the mass of produced hadronic states W is the same for the real and virtual photon [18].

Let us briefly discuss the real photon limit. To this end it is convenient to consider the SF as a function of W^2 and

Q^2 . Owing to conservation of electromagnetic current, the longitudinal cross section vanishes at $Q^2 = 0$. This in turn suggests F_L vanishing faster than Q^2 as $Q^2 \rightarrow 0$. On the other hand, the cross section σ_T for transverse virtual photons goes to the total photoproduction cross section in this limit:

$$\sigma_\gamma(W) = 4\pi^2 \alpha \lim_{Q^2 \rightarrow 0} F_T(W^2, Q^2) / Q^2. \quad (10)$$

For this reason the ratio $F_T(W^2, Q^2) / Q^2$ (as well as F_2 / Q^2) is finite at $Q^2 \rightarrow 0$ and fixed W . We use Eq. (10) to constrain a low- Q behavior of our model in Sec. III.

A. Deep inelastic scattering

In QCD, a common framework to address DIS is the operator product expansion (OPE), a procedure producing the power series in Q^{-2} (twist expansion). In the leading order of this expansion, i.e., in the leading twist (LT), SFs factorize into a convolution of the coefficients functions, describing quark-gluon interaction at a hard scale Q , and the parton distribution functions [19]. In the lowest order in QCD coupling constant α_s the coefficient functions are simply the quark charges squared, and SFs are given in terms of PDFs according to the celebrated quark-parton model. The gluon PDF contributes to SFs in higher orders in α_s through quark-gluon radiation processes. For more detailed discussion see, e.g., Ref. [1].

The power corrections in Q^{-2} can be of two different types: contributions from higher-twist (HT) operators describing quark-gluon correlations and correction arising from a finite nucleon mass (target mass correction, or TMC). Summarizing, we write the proton SF as follows

$$F_i^{\text{DIS}}(x, Q^2) = F_i^{\text{TMC}}(x, Q^2) + H_i(x) / Q^2, \quad (11)$$

where $i = T, L$ and the superscript TMC labels the LT SF corrected for the target mass effect while the functions H_i describe the dynamical twist-4 contribution (for brevity, we suppress explicit notation to the twists higher than 4).

The PDFs are usually determined in a global QCD analysis of high-energy data including DIS, muon pair production in proton-proton collisions (DY), and W/Z boson production at colliders (for more detail we refer to Refs. [1, 2]). In this study we use the proton PDFs from a global QCD fit of Refs. [15, 16], which was performed to the next-to-next-to-leading-order (NNLO) approximation in the QCD coupling constant. Although updated PDF analyses are available, such as Refs. [20, 21] as well as the other results discussed in Refs. [1, 2], which include the most recent LHC data and thus better constrain the low- x region, we use the PDFs of Refs. [15, 16] as the base. We are motivated by the fact that the analysis of Ref. [15] applies the cuts $Q > 1$ GeV and $W > 1.8$ GeV and thus includes low- Q data.² Along with PDFs the

² SFs of Ref. [15] are available at significantly lower values of Q^2

analysis of Refs. [15, 16] provides the determination of H_i functions describing twist-4 terms. In this study we address the resonance and DIS transition region and for this reason a low- Q PDF fit is preferred over recent PDF analyses [1, 20], which utilize the more stringent cut $Q^2 > 2.5 \text{ GeV}^2$. We also comment that the proton and the neutron SFs of Ref. [15] show a very good performance in analysis of the nuclear EMC effect in Refs. [22, 23] as well as in the interpretation of a recent measurement of F_2^n/F_2^p [24].

TMC is accounted for within the OPE framework of Ref. [25]. Similar TMC was used in analyses of Refs. [15, 16]. It should be remarked that the TMC procedure of Ref. [25] violates the inelastic threshold behavior of the SFs, leading to nonzero values at $x \geq 1$ (see, e.g., the discussion in Ref. [22]). The region of large Bjorken x corresponds to low values of W . By increasing the value of x at some point we enter the resonance region even at high values of Q^2 and thus leave the region of applicability of an OPE-based description. In our analysis below, we use DIS SFs in a safe region of $W^2 > 4 \text{ GeV}^2$ and $Q^2 > 2 \text{ GeV}^2$. To calculate nonresonant background at low- W and low- Q values we use extrapolated DIS SFs as discussed in Sec. III.

B. Excitation of nucleon resonances

In the region of $W < 2 \text{ GeV}$ and for a low momentum transfer $Q \lesssim 2 \text{ GeV}$ the inelastic cross section is dominated by excitation of nucleon resonance states. Their contribution to the hadronic tensor Eq. (1) can be written as

$$W_{\mu\nu}^{\text{Res}} = \frac{1}{4} \sum_{R,\lambda,\lambda'} \delta(W^2 - M_R^2) \times \langle P, \lambda | J_\mu^{\text{em}}(0) | R, \lambda' \rangle \langle R, \lambda' | J_\nu^{\text{em}}(0) | P, \lambda \rangle, \quad (12)$$

where the sum is taken over the nucleon resonant states and M_R is the mass of the corresponding state. We first consider narrow resonance states with zero width; the effect of a finite width will be discussed below. In Eq. (12) we also explicitly sum over the polarization λ' of an intermediate state and average over the proton polarization λ .

We discuss in detail the derivation of the structure functions F_T and F_L from hadronic tensor (12) in terms of helicity amplitudes thus updating existing studies [5, 6]. F_T and F_L are given by contracting the hadronic tensor (12) with the corresponding photon polarization vector by Eq. (7) and (8). The matrix elements of electromagnetic current can be described in terms of helicity amplitudes [3,

7, 26]:

$$\langle R, h' | \varepsilon^{(m)} \cdot J^{\text{em}}(0) | P, h \rangle = H_{h'h}^m, \quad (13)$$

where h' and h are the helicities of the resonance state R and the proton, respectively (for brevity, we suppress explicit notation of the dependence of helicity amplitudes on the resonance R). Because helicity is conserved, $h' = h + m$. In the parity transformation the helicity changes its sign, and, because of symmetry under parity transformation, we have the relation $H_{-h'-h}^{-m} = H_{h'h}^m$ (see also Ref. [3]). We consider the helicity amplitudes in the center-of-mass frame (c.m.) and chose the spin quantization axis along the photon momentum. Then the proton helicity h has the sign opposite to its polarization, as the proton momentum balances the photon momentum, and the helicity h' of the resonance state R corresponds to its polarization.

Consider Eq. (13) for the proton polarization $\lambda = 1/2$ and respectively $h = -1/2$. The helicity amplitudes can be related to the standard electrocouplings $A_{1/2}$, $A_{3/2}$, and $S_{1/2}$, which are commonly used to describe electroexcitation of the resonance states (see, e.g., Ref. [7]):

$$H_{\frac{1}{2}, -\frac{1}{2}}^{+1} = c_R A_{1/2}(Q^2), \quad (14)$$

$$H_{-\frac{3}{2}, -\frac{1}{2}}^{-1} = c_R A_{3/2}(Q^2), \quad (15)$$

$$H_{-\frac{1}{2}, -\frac{1}{2}}^0 = c_R S_{1/2}(Q^2)(Q/|\mathbf{q}|_{\text{cm}}), \quad (16)$$

where $|\mathbf{q}|_{\text{cm}}$ is the photon momentum in the c.m. frame.³ The normalization factor c_R can be determined by requiring the electromagnetic decay width $\Gamma_R^\gamma(R \rightarrow P\gamma)$ to be [7, 27]

$$\Gamma_R^\gamma = \frac{2K_R^2 M}{\pi(2S_R + 1)M_R} \left(|A_{1/2}^R(0)|^2 + |A_{3/2}^R(0)|^2 \right), \quad (17)$$

where we assume averaging over the resonance polarization and summing over photon polarization, S_R is the resonance spin, and $K_R = (M_R^2 - M^2)/(2M_R)$ is the energy of a real photon in the c.m. frame needed to produce the state with the mass M_R . Using Eq. (14) and (15) we have

$$c_R^2 = \frac{M(M_R^2 - M^2)}{\pi\alpha}. \quad (18)$$

Note that the electromagnetic current in Eq. (1) is normalized such that the electric charge $e = 1$. By definition the electric charge is absorbed in the amplitudes $A_{1/2}$, $A_{3/2}$, $S_{1/2}$, and for that reason we have α in the denominator in Eq. (18).

We now apply the results of the present discussion to compute the resonant contribution to F_T and F_L in terms

owing an extrapolation procedure, which is different from that discussed below.

³ Note that in the c.m. frame $|\mathbf{q}|_{\text{cm}}$ is also the magnitude of the proton momentum. For completeness, $|\mathbf{q}|_{\text{cm}}^2 = E_{\text{cm}}^2 - M^2$, where $E_{\text{cm}} = (W^2 + Q^2 + M^2)/(2W)$ is the proton c.m. energy.

of the amplitudes $A_{1/2}$, $A_{3/2}$ and $S_{1/2}$. From Eq. (7) and (8) we have

$$F_T^{\text{Res}} = \frac{xM}{2\pi\alpha} \sum_R \delta(W^2 - M_R^2)(M_R^2 - M^2) \times \left(|A_{1/2}^R(Q^2)|^2 + |A_{3/2}^R(Q^2)|^2 \right), \quad (19)$$

$$F_L^{\text{Res}} = \frac{xM}{\pi\alpha} \sum_R \delta(W^2 - M_R^2)(M_R^2 - M^2) \times (Q^2/|\mathbf{q}_{\text{cm}}|^2) |S_{1/2}^R(Q^2)|^2, \quad (20)$$

where x is the Bjorken variable and the sum is taken over the resonance states.

Let us now discuss the effect of finite resonance width in Eq. (12) in some more detail. Following a traditional approach, we replace $\delta(W^2 - M_R^2)$ with the standard Breit-Wigner factor:

$$\delta(W^2 - M_R^2) \rightarrow \frac{1}{\pi} \frac{M_R \Gamma_R}{(W^2 - M_R^2)^2 + M_R^2 \Gamma_R^2}, \quad (21)$$

where Γ_R is the resonance total width.

The $\Delta(1232)$ resonance width is entirely due to the πN decay channel. For heavier resonance states there are also other decay modes. In our analysis we will assume that any resonance state R in Eq. (19) and (20) decays either in πN , ηN , or $2\pi N$ channels:

$$\Gamma_R = \beta_R^\pi \Gamma_R^\pi + \beta_R^\eta \Gamma_R^\eta + \beta_R^{2\pi} \Gamma_R^{2\pi}, \quad (22)$$

with $\beta_R^{\pi,\eta,2\pi}$ the corresponding branching fractions.

Generally, the resonances can be excited off the resonance pole, $W^2 \neq M_R^2$, and in Eq. (12) one has to consider off-mass-shell effects on the resonance parameters. In particular, the resonance width becomes a function of running mass, $\Gamma_R = \Gamma_R(W)$. Indeed, near the inelastic threshold $W_{\text{th}} = M + m_\pi$ the cross section should vanish that in turn requires vanishing resonance width. On the other hand, $\Gamma_R(W)$ increases with W as the phase space available for the resonance decay increases. In order to account for this effect, we parametrize the energy dependence of $\Gamma_R(W)$ following Ref.[3]:

$$\Gamma_R^\pi = \Gamma_R^0 \left(\frac{p_\pi(W)}{p_\pi(M_R)} \right)^{2L+1} \left(\frac{p_\pi(M_R)^2 + X_R^2}{p_\pi(W)^2 + X_R^2} \right)^L, \quad (23)$$

where Γ_R^0 is the intrinsic resonance width, $p_\pi(W)$ is the meson c.m. momentum in the decay $R \rightarrow \pi P$ of the resonance with mass W , L is angular momentum of the resonance, and X_R is a phenomenological parameter (damping factor). The parametrization of the ηN decay mode is similar to Eq. (23) with p_η the η meson c.m. momentum. For the 2π decay mode we use [7]

$$\Gamma_R^{2\pi} = \Gamma_R^0 \left(\frac{p_{2\pi}(W)}{p_{2\pi}(M_R)} \right)^{2L+4} \left(\frac{p_{2\pi}(M_R)^2 + X_R^2}{p_{2\pi}(W)^2 + X_R^2} \right)^{L+2}, \quad (24)$$

where $p_{2\pi}$ is effective two-pion momentum in c.m. frame which is computed similarly to p_π but replacing m_π with $2m_\pi$. Apparently, $p_{2\pi} = 0$ below the 2π production threshold and $p_\eta = 0$ below the η meson production threshold.

Also the γPR vertex, or helicity amplitudes, acquire W dependence in the resonance off-pole region. We phenomenologically account for the off-shell effect following Ref.[3] with the factor f_R^γ :

$$f_R^\gamma(W) = \frac{K^2}{K_R^2} \frac{K_R^2 + X_R^2}{K^2 + X_R^2}, \quad (25)$$

where $K = K(W) = (W^2 - M^2)/(2W)$ is the equivalent photon c.m. momentum, $K_R = K(M_R)$ and X_R is the same damping parameter as in Eq. (23) and (24). At the resonance pole $f_R^\gamma(M_R) = 1$.

Summarizing, we have for the resonant contribution to F_T and F_L :

$$F_T^{\text{Res}} = \frac{xM}{\pi^2\alpha} \sum_R \frac{M_R^2 \Gamma_R K_R f_R^\gamma(W)}{(W^2 - M_R^2)^2 + M_R^2 \Gamma_R^2} \times \left(|A_{1/2}^R(Q^2)|^2 + |A_{3/2}^R(Q^2)|^2 \right), \quad (26)$$

$$F_L^{\text{Res}} = \frac{2xM}{\pi^2\alpha} \sum_R \frac{M_R^2 \Gamma_R K_R f_R^\gamma(W)}{(W^2 - M_R^2)^2 + M_R^2 \Gamma_R^2} \times (Q^2/|\mathbf{q}_{\text{cm}}|^2) |S_{1/2}^R(Q^2)|^2, \quad (27)$$

where we sum over the resonance states and $\Gamma_R = \Gamma_R(W)$ is the total resonance width by Eq. (22). For completeness we also present the corresponding contributions to the virtual photon cross section σ_T and σ_L by Eq. (9). Using Eq. (26) and (27) and also the relation $Q^2(1-x) = x(W^2 - M^2)$ we have

$$\sigma_T^{\text{Res}} = \frac{2M}{W} \sum_R \frac{M_R^2 \Gamma_R (K_R/K) f_R^\gamma(W)}{(W^2 - M_R^2)^2 + M_R^2 \Gamma_R^2} \times \left(|A_{1/2}^R(Q^2)|^2 + |A_{3/2}^R(Q^2)|^2 \right), \quad (28)$$

$$\sigma_L^{\text{Res}} = \frac{4M}{W} \sum_R \frac{M_R^2 \Gamma_R (K_R/K) f_R^\gamma(W)}{(W^2 - M_R^2)^2 + M_R^2 \Gamma_R^2} \times (Q^2/|\mathbf{q}_{\text{cm}}|^2) |S_{1/2}^R(Q^2)|^2. \quad (29)$$

The explicit parametrization of the Q^2 dependence of the helicity amplitudes entering Eq. (26) to (29) is discussed in Sec. III.

It should be commented that the off-shell continuation of amplitudes for a particle with finite width is not unique. In order to illustrate this statement, we first observe that in the right side of Eq. (19) and (20) M_R can be replaced with W and then the factor $W^2 - M^2$ can be taken out of the sum over the resonance states. On the other hand, this operation does not commute with Eq. (21) and the result would depend on the order of these two operations. We will proceed with Eq. (26) and (27) and fix phenomenological parameters there from a fit to the cross section data described in Sec. IV.

III. DESCRIPTION OF THE MODEL

The full structure functions include contributions from both, the resonance states discussed in Sec. II B, and non-resonantly produced continuum states [background (BG) contributions]:

$$F_i = F_i^{\text{Res}} + F_i^{\text{BG}}, \quad (30)$$

where $i = T, L$. In what follows it will be convenient to consider the structure functions as a function of Q^2 and W^2 . From Eq. (3) the Bjorken variable $x = Q^2/(Q^2 + W^2 - M^2)$. While the resonance part dominates in the region of low W , BG contribution rises with W and prevails for $W > 2$ GeV. If W and Q are sufficiently high then BG contributions are driven by DIS, $F_i^{\text{BG}} \rightarrow F_i^{\text{DIS}}$. We will use this simple observation to also model BG contributions in the whole region of W and Q with suitable extrapolation of the DIS structure functions outside the region of their applicability.

A. Resonance contributions

We apply Eq. (26) and (27) to compute the resonant contribution to the transverse and the longitudinal SFs. Note that the unpolarized scattering is not sensitive to individual amplitudes $A_{1/2}$ and $A_{3/2}$ and only their quadrature sum is relevant. For this reason, for each of the resonance state in Eq. (26) and (27), we discuss the average amplitude $A(Q^2)$ defined as

$$|A(Q^2)|^2 = |A_{1/2}(Q^2)|^2 + |A_{3/2}(Q^2)|^2. \quad (31)$$

In order to describe the observed resonant inclusive spectra, we include five resonant contributions in Eq. (26) and (27). The first resonance region is described by a well separated $\Delta(1232)$ resonance state. The second and third resonance regions are described in terms of the $N(1440)$ Roper resonance and three more heavier states R_1 , R_2 , and R_3 . As outlined in Sec. I, we treat these states as effective Breit-Wigner resonances incorporating contributions from a number of individual excited-nucleon states. The relevant resonance parameters are listed in Table I. The parameter values are determined from a combined fit to the hydrogen inclusive electroproduction differential cross-section data and photoproduction cross-section data, as described in Sec. IV.

To parametrize Q^2 dependence of the transverse and the longitudinal amplitudes in Eq. (26) and (27) we use the following model:

$$A(Q^2) = (a_1 + a_2 Q^2) / (1 + a_3 Q^2)^{a_4} \quad (32)$$

$$S_{1/2}(Q^2) = (c_1 + c_2 Q^2) \exp(-c_3 Q^2) \quad (33)$$

The determination of parameter values in Eq. (32) and (33), as well as other model parameters entering Eq. (26) and (27), is discussed in Sec. IV.

TABLE I. The best fit values for the mass M_R , the intrinsic width Γ_R , the angular momentum L , the damping parameter X_R , and the decay branching fractions β for each of the resonant state. The dimensional parameters are in GeV units. The estimate of the fit parameter uncertainty is given in parentheses in percent units.

	M_R	Γ_R	L	X_R	$\beta_{1\pi}$	$\beta_{2\pi}$	β_η
$\Delta(1232)$	1.2270(0.02)	0.1128(0.48)	1	0.0554(1.07)	1.00	0.00	0.00
$N(1440)$	1.4487(0.34)	0.4022(3.34)	1	0.1125(3.85)	0.65	0.35	0.00
R_1	1.5123(0.02)	0.0945(1.83)	2	0.4959(4.81)	0.75	0.25	0.00
R_2	1.5764(0.16)	0.5005(1.76)	0	0.3097(2.12)	0.15	0.85	0.00
R_3	1.7002(0.03)	0.1177(1.66)	2	0.2583(10.8)	0.15	0.60	0.25

B. Background contributions

In order to model BG contributions we first consider the extrapolation of DIS structure functions to low Q^2 . Note that the framework of Sec. II A applies for $Q > Q_0$ with the scale $Q_0 \sim 1$ GeV. Going into the region $Q < Q_0$, we consider extrapolation of DIS F_T and F_L from the scale Q_0^2 down to $Q^2 = 0$, taking into account the real photon limit [see the discussion after Eq. (9)]. Let us first discuss the function F_T which vanishes as Q^2 at $Q^2 \rightarrow 0$. From Eq. (10) the ratio F_T/Q^2 in the limit $Q^2 \rightarrow 0$ is given by the total photoproduction cross section $\sigma_\gamma(W)$. Taking this into account, we consider the following model for $0 \leq Q^2 \leq Q_0^2$:

$$F_T^{\text{Ext}}(W^2, t) = f_0 t + f_1 t^m + f_2 t^n, \quad (34)$$

where for Q^2 we use a more handy notation t , and f_0 , f_1 and f_2 are the functions of W , and we assume $m > 1$ and $n > 1$. Taking the limit $t \rightarrow 0$ and using Eq. (10) we have

$$f_0(W) = \sigma_\gamma(W) / (4\pi^2 \alpha). \quad (35)$$

The functions f_1 and f_2 are determined by requiring the smoothness of the extrapolation function by Eq. (34) at $t = t_0 = Q_0^2$; i.e., we require the continuity of the function and its first derivative at the DIS matching point. We have

$$f_1 = t_0^{-m} (n F_T^{\text{DIS}} - t_0 \partial_t F_T^{\text{DIS}} - (n-1) f_0 t_0) / (n-m), \quad (36)$$

$$f_2 = t_0^{-n} (m F_T^{\text{DIS}} - t_0 \partial_t F_T^{\text{DIS}} - (m-1) f_0 t_0) / (m-n), \quad (37)$$

where F_T^{DIS} and its derivative $\partial_t F_T^{\text{DIS}}$ are computed at $t = t_0$ for given W^2 . The exponents m and n controlling the transition to the low- t region are adjusted from the data analysis in Sec. IV. Note that both Eq. (36) and (37) have a pole at $n = m$. However, Eq. (34) is finite in the limit $n \rightarrow m$. Taking this limit we see that a low- t behavior is given by a combination of t^m and $t^m \ln t$ terms, and Eq. (34) can be written as follows:

$$F_T^{\text{Ext}} = f_0 t + (t/t_0)^m [F_T^{\text{DIS}} - f_0 t_0 + (m F_T^{\text{DIS}} - t_0 \partial_t F_T^{\text{DIS}} - (m-1) f_0 t_0) \ln(t/t_0)]. \quad (38)$$

In practice this is an important case, preferred by data as described in Sec. IV.

To extrapolate the longitudinal SF in the region $0 \leq t \leq t_0$ we use a model similar to Eq. (34) with $f_0 = 0$ as the longitudinal cross section vanishes for real photon:

$$F_L^{\text{Ext}}(W^2, t) = f_1' t^{m'} + f_2' t^{n'}. \quad (39)$$

The functions $f_{1,2}'(W)$ are fixed by requiring smoothness of the function Eq. (39) at $t = t_0$, similarly to the F_T case. On the functions f_1' and f_2' we obtain the equations similar to Eq. (36) and (37) with F_T replaced with F_L and $f_0 = 0$. The case $n' = m'$, which is preferred by our analysis in Sec. IV, reads

$$F_L^{\text{Ext}} = (t/t_0)^{m'} [F_L^{\text{DIS}} + (m' F_L^{\text{DIS}} - t_0 \partial_t F_L^{\text{DIS}}) \ln(t_0/t)]. \quad (40)$$

Note that in global QCD fits the PDFs are parameterized in the full region of the variable x ($0 < x < 1$) and for this reason the DIS structure functions by Eq. (11) can be computed in the full region of W . However, for $W < 2$ GeV, and therefore in the region of large x , the structure functions from global PDF fits are not directly constrained by data because low- W data are explicitly removed from the fits (for instance, the fit of Refs. [15, 20] applies the cut $W > 1.8$ GeV). It should be also recalled, that the target mass correction of Ref. [25] generates unphysical contributions at $x \geq 1$. Taking this into account, we address the low- W region in our model by introducing a correction factor B as follows:

$$F_i^{\text{BG}} = B_i(W^2) \begin{cases} F_i^{\text{DIS}}(W^2, Q^2) & \text{if } Q^2 \geq Q_0^2, \\ F_i^{\text{Ext}}(W^2, Q^2) & \text{if } Q^2 < Q_0^2, \end{cases} \quad (41)$$

where $i = T, L$ and F_i^{BG} is the corresponding background structure function, and F_T^{Ext} and F_L^{Ext} are given by Eq. (34) and (39). The factors B_T and B_L are responsible for extrapolation to the low- W region and in this study we assume them to be the functions of W only. The $B_{T,L}$ functions are positively defined and required to vanish at the pion production threshold $W \rightarrow W_{\text{th}} = M + m_\pi$. On the other hand, they rise with W and $B_{T,L} \rightarrow 1$ above the resonance region. In order to respect these requirements, we use the following model:

$$B = 1 - \exp(-b_1(W^2 - W_{\text{th}}^2)^{b_2}), \quad (42)$$

where for simplicity we suppress the explicit subscript $i = T, L$ for B . The parameters b_1 and b_2 , which are assumed to be positive, are adjusted from a fit to cross-section data in Sec. IV. We independently treat these parameters for F_T and F_L .

C. Real photon limit

In the limit of $Q^2 = 0$ the longitudinal cross section vanishes and the photoproduction cross section σ_γ is

given by Eq. (10). Note that σ_γ receives contributions from the resonance production process as well as from a nonresonant background scattering:

$$\sigma_\gamma(s) = \sigma_\gamma^{\text{Res}}(s) + \sigma_\gamma^{\text{BG}}(s), \quad (43)$$

where $s = W^2 = M^2 + 2ME_\gamma$ and E_γ is the photon energy in the target rest frame. The resonant part is given by the $Q^2 \rightarrow 0$ limit of Eq. (28) and we have

$$\sigma_\gamma^{\text{Res}}(s) = \frac{2M}{W} \sum_R \frac{M_R^2 \Gamma_R(K_R/K) f_R^\gamma(W)}{(s - M_R^2)^2 + M_R^2 \Gamma_R^2} |A_R(0)|^2, \quad (44)$$

where the notations are similar to those in Eq. (28).

Above the resonance region, $W > 2$ GeV, the total photoproduction cross section is dominated by nonresonant processes. At high energy, $s > 10$ GeV², available photoproduction data can be described to a high accuracy in terms of a Regge model fit [28] whose best fit result is

$$\sigma_\gamma^{\text{Regge}}(s) = 0.0598 s^{0.0933} + 0.1164 s^{-0.357} \text{ mb}. \quad (45)$$

Using this result we model the background cross section $\sigma_\gamma^{\text{BG}}$ in the full region of s by applying a correction function B_T by Eq. (42) to Eq. (45):

$$\sigma_\gamma^{\text{BG}}(s) = B_T(s) \sigma_\gamma^{\text{Regge}}(s). \quad (46)$$

Note that in this analysis we assume the correction function by Eq. (42) to be independent of Q^2 . For this reason the same function $B_T(s)$ can be applied to both, the photoproduction cross section and the structure function F_T . We further check this assumption in our analysis of data in Sec. IV.

IV. DATA SETS AND FIT

We adjust parameters of our model by fitting to world data on the differential cross section of inelastic electron scattering together with photoproduction cross section data off a hydrogen target. The data sets used in our analysis are listed in Table II and Table III. The electron beam energy of SLAC experiments [29, 31, 52–60] span the region from 2 to 20 GeV and the data cover a wide kinematical region including the resonance production and DIS, while the beam energy of JLab experiments [32–34, 36, 37, 61] was in the range from 1.15 to 5.5 GeV and their data cover the resonance and transition region. The kinematics as well as statistics coverage of electron cross section data sets are illustrated in the (W^2, Q^2) plane in Fig. 1. The photoproduction cross section data at $Q^2 = 0$ are listed in Table III.

Note that our hybrid model is designed to smoothly match the DIS region. For this reason we do not include in the fit DIS data sets from NMC [62], BCDMS [63], H1 [64], and ZEUS [65], which were included in a global QCD analysis of Ref. [15] whose PDFs and HT terms are used in our study.

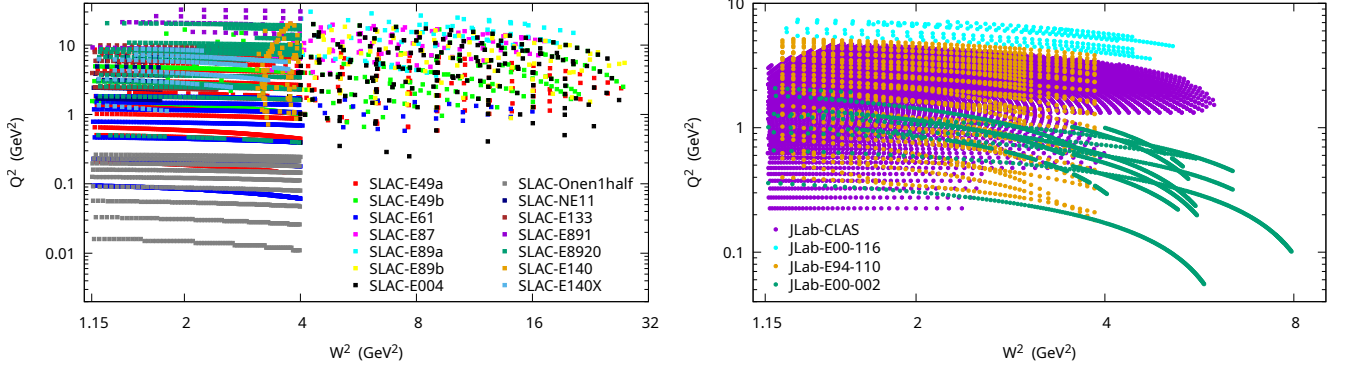


FIG. 1. The (W^2, Q^2) space populated by data points of the electroproduction data sets in Table II. The left (right) panel is for SLAC (JLab) experiments. The color code and legend for each of the data set are shown in the panels.

The parameters of our model are adjusted from minimization of the χ^2 function

$$\chi^2 = \sum_i (v_i^{\text{exp}} - v_i^{\text{model}})^2 / \sigma_i^2, \quad (47)$$

where the sum runs over the cross section data points used in our fit, and v_i^{exp} and v_i^{model} are the corresponding experimental and model values, and σ_i^2 is the experimental uncertainty squared, for which we take the quadrature sum of statistical and systematic error. We use data from Tables II and III as provided with no attempt to adjust overall normalization of particular data sets.

We use the MINUIT program [66] to minimize χ^2 and thus determine the parameters of our model. In preliminary trials we had 68 free parameters including the masses, widths, orbital momenta, damping parameters, and the branching fractions of resonance states in Table I; the parameters a_i and c_i describe the resonance amplitudes by Eq. (32) and (33), the parameters b_i are for the nonresonant background in Eq. (42) for transverse and longitudinal channels, and the scale parameter Q_0 as well as the parameters m and n drive the Q^2 dependence of extrapolated structure functions in Eq. (38) and (40).

An iterative procedure was applied to find the best fit model parameters. We first addressed the total photoproduction cross section data at $Q^2 = 0$ in Table III. This allowed us to determine some of the model parameters, in particular the resonance masses and widths, the normalization of resonance helicity amplitudes $|A(0)| = a_1$, and the parameters of the B_T function. Those parameters were then used as input for a further combined fit including both the photoproduction and electroproduction cross-section data from Tables II and III. By studying the photoproduction cross section we also tried to optimize the angular momenta of effective resonances together with their branching fractions, which then were fixed to the values listed in Table I.

In a combined fit to electroproduction and photoproduction data we had a number of sequential iterations. In initial trials we kept the resonance parameters fixed, thus

performing adjustment of the background parameters b_i as well as the exponents m and n controlling low- Q behavior of the structure functions (see Sec. IIIB). Then we performed the adjustment of the resonance parameters with the background fixed. This allowed us to study correlations between the parameters and also to locate the parameters to which the fit is most (least) sensitive.

In the course of our analysis we also observed that the fit prefers the $n \rightarrow m$ limit on the exponents describing extrapolation of the structure functions (see Sec. IIIB). We then fixed $n = m$ for both the transverse and the longitudinal SFs. Note that the exponent m is treated independently for F_T and F_L .

We also performed the studies aiming to optimize the parameter $t_0 = Q_0^2$, the scale from which we start extrapolating the DIS structure functions down to $Q^2 = 0$ (see Sec. IIIB). Note that our background DIS SFs are constrained by data for $Q^2 > 1 \text{ GeV}^2$ [15, 16]. Our fit prefers $t_0 = 1 \text{ GeV}^2$ resulting in a minimum of global χ^2 . However, the low- Q extrapolation starting from $t_0 = 1 \text{ GeV}^2$ following the method of Sec. IIIB results in $F_L < 0$ for high values of W and $Q^2 < 1 \text{ GeV}^2$ (effectively for $x < 0.01$) owing to a negative contribution from the derivative term in Eq. (40). Raising the extrapolation scale t_0 allows us to reduce the impact of this derivative term. We found that $t_0 = 2 \text{ GeV}^2$ results in a stable behavior of extrapolated F_L at low values of x and Q^2 . Note also that higher value of t_0 allows us to reduce uncertainties in evaluating the DIS SF by Eq. (11) at this scale.

It should be also commented that our fit results in numerically small values of the longitudinal parameters $c_1(\text{Roper})$, $c_1(R_2)$, $c_2(\Delta)$, $c_2(R_2)$, $c_2(R_3)$. On the final step we set these parameters to 0 as indicated in Table V. Also, our preliminary fits prefer the numerical value of the m_L exponent close to 1. Note that for the reason of vanishing $R = F_L/F_T \rightarrow 0$ at $Q^2 \rightarrow 0$, the value of the exponent m_L must be $m_L > 1$. In the final fit trial we also fixed $m_L = 1.1$, thus leaving 49 fit parameters.

Our fit results in the minimum of $\chi^2 = 27785.77$ for

TABLE II. Hydrogen electroproduction cross-section data sets used in our analysis. Listed are the experiments with corresponding number of data points (NDP) and kinematics coverage. The values of Q^2 and W^2 are in GeV^2 units. The cut $W^2 > 1.16 \text{ GeV}^2$ was applied. The “DIS” label indicates data which are mostly in the DIS region while the “RES” label is for data samples which are mostly in the resonance region. The last two columns are the values of χ^2 normalized per NDP computed, respectively, in our model and in the model of Ref. [5], for comparison (the symbol “N/A” indicates that the model of Ref. [5] is not applicable for kinematics reason).

Data set ^a	NDP	Q^2_{\min}	Q^2_{\max}	W^2_{\min}	W^2_{\max}	χ^2	χ^2_{CB}
SLAC-E49a (DIS) [29]	117	0.586	8.067	3.130	27.19	0.55	N/A
SLAC-E49b (DIS) [29]	208	0.663	20.08	3.010	27.51	1.32	N/A
SLAC-E61 (DIS) [29]	32	0.581	1.738	3.210	16.00	0.44	N/A
SLAC-E87 (DIS) [29]	109	3.959	20.41	3.280	17.18	0.57	N/A
SLAC-E89a (DIS) [29]	77	3.645	30.31	3.300	20.43	0.60	N/A
SLAC-E89b (DIS) [29]	118	0.887	19.18	3.100	27.75	0.70	N/A
SLAC-E004 (DIS) [30]	198	0.249	20.07	3.561	26.84	0.44	N/A
SLAC-E49a6 (RES) [30]	460	0.146	3.708	1.177	3.992	0.72	1.16
SLAC-E49a10 (RES) [30]	541	0.445	8.593	1.171	4.000	0.84	1.04
SLAC-E49b (RES) [30]	366	1.018	16.74	1.153	3.992	0.81	1.15
SLAC-E61 (RES) [30]	1075	0.061	1.839	1.160	4.000	1.20	1.76
SLAC-E87 (RES) [30]	22	1.821	20.54	3.183	3.988	0.25	N/A
SLAC-E89a ^b (RES) [30]	90	7.124	32.39	1.156	4.000	0.14	N/A
SLAC-E89b ^c (RES) [30]	492	0.395	20.66	1.197	3.984	1.12	N/A
SLAC-E133 (RES) [30]	178	2.287	9.914	1.153	3.037	3.19	5.04
SLAC-E140 (RES) [30]	87	0.717	20.41	3.010	3.950	1.46	N/A
SLAC-E140X (RES) [30]	153	1.118	8.871	1.200	3.720	2.88	3.27
SLAC-NE11 (RES) [31]	113	1.606	6.855	1.164	1.788	2.27	5.78
SLAC-Onen1half (RES) [30]	745	0.011	0.263	1.153	4.000	6.18	7.00
Jlab-CLAS E1 ^d (RES) [32–35]	509	0.225	0.925	1.162	2.544	1.15	19.5
Jlab-CLAS E2 (RES) [32–35]	1443	0.475	2.175	1.162	3.987	1.44	11.3
Jlab-CLAS E3 (RES) [32–35]	2484	1.325	4.175	1.162	5.537	1.04	2.73
Jlab-CLAS E4 (RES) [32–35]	2637	1.325	4.425	1.164	5.643	0.95	1.93
Jlab-CLAS E5 (RES) [32–35]	2681	1.375	4.725	1.162	5.971	0.96	1.51
JLab-E94-110 (RES) [30]	1273	0.181	5.168	1.225	3.850	3.15	1.33
JLab-E00-116 (RES) [36]	261	3.585	7.384	1.243	5.131	1.48	1.58
JLab-E00-002 (RES) [30, 37]	1477	0.055	2.079	1.163	7.932	1.22	0.88

^a Here we show the primary source of data in our analysis which is not always the full reference to the corresponding experiment.

^b Listed as SLAC-E891 in [30].

^c Listed as SLAC-E8920 in [30].

^d The JLab-CLAS data sets E1, E2, E3, E4, E5 correspond to the beam energies 1.515, 2.567, 4.056, 4.247, 4.462 GeV, respectively.

TABLE III. Hydrogen photoproduction cross-section data sets used in our analysis. Listed are the experiments with corresponding number of data points (NDP) and kinematics coverage. The values of W^2 are in GeV^2 units. The last two columns are the values of χ^2 normalized per NDP computed in our model and in the model of Ref. [5], respectively (“N/A” has the same meaning as in Table II).

Data set	NDP	W^2_{\min}	W^2_{\max}	χ^2	χ^2_{CB}
Armstrong [38]	159	1.378	8.790	2.39	1.34
Maccormick [39]	57	1.263	2.361	2.15	7.12
Meyer [40]	18	3.038	12.61	0.69	0.54
Hilpert [41]	6	2.121	9.212	3.09	1.66
Dieterle [42]	5	2.382	11.67	1.70	N/A
Ballam [43]	3	6.135	14.95	0.79	N/A
Bingham [44]	1	18.33	18.33	0.26	N/A
Caldwell [45]	9	8.518	31.62	1.10	N/A
Caldwell [46]	30	35.22	343.7	0.64	N/A
Michalowski [47]	6	4.633	18.73	1.08	N/A
Alexander [48]	1	14.95	14.95	0.003	N/A
Aid [49]	2	39999	43681	0.27	N/A
Vereshkov [50]	4	2065	17822	0.24	N/A
GRAAL [51]	62	1.950	3.564	9.92	6.50

the total number of data points $\text{NDP} = 18298$ (most of the data are in the resonance region). Thus, we have $\chi^2/\text{NDP} \approx 1.52$. The best fit parameters together with relative fit uncertainties are listed in Table I and Tables IV to VI. The values of χ^2 normalized per number of data points of individual experiments are listed in Table II for all hydrogen electroproduction data sets used in the fit, and the corresponding χ^2 values for photoproduction data are given in Table III. The last column in Tables II and III lists the values of χ^2 computed for the model of Ref. [5], where applicable. We observe significant improvement over the results of the empirical model of Ref. [5] for all studied data sets except for the cross-section data from the JLab-E94-110 experiment.

TABLE IV. The best fit parameters describing the resonant contributions to the transverse helicity amplitude by Eq. (32). The estimate of fractional parameter uncertainty is given in parentheses in percent units.

	a_1 ($\text{GeV}^{-1/2}$)	a_2 ($\text{GeV}^{-5/2}$)	a_3 (GeV^{-2})	a_4
$\Delta(1232)$	0.31115(0.31)	2.02940(0.57)	1.67130(1.06)	2.7600(0.41)
$N(1440)$	0.08955(4.61)	0.18087(1.16)	0.23431(0.87)	4.1173(0.35)
R_1	0.10677(2.08)	0.24897(1.62)	0.55621(0.66)	3.0798(0.38)
R_2	0.38953(0.60)	-0.17962(1.88)	0.37638(3.09)	2.9622(1.70)
R_3	0.06708(5.72)	0.09733(6.26)	0.27891(4.74)	3.5372(1.42)

TABLE V. The best fit parameters describing the resonant contributions to the longitudinal helicity amplitude by Eq. (33). The estimate of fractional parameter uncertainty is given in parentheses in percent.

	c_1 ($\text{GeV}^{-1/2}$)	c_2 ($\text{GeV}^{-5/2}$)	c_3 (GeV^{-2})
$\Delta(1232)$	0.05029(6.72)	0	0.42522(6.40)
$N(1440)$	0	0.23847(2.62)	1.4982(2.03)
R_1	0.09198(4.33)	-0.10652(5.81)	1.0758(3.48)
R_2	0	0	0
R_3	0.12027(1.68)	0	0.89367(2.72)

TABLE VI. The best fit parameters describing the background function by Eq. (42). The estimate of fractional parameter uncertainty is given in parentheses in percent.

	b_1 (GeV^{-2b_2})	b_2	$m_{T,L}$
B_T	0.14453(4.19)	3.1297(1.76)	1.6302(0.19)
B_L	3.4742(2.44)	0.54193(1.26)	1.1

In order to illustrate the overall quality of our fit, in the left panel of Fig. 2 we show the distribution of the number of data points vs the residual $(v_{\text{dat}} - v_{\text{model}})/\sigma_{\text{dat}}$, where v_{dat} and σ_{dat} are the measured cross section value and its experimental uncertainty and v_{model} is the corresponding model value. The distribution is presented separately for the resonance region ($W < 2$ GeV) and for the full set of data points. The analysis of this residual distribution helps to understand the overall fit uncertainty together with the shift of fit results vs data. We found that both these residual distributions follow the normal distribution with good accuracy, with about 67% of data points within $\pm 1\sigma$ interval, and the average residual is consistent with 0.

In the right panel of Fig. 2 we show a similar distribution vs. data/model - 1 shift. We have about 78% of data points within $\pm 10\%$ interval of data/model - 1.

In Figs. 3 to 5 we show data/model ratios (pulls) for different electroproduction cross section data samples and for different kinematical regions. The pulls for the electroproduction cross section data are organized in terms of a set of panels corresponding to different Q^2 bins indicated in the plots. Note the logarithmic scale in W^2 . Figure 3 refers to the region $W^2 > 4$ GeV^2 with the set of Q^2 bins selected to cover the region $0.25 < Q^2 < 30$ GeV^2 , while Fig. 4 is focused on the resonance region $W^2 < 4$ GeV^2 and $0.25 < Q^2 < 6$ GeV^2 . For completeness, the pulls in Fig. 3 also include the DIS cross section data, such as CERN-NMC [62], CERN-BCDMS [63] and DESY-HERMES [67], which were not used in our fit but included in the global QCD analysis of Refs. [15, 16] whose PDFs and HT terms are used in our study. In view of a large number of data points from the JLab-CLAS experiment [32–35], which were presented for fixed Q^2 bins, we show the comparison with JLab-CLAS data points in Fig. 5.

Overall, our model shows a very good agreement with data in a wide region of Q^2 and W^2 . However, we also observe rather strong fluctuations of the pulls for some data sets. In particular, the pulls for different beam energies of JLab-CLAS cross section data are not always fully consistent (see, e.g., the bins with $Q^2 > 1.3$ GeV^2 in Fig. 5). The fluctuations of the data/model ratio are high in the region $W^2 < 1.5$ GeV^2 , as can be seen in Fig. 4. It is worth mentioning that SLAC-Onen1half cross section data [30] in the energy bin $E = 5$ GeV and at very low values of $Q^2 \sim 0.01$ GeV^2 are underestimated in our model resulting in a rather high χ^2 value in Table II. However, for other energy bins of this experiment our model is in a reasonable agreement with data, as illustrated by the cross-section plots in the Supplemental Material [17].

Also, our global fit to world electroproduction and photoproduction cross section data leads to a good overall description of the total photoproduction cross section (see Fig. 12 in the Supplemental Material [17]). We found that our result for the average transverse helicity amplitude squared $A(Q^2)^2$ for the $\Delta(1232)$ resonance state is in a good agreement with the results of a low- Q analysis in a unitary isobar model [4]. For the $N(1440)$ resonance state we obtained the value of a_1^2 to be consistent with that reported in the Particle Data Group review [27]. However, Q^2 dependence of the transverse amplitude $A(Q^2)$ for the $N(1440)$ state is different from that of Ref. [4].

Note that the value of a_1^2 drives the strength of corresponding resonance peak in the photoproduction cross section at $Q^2 = 0$. However, for the third resonance peak our model is somewhat off the data. Note in this context that, in a fit to only photoproduction data, we achieve a good description of data in the full region with a somewhat different set of resonance parameters, whose values are in a tension with the results from our global fit. In particular, the photoproduction data require a

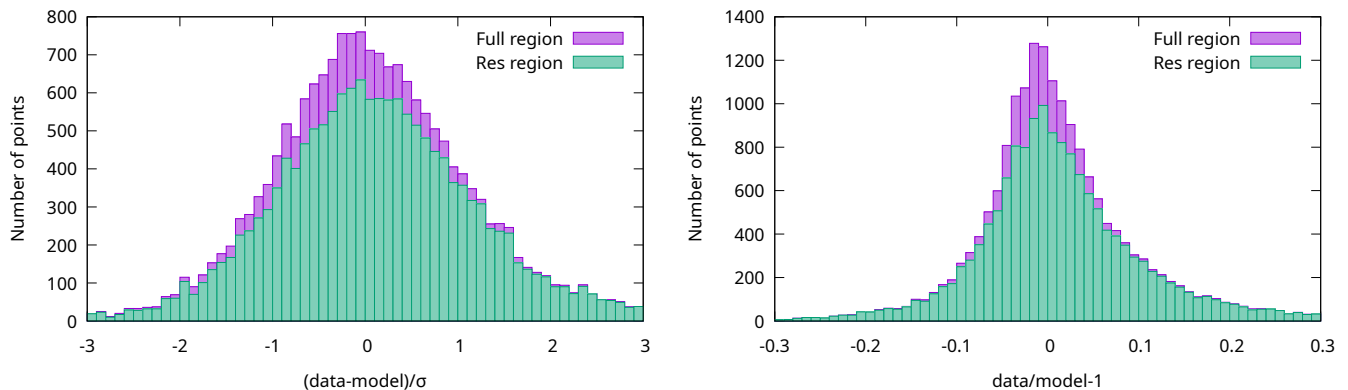


FIG. 2. Left panel: NDP distribution vs the residual $(v_{\text{dat}} - v_{\text{model}})/\sigma_{\text{dat}}$ (see text). Separate distributions are shown for the full data set and for resonance data with the legend in the figure panel. Right panel: NDP distribution vs $v_{\text{dat}}/v_{\text{model}} - 1$.

lower value of the mass of the third effective resonance together with a significantly higher value of a_1^2 for this state. This may indicate Q^2 dependence of Breit-Wigner pole positions in our effective model. This point will be addressed in future studies.

A detailed comparison of our predictions with cross-section data on both the electroproduction differential cross section from Table II and the total photoproduction cross section from Table III can be found in the Supplemental Material [17].

V. DISCUSSION

To verify our results we compare the model predictions with data which were not used in our fit, in particular the measurements of the structure function F_2 and $R = F_L/F_T$ and the DIS cross-section data in Table VII.

We first discuss the measurements of the structure function F_2 . The F_2 data in Table VII include the results of Refs. [29, 57] obtained from re-analysis of “old” SLAC data, the measurements from JLab experiments [32, 33, 36, 37, 61, 68], and we also include the F_2 and cross-section data from DESY-HERMES [67], CERN-NMC [62] and CERN-BCDMS [63]. To illustrate the quality of data description, Table VII lists the values of χ^2 per one data point for each of the data set.

Note that the F_2 extractions from various experiments listed in Table VII depend on the input for R . The F_2 measurements of Refs. [37, 61] were based on the Rosenbluth separation of F_T and F_L , while the F_2 extractions from Refs. [29, 33, 36] used different models of R constrained by data. The F_2 extraction of Ref. [62] was based on their own measurement of R , while the F_2 extraction of Ref. [63] assumed $R = 0$. This may explain the significant difference in the values of χ^2 in our model for the cross-section data and F_2 data of Ref. [63] in Table VII.

Our results on F_2 are illustrated in Figs. 6 to 9. Figure 6 shows the pulls for $W^2 > 4 \text{ GeV}^2$ and $0.25 < Q^2 < 30 \text{ GeV}^2$, which are organized in the panels of Q^2 bins

indicated in the plot. Figure 7 shows similar pulls for the resonance region of $W^2 < 4 \text{ GeV}^2$ and $0.2 < Q^2 < 5.5 \text{ GeV}^2$.

In Figs. 8 and 9 the structure function F_2 is shown vs W^2 for a number of Q^2 bins, which are indicated in the panels. The curves with our predictions are drawn for the central value of each Q^2 bin. Also shown are the data points from different experiments selected in the given Q^2 bins. Figure 8 covers the region up to $W^2 = 150 \text{ GeV}^2$ and $0.3 < Q^2 < 16 \text{ GeV}^2$, while Fig. 9 focuses on the resonance region $W^2 < 4.2 \text{ GeV}^2$ and $0.25 < Q^2 < 7 \text{ GeV}^2$.

For comparison, together with our results in Fig. 8 and 9 we also show the predictions from Ref. [5] (the dashed curve labeled “CB”). We observe that our predictions are consistent with the CB fit for $W^2 < 8 \text{ GeV}^2$ and $Q^2 < 10 \text{ GeV}^2$. The inspection of χ^2 values in Table VII suggests that our approach provides better overall description of data in the resonance region for almost all data sets except for the JLab-E94-110 experiment. The CB model fails for $W^2 > 8 \text{ GeV}^2$. In contrast, our predictions can be applied in a wide range of kinematics since at high values of Q^2 and W^2 our model merges the DIS description from a global QCD analysis [15]. For completeness, in Figs. 8 and 9 we also show the background contribution which clearly dominates for $W^2 > 3.5 \text{ GeV}^2$ and merges with the DIS structure function at higher values of W^2 .

Figure 10 shows the measurements of $R = F_L/F_T$ [29, 37, 58–61] as a function of W^2 together with our predictions. The plots in Fig. 10 are organized in terms of panels of Q^2 bins covering the region from 0.25 to 10 GeV^2 . The data points marked with the symbol “R” in the legend correspond to the measurements based on the Rosenbluth separation method. Our predictions are indicated by the solid curve and for comparison we also show the results obtained with the parametrization R_{1998} [60] and the CB model [5]. Note also that while our predictions are for the proton, the data on R in Fig. 10 are collected for different nuclear targets including ^2H , ^{56}Fe , and ^{197}Au (SLAC-E140 [58]), ^2H and ^9Be (SLAC-E140X [59]), and

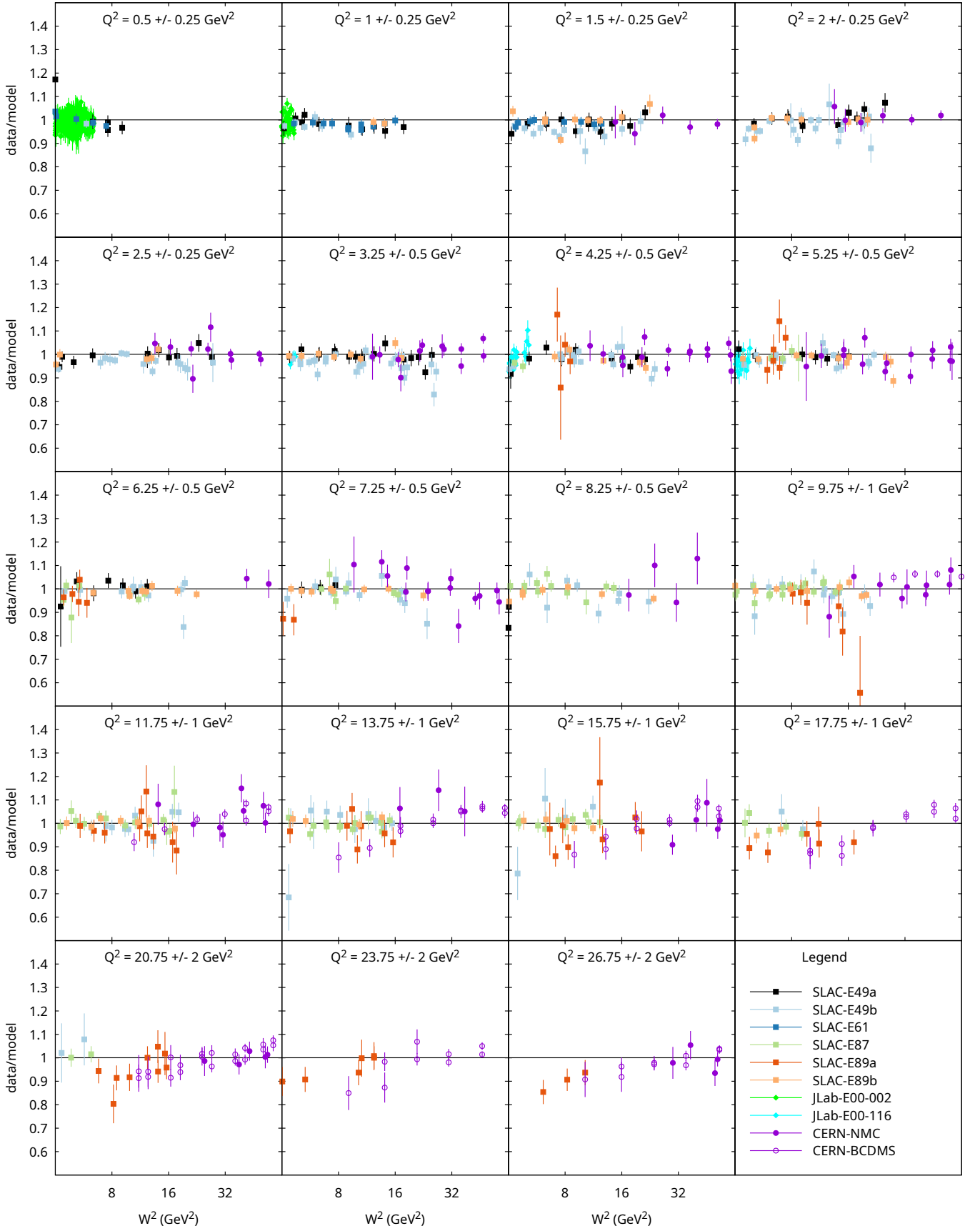
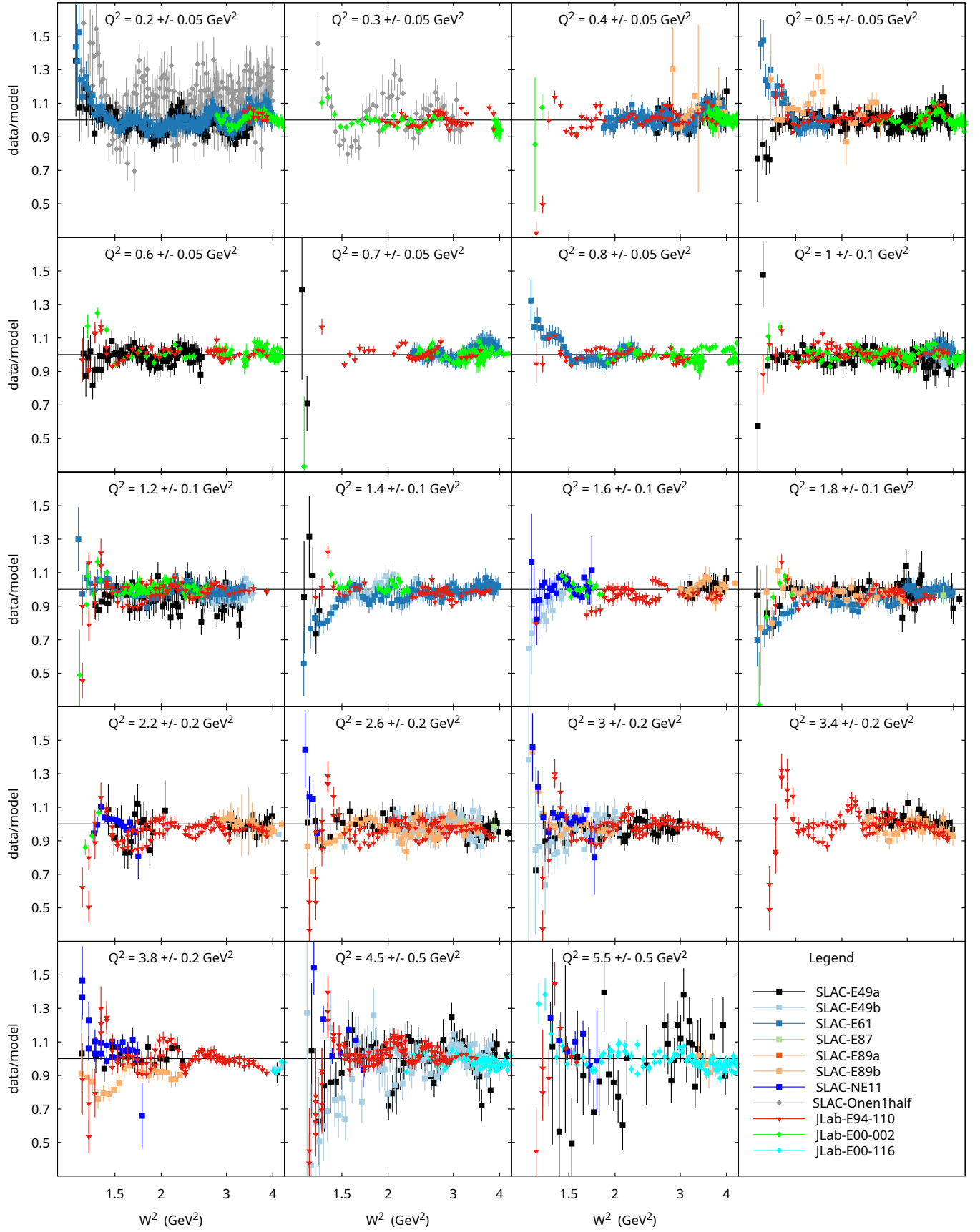


FIG. 3. The pulls for cross-section data of Table II with $W^2 > 4 \text{ GeV}^2$. Data points are grouped in Q^2 bins indicated in the panels. The error bars include statistical and systematic uncertainties of data taken in quadrature. The legend for the data points is shown in the lower-right panel.



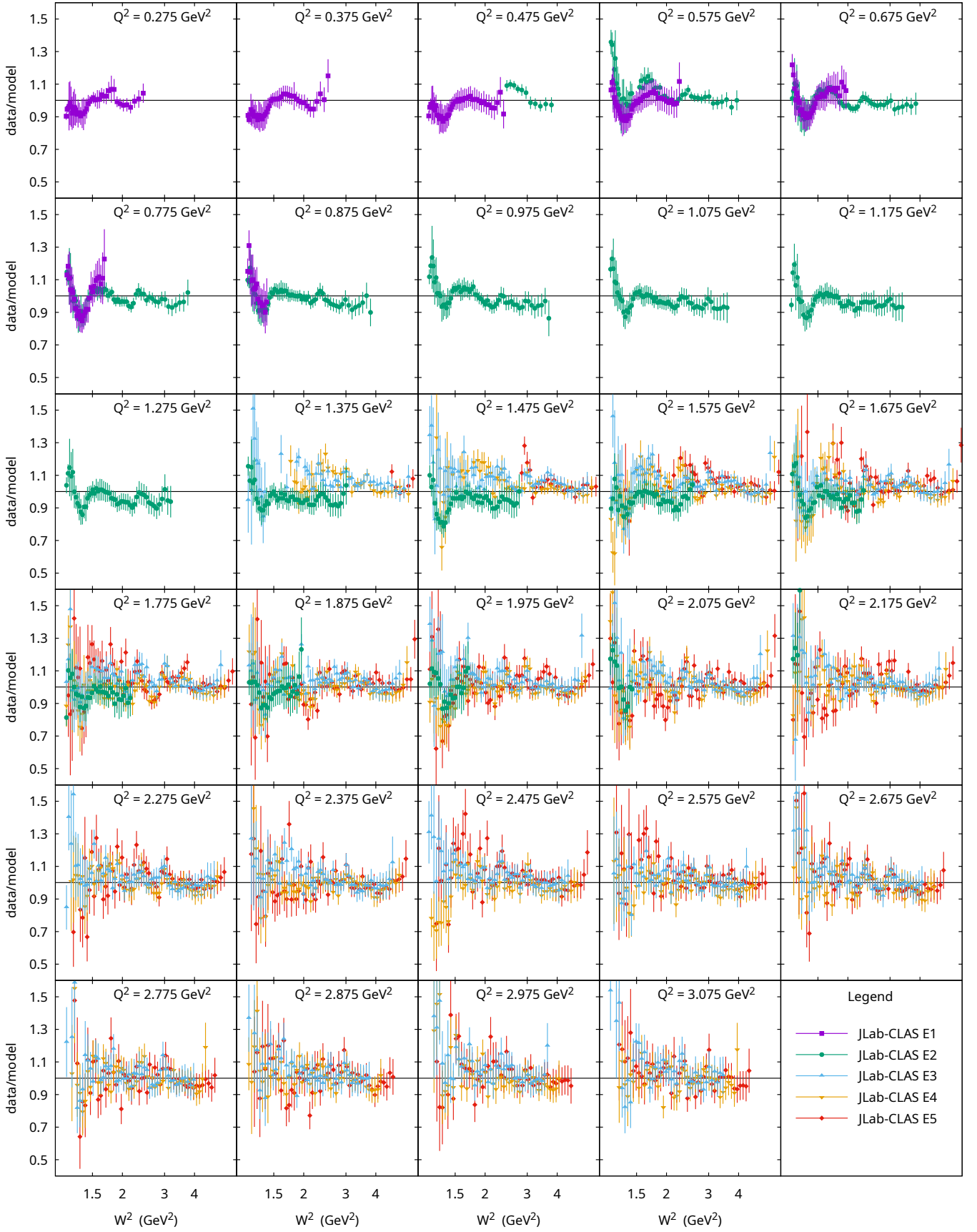


FIG. 5. The pulls for JLab-CLAS cross-section data listed in Table II. The panels correspond to Q^2 bins from JLab-CLAS measurement. The error bars include statistical and systematic uncertainties of data taken in quadrature. The legend for data points is shown in the lower-right panel.

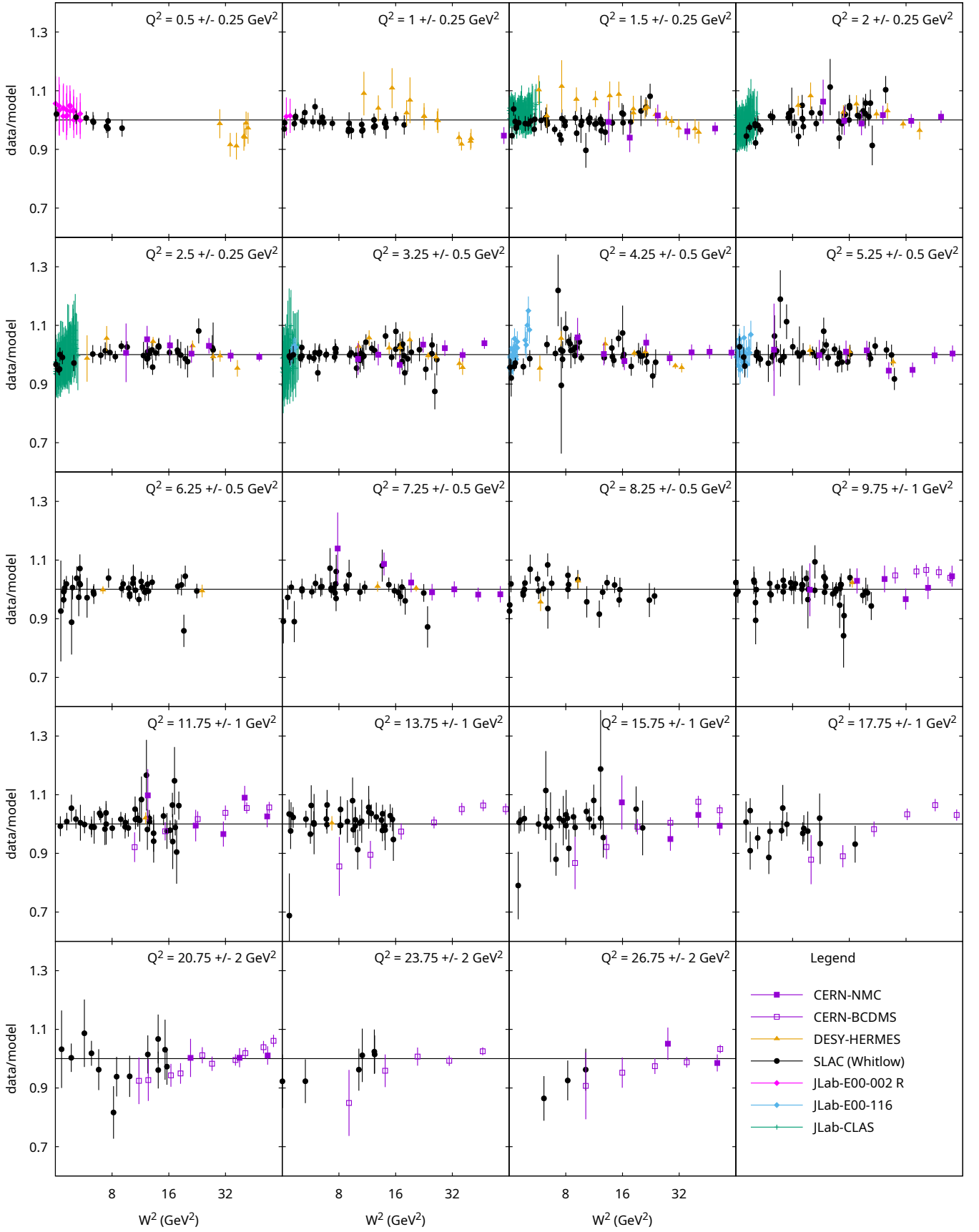


FIG. 6. The pulls for F_2 data in Table VII vs W^2 . Shown is the region $W^2 > 4 \text{ GeV}^2$. Data points were grouped in Q^2 bins indicated in the panels. The error bars include statistical and systematic uncertainties of data taken in quadrature. The legend for the data points is shown in the lower-right panel.

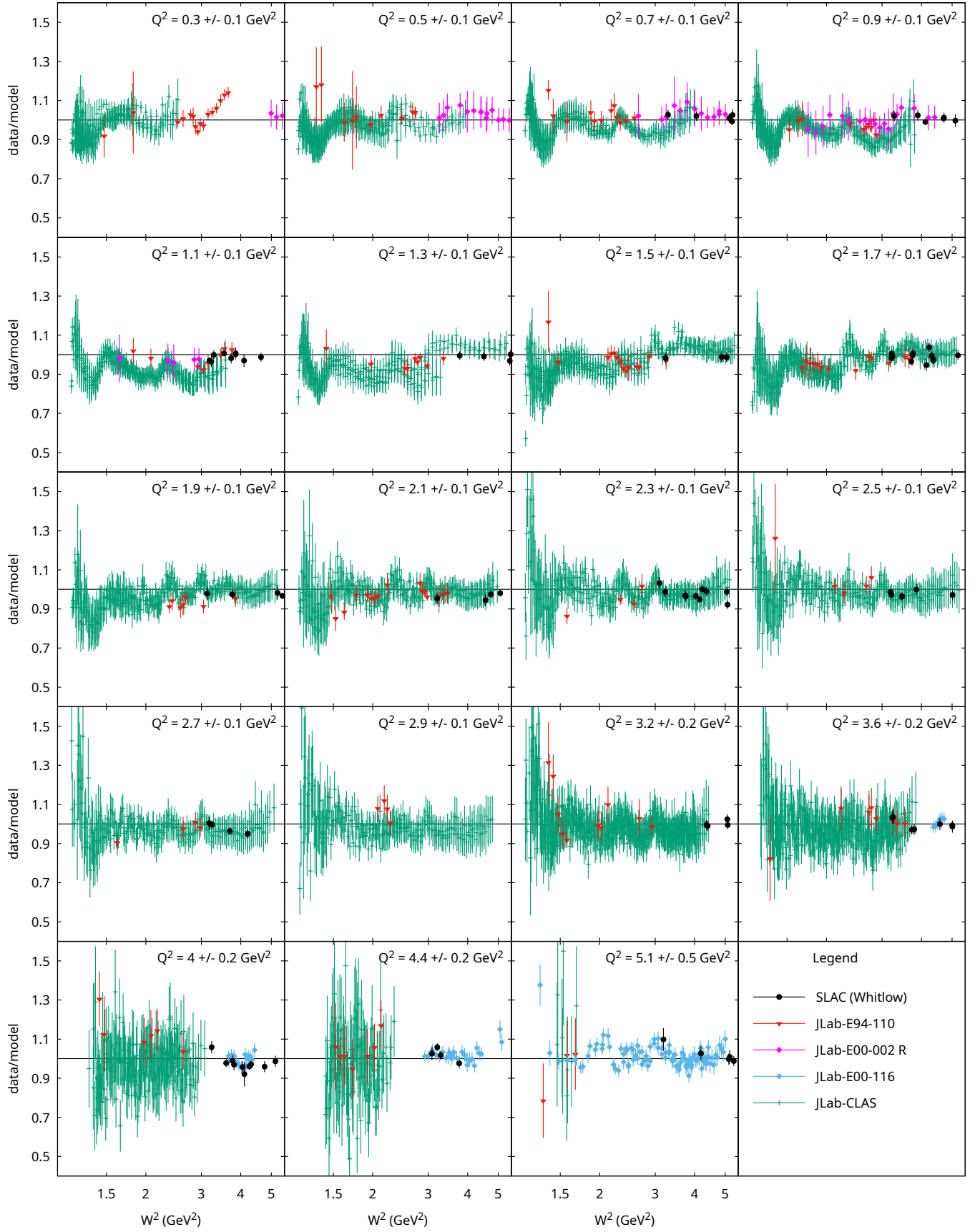


FIG. 7. Similar to Fig. 6 but for the region of $W^2 < 5.5$ GeV 2 .

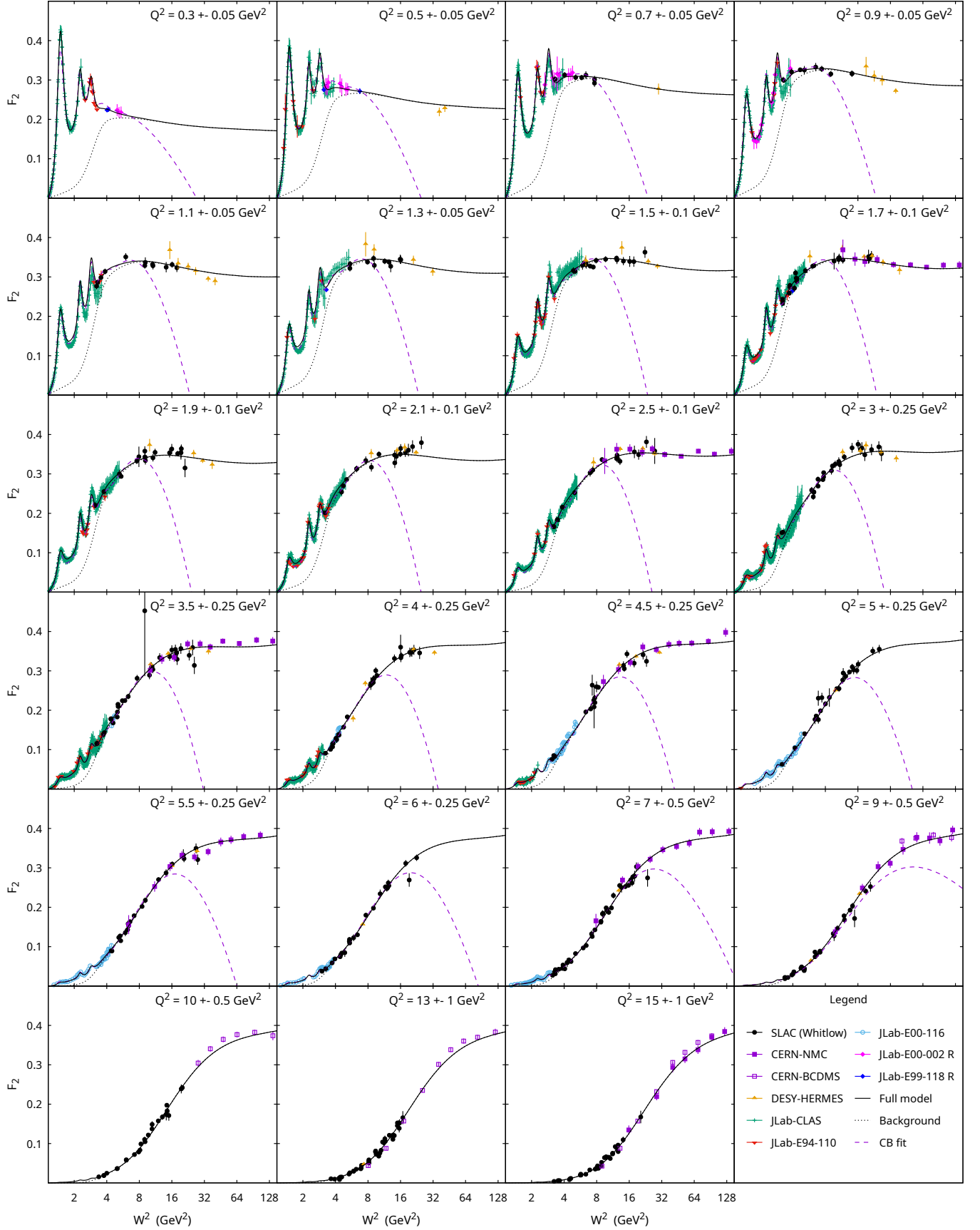


FIG. 8. Our predictions on F_2 (solid line) in comparison with data for $W^2 < 150$ GeV² and for a number of Q^2 bins indicated in the panels. The curves are drawn for the central value of each of the Q^2 bin. The legend for the data points is shown in the lower-right panel. The background contribution is shown by dotted line while the results of Ref. [5] (CB) are shown by the dashed line.

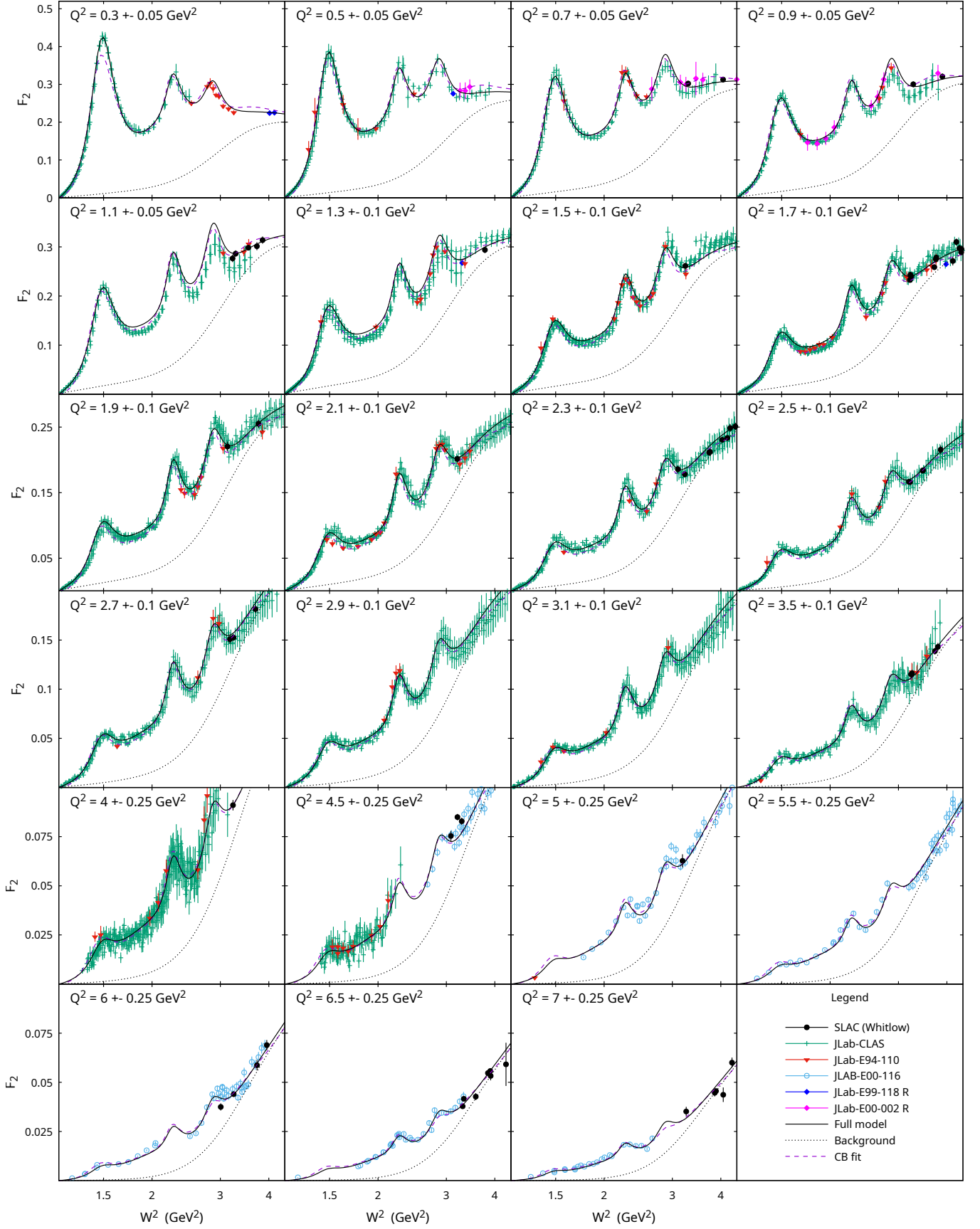


FIG. 9. Similar to Fig. 8 but focusing on the region $W^2 < 4.5$ GeV² and $Q^2 \lesssim 7$ GeV².

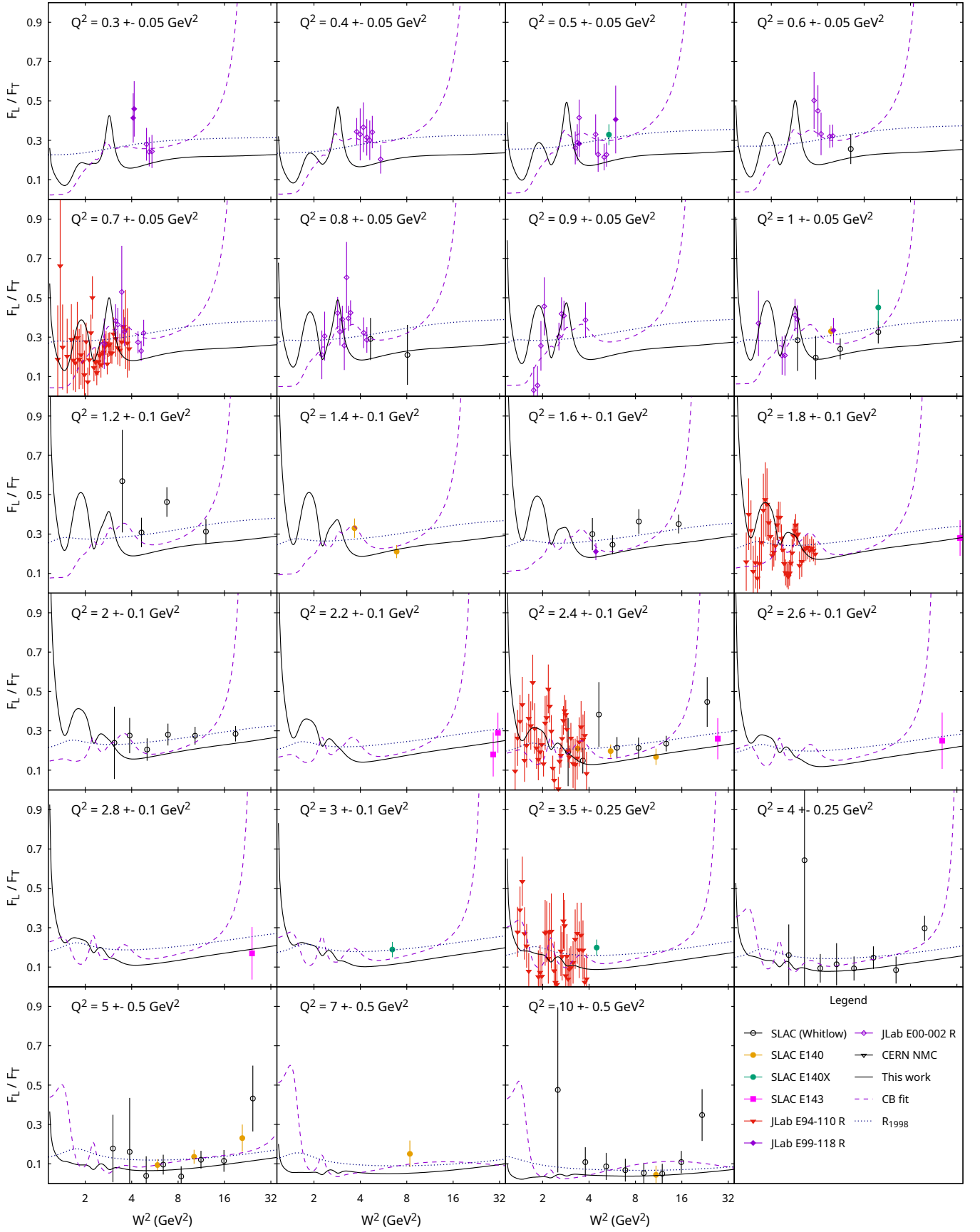


FIG. 10. Our predictions (solid line) on the ratio $R = F_T/F_L$ vs W^2 in comparison with data for a number of Q^2 bins indicated in the panels. The curves are drawn for the central value of each Q^2 bin. Also shown are the prediction from Ref. [5] (CB, dashed) and R_{1998} fit [60] (dotted). The legend is given in the lower-right panel.

TABLE VII. The list of F_2 and cross-section data sets not used in our fit. Also shown the corresponding number of data points (NDP) and kinematics coverage. The values of Q^2 and W^2 are in GeV^2 units. The “DIS” label indicates data which are mostly in the DIS region while “RES” labels the data samples which are mostly in the resonance region. The last two columns are the values of χ^2 normalized per NDP computed, respectively, in our model and using parameterization of Ref. [5] (“N/A” has the same meaning as in Table II).

F_2 data set	NDP	Q_{\min}^2	Q_{\max}^2	W_{\min}^2	W_{\max}^2	χ^2	χ_{CB}^2
SLAC-E49a [29] (DIS)	117	0.586	8.067	3.131	27.24	0.50	N/A
SLAC-E49b [29] (DIS)	208	0.663	20.08	3.007	27.51	0.72	N/A
SLAC-E61 [29] (DIS)	32	0.581	1.738	3.213	16.05	0.34	N/A
SLAC-E87 [29] (DIS)	109	3.959	20.41	3.287	17.16	0.59	N/A
SLAC-E89a [29] (DIS)	77	3.645	30.31	3.303	20.46	1.01	N/A
SLAC-E89b [29] (DIS)	118	0.887	19.18	3.099	27.78	0.52	N/A
JLab-CLAS [33] (RES)	4191	0.225	4.725	1.162	5.804	1.17	6.13
JLab-E94-110 [68] (RES)	170	0.181	4.794	1.325	3.850	1.90	0.72
JLab-E00-116 [69] (RES)	261	3.585	7.384	1.243	5.132	1.42	1.94
JLab-E00-002 [37] (RES)	54	0.300	1.000	1.650	5.419	0.24	0.05
CERN-NMC [62] (DIS)	157	0.750	65.00	6.380	553.9	1.74	N/A
CERN-BCDMS [63] (DIS)	177	7.500	230.0	8.042	351.0	2.31	N/A
DESY-HERMES [67] (DIS)	80	0.354	12.78	5.751	42.17	0.28	N/A
Cross-section data set	NDP	Q_{\min}^2	Q_{\max}^2	W_{\min}^2	W_{\max}^2	χ^2	χ_{CB}^2
CERN-NMC [62] (DIS)	292	0.750	65.00	6.380	553.9	1.38	N/A
CERN-BCDMS [63] (DIS)	351	7.500	230.0	8.042	351.0	1.15	N/A
DESY-HERMES [67] (DIS)	81	0.354	12.78	5.751	42.17	0.45	N/A

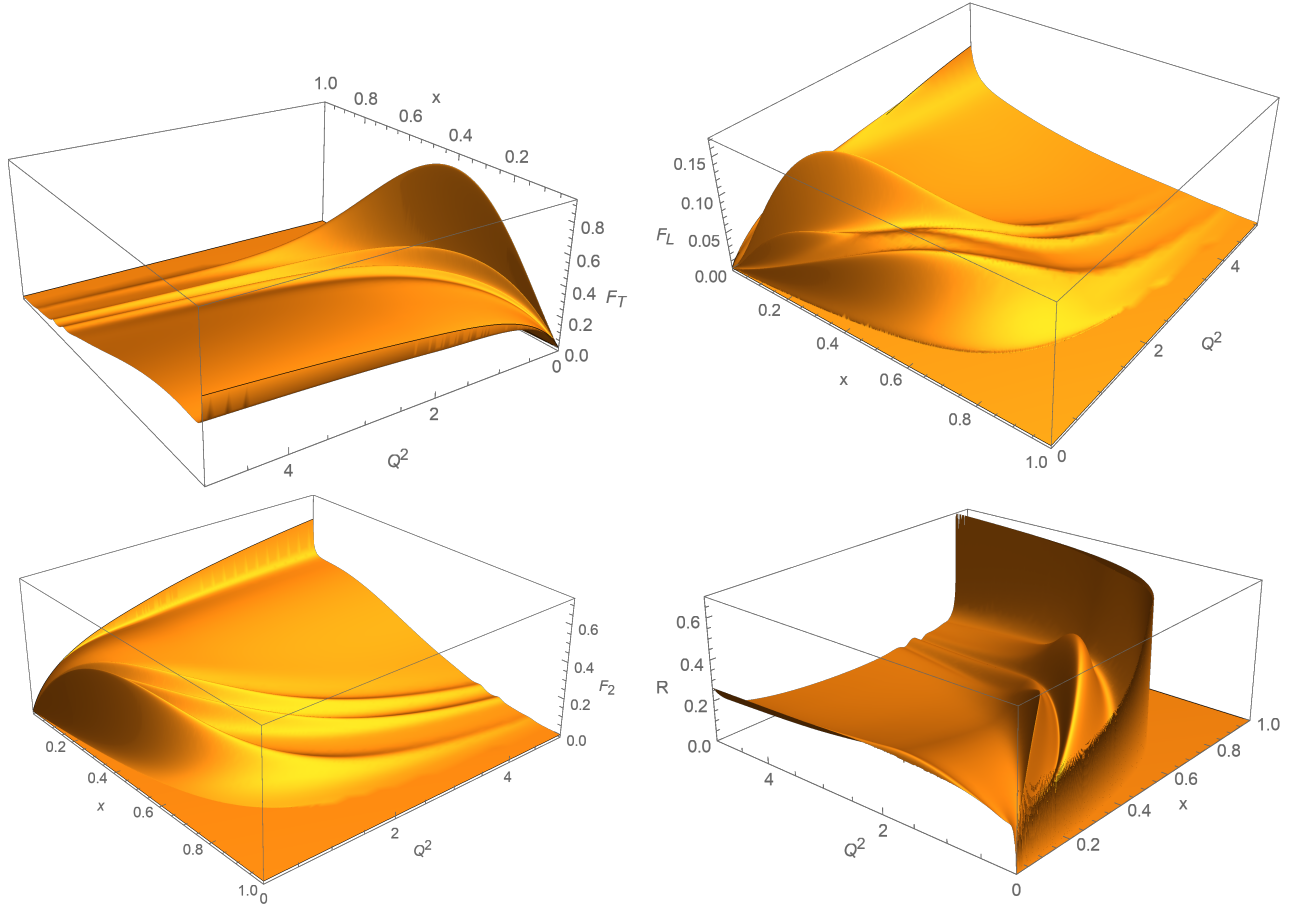


FIG. 11. The structure functions F_T , F_L , F_2 , and R vs (x, Q^2) .

^{12}C (SLAC-E143 [60]).

It should be remarked that while our model provides

$R = 0$ at $Q^2 = 0$, the transition to this limit occurs at a very low scale $Q^2 \ll 0.1 \text{ GeV}^2$, because the value of parameter m_L , which drives a low- Q asymptotic of background part of F_L , is close to 1. If we release m_L , the fit prefers $m_L \rightarrow 1$ (although with significant uncertainty). In order to have vanishing R at the real photon point, in the final fit trial we fixed the value $m_L = 1.1$.

Note also an oscillating behavior of R vs. W in the resonance region with Q^2 -dependent amplitudes, as can be seen in Fig. 10. Overall, our predictions for R are in a reasonable agreement with available measurements, although the data uncertainties are rather large.

In Fig. 11 we illustrate the x and Q^2 dependence of SFs in our model in the region $0.001 < x < 1$ and $0.01 < Q^2 < 5 \text{ GeV}^2$ by plotting the surfaces of F_T , F_L , F_2 and R . We show SFs at different surface view points in order to better view various features of resonance structures. We clearly see that for $Q^2 < 2 \text{ GeV}^2$ the resonance structures drive SF strength at low values of W across the x region while their impact rapidly decreases with Q^2 . The details of resonance contributions differ for various SFs. In this context, we note a sharp $\Delta(1232)$ resonance structure on the F_T surface and a pronounced peak from the third effective resonance on the F_L surface. Also pronounced resonance structures are present in the ratio $R = F_L/F_T$. Note that a sharp wall-like structure in R at large values of x is not because of a resonance contribution but is owed to a different W dependence of background contributions to F_T and F_L in a region close to the inelastic threshold.

In conclusion, we examine the duality property of our model. The quark-hadron duality principle suggests an integral relation between the observed structure function, which includes the resonance contributions, and a smooth DIS structure function [10]. We then verify the following integral relation:

$$\int_{W_{\text{th}}^2}^{W_0^2} dW^2 F_2(W^2, Q^2) = \int_{W_{\text{th}}^2}^{W_0^2} dW^2 F_2^{\text{DIS}}(W^2, Q^2), \quad (48)$$

where on the left we use SF of the present model and on the right the DIS SF by Eq. (11) from Ref. [15]. The integration is taken from the pion production threshold $W_{\text{th}}^2 = (M + m_\pi)^2$ to the boundary of the resonance region for which we take $W_0^2 = 4 \text{ GeV}^2$. We found that this relation holds with rather high accuracy, with the relative error ranging between 1 and 2% for $1.3 < Q^2 < 5 \text{ GeV}^2$. We also studied Eq. (48) for F_T and F_L . We found somewhat lower accuracy of the duality relation for F_T , with the relative error up to 5% for $1 < Q^2 < 3 \text{ GeV}^2$. For higher Q^2 the accuracy of the duality relation for F_T is on the level of that for F_2 . The accuracy of Eq. (48) is poor for F_L for $1 < Q^2 < 3 \text{ GeV}^2$, where the difference between the left and right sides of Eq. (48) is between 15

and 25%. Nevertheless Eq. (48) for F_L gradually becomes more accurate at higher Q^2 .

VI. SUMMARY

To summarize, in this paper we develop a hybrid model of the proton structure functions applicable in a wide region of Q^2 and W^2 . In the nucleon resonance region, $W < 2 \text{ GeV}$, we account for contributions from the $\Delta(1232)$ resonance, the $N(1440)$ Roper resonance, and three more heavy effective resonances responsible for the second and third resonance regions in the spectra. Nonresonant background is computed in terms of DIS structure functions properly continued into a low- Q and low- W region. Our extrapolation method respects the pion production threshold as well as the $Q^2 \rightarrow 0$ real photon limit. The onset of a low- Q region is defined by the parameter Q_0 , the scale from which we start extrapolations of DIS SFs. The value $Q_0^2 = 2 \text{ GeV}^2$ provides an optimum description of electroproduction data in our analysis, as discussed in Sec. IV. The DIS region of $Q > Q_0$ and $W > 2 \text{ GeV}$ is well described in terms of the proton PDFs and the higher-twist terms from a global QCD analysis [15, 16].

The model parameters, such as resonance masses and widths, parameters of resonance helicity amplitudes, scale parameter for transition region, as well as parameters responsible for extrapolation to low- Q and low- W values, are adjusted from a global fit to the world data on hydrogen electroproduction and photoproduction cross section. This approach allows us to determine parameters of both the transverse and the longitudinal SFs reproducing available cross-section data with a very good accuracy, as illustrated in detail by the data/model ratios in Figs. 3 to 5. For a detailed comparison of our model with cross-section data see the Supplemental Material [17].

We verify the model performance by comparing our predictions with available measurements of the proton F_2 and the ratio $R = F_L/F_T$. Figures 6 to 9 and Table VII show a very good overall agreement of our predictions with F_2 measurements. Figure 10 illustrates the model performance against available measurements of R .

Also, we verified that our hybrid model of structure functions is dual in the integral sense to the underlying DIS structure functions. The duality relation, Eq. (48), holds with a good accuracy for F_2 .

Work is in progress on extending this approach to determine parameters of the neutron structure functions from a combined set of the proton and nuclear data. Also in progress is the generalization of this model to neutrino-nucleon scattering in the resonance and DIS transition region, which is of primary importance for interpretation of data from current and future neutrino experiments.

Code to numerically compute the model structure functions F_T , F_L and F_2 is available from the authors upon email request.

VII. ACKNOWLEDGMENTS

We thank S. Alekhin, A. Kataev, and R. Petti, for useful discussions, and M. Osipenko for providing the data of the JLab-CLAS Collaboration. V.V.B. was supported by the BASIS Foundation for the Development of Theoretical Physics and Mathematics.

-
- [1] A. Accardi, S. Alekhin, J. Blümlein, M. Garzelli, M. K. Lipka, W. Melnitchouk, S. Moch, J. Owens, R. Placakyte, E. Reya, N. Sato, A. Vogt, and O. Zenaiev, A critical appraisal and evaluation of modern PDFs, *Eur. Phys. J.* **C76**, 471 (2016), [arXiv:1603.08906](#).
 - [2] J. Gao, L. Harland-Lang, and J. Rojo, The structure of the proton in the LHC precision era, *Phys. Rept.* **742**, 1 (2018), [arXiv:1709.04922](#).
 - [3] R. L. Walker, Phenomenological analysis of single pion photoproduction, *Phys. Rev.* **182**, 1729 (1969).
 - [4] D. Drechsel, O. Hanstein, S. Kamalov, and L. Tiator, A unitary isobar model for pion photoproduction and electroproduction on the proton up to 1 GeV, *Nucl. Phys.* **A645**, 145 (1999), [arXiv:nucl-th/9807001](#).
 - [5] M. E. Christy and P. E. Bosted, Empirical fit to precision inclusive electron-proton cross sections in the resonance region, *Phys. Rev.* **C81**, 055213 (2010), [arXiv:0712.3731](#).
 - [6] A. N. Hiller Blin *et al.*, Nucleon resonance contributions to unpolarised inclusive electron scattering, *Phys. Rev.* **C100**, 035201 (2019), [arXiv:1904.08016](#).
 - [7] I. G. Aznauryan and V. D. Burkert, Electroexcitation of nucleon resonances, *Prog. Part. Nucl. Phys.* **67**, 1 (2012), [arXiv:1109.1720](#).
 - [8] R. Fiore, A. Flachi, L. L. Jenkovszky, A. I. Lengyel, and V. K. Magas, A kinematically complete analysis of the CLAS data on the proton structure function F_2 in a Regge dual model, *Phys. Rev. D* **69**, 014004 (2004), [arXiv:hep-ph/0308178](#).
 - [9] S. Brown, G. Niculescu, and I. Niculescu, Machine learning representation of the F_2 structure function over all charted Q^2 and x range, *Phys. Rev. C* **104**, 064321 (2021), [arXiv:2106.06390](#).
 - [10] E. D. Bloom and F. J. Gilman, Scaling, duality, and the behavior of resonances in inelastic electron-proton scattering, *Phys. Rev. Lett.* **25**, 1140 (1970).
 - [11] A. Manohar, P. Nason, G. P. Salam, and G. Zanderighi, How bright is the proton? A precise determination of the photon parton distribution function, *Phys. Rev. Lett.* **117**, 242002 (2016), [arXiv:1607.04266](#).
 - [12] S. Kulagin, Nuclear effects in the deuteron in the resonance and deep-inelastic scattering region, *Phys. Part. Nucl.* **50**, 506 (2019), [arXiv:1812.11738](#).
 - [13] S. A. Kulagin, Modelling the nuclear parton distributions, *J. Phys. Conf. Ser.* **762**, 012072 (2016), [arXiv:1606.07016](#).
 - [14] R. Acciarri *et al.* (DUNE), Long-Baseline Neutrino Facility (LBNF) and Deep Underground Neutrino Experiment (DUNE): Conceptual Design Report, Volume 2: The Physics Program for DUNE at LBNF, [arXiv:1512.06148](#).
 - [15] S. Alekhin, S. A. Kulagin, and R. Petti, Modeling lepton-nucleon inelastic scattering from high to low momentum transfer, *Proceedings, 5th International Workshop on Neutrino-Nucleus Interactions in the Few GeV Region (NuInt07): Batavia, USA, May 30-June 3, 2007*, *AIP Conf. Proc.* **967**, 215 (2007), [arXiv:0710.0124](#).
 - [16] S. Alekhin, S. A. Kulagin, and R. Petti, Update of the global fit of PDFs including the low- Q DIS data, in *Proceedings, 16th International Workshop on Deep Inelastic Scattering and Related Subjects (DIS 2008): London, UK, April 7-11, 2008* (2008) p. 43, [arXiv:0810.4893](#).
 - [17] See [Supplemental Material](#) for a detailed comparison of our predictions with hydrogen cross-section data listed in Tables II and III.
 - [18] B. L. Ioffe, V. A. Khoze, and L. N. Lipatov, *Hard Processes. Vol. 1: Phenomenology. Quark-Parton Model* (Elsevier, Amsterdam, 1984).
 - [19] J. C. Collins, D. E. Soper, and G. F. Sterman, Factorization of Hard Processes in QCD, *Adv. Ser. Direct. High Energy Phys.* **5**, 1 (1989), [arXiv:hep-ph/0409313](#).
 - [20] S. Alekhin, J. Blümlein, S. Moch, and R. Placakyte, Parton distribution functions, α_s , and heavy-quark masses for LHC Run II, *Phys. Rev. D* **96**, 014011 (2017), [arXiv:1701.05838](#).
 - [21] S. I. Alekhin, S. A. Kulagin, and R. Petti, Nuclear effects in the deuteron and constraints on the d/u ratio, *Phys. Rev. D* **96**, 054005 (2017), [arXiv:1704.00204](#).
 - [22] S. A. Kulagin and R. Petti, Global study of nuclear structure functions, *Nucl. Phys.* **A765**, 126 (2006), [arXiv:hep-ph/0412425](#).
 - [23] S. A. Kulagin and R. Petti, Structure functions for light nuclei, *Phys. Rev. C* **82**, 054614 (2010), [arXiv:1004.3062](#).
 - [24] D. Abrams *et al.* (MARATHON), Measurement of the nucleon F_2^n/F_2^p structure function ratio by the Jefferson Lab MARATHON Tritium/Helium-3 deep-inelastic scattering experiment, *Phys. Rev. Lett.* **128**, 132003 (2022), [arXiv:2104.05850](#).
 - [25] H. Georgi and H. D. Politzer, Freedom at moderate energies: masses in color dynamics, *Phys. Rev. D* **14**, 1829 (1976).
 - [26] J. D. Bjorken and J. D. Walecka, Electroproduction of nucleon resonances, *Annals Phys.* **38**, 35 (1966).
 - [27] M. Tanabashi *et al.* (Particle Data Group), Review of Particle Physics, *Phys. Rev. D* **98**, 030001 (2018).
 - [28] J. Cudell, V. Ezhela, K. Kang, S. Lugovsky, and N. Tkachenko, High-energy forward scattering and the pomeron: simple pole versus unitarized models, *Phys. Rev. D* **61**, 034019 (2000), Erratum: *ibid.* **63**, 059901(E) (2001), [arXiv:hep-ph/9908218](#).
 - [29] L. W. Whitlow, *Deep Inelastic Structure Functions From Electron Scattering on Hydrogen, Deuterium, and Iron at $0.6 \leq Q^2 \leq 30 \text{ GeV}^2$* , *Ph.D. thesis*, SLAC (1990).
 - [30] Resonance data archive, <https://hallcweb.jlab.org/resdata/database/>.
 - [31] L. M. Stuart *et al.* (NE11), Measurements of the $\Delta(1232)$ transition form-factor and the ratio σ_n/σ_p from inelastic electron-proton and electron-deuteron scattering, *Phys. Rev. D* **58**, 032003 (1998), [arXiv:hep-ph/9612416](#).
 - [32] M. Osipenko *et al.* (CLAS), A kinematically complete measurement of the proton structure function F_2 in the

- resonance region and evaluation of its moments, *Phys. Rev. D* **67**, 092001 (2003), [arXiv:hep-ph/0301204](#).
- [33] M. Osipenko *et al.* (CLAS), The proton structure function F_2 with CLAS, [arXiv:hep-ex/0309052](#).
- [34] M. Osipenko (private communication).
- [35] CLAS physics database, <https://clas.sinp.msu.ru/cgi-bin/jlab/db.cgi>.
- [36] S. P. Malace *et al.* (JLab E00-116), Applications of quark-hadron duality in F_2 structure function, *Phys. Rev. C* **80**, 035207 (2009), [arXiv:0905.2374](#).
- [37] V. Tvaskis *et al.*, Measurements of the separated longitudinal structure function F_L from hydrogen and deuterium targets at low Q^2 , *Phys. Rev. C* **97**, 045204 (2018), [arXiv:1606.02614](#).
- [38] T. Armstrong *et al.*, Total hadronic cross-section of gamma rays in hydrogen in the energy range 0.265 GeV to 4.215 GeV, *Phys. Rev. D* **5**, 1640 (1972).
- [39] M. MacCormick *et al.*, Total photoabsorption cross-sections for ^1H , ^2H and ^3He from 200 to 800 MeV, *Phys. Rev. C* **53**, 41 (1996).
- [40] H. Meyer *et al.*, Total cross section for photoproduction of hadrons on hydrogen and deuterium between 1.0 and 6.4 GeV, *Phys. Lett. B* **33**, 189 (1970).
- [41] H. Hilpert *et al.*, Total cross section for photoproduction of hadrons on protons up to 5 GeV, *Phys. Lett. B* **77**, 474 (1968).
- [42] M. L. Perl *et al.*, Muon-proton inelastic scattering and vector dominance, *Phys. Rev. Lett.* **23**, 1191 (1969).
- [43] J. Ballam *et al.*, Bubble chamber study of photoproduction by 2.8 and 4.7-GeV polarized photons. 1. Cross-Section Determinations and Production of ρ^0 and Δ^{++} in the reaction $\gamma p \rightarrow p\pi^+\pi^-$, *Phys. Rev. D* **5**, 545 (1972).
- [44] H. Bingham *et al.*, Total and partial γp cross-sections at 9.3 GeV, *Phys. Rev. D* **8**, 1277 (1973).
- [45] D. O. Caldwell, V. Elings, W. Hesse, R. Morrison, F. V. Murphy, and D. Yount, Total hadronic photoabsorption cross-sections on hydrogen and complex nuclei from 4 to 18 GeV, *Phys. Rev. D* **7**, 1362 (1973).
- [46] D. O. Caldwell *et al.*, Measurements of the photon total cross-section on protons from 18 to 185 GeV, *Phys. Rev. Lett.* **40**, 1222 (1978).
- [47] S. Michalowski *et al.*, Experimental study of nuclear shadowing in photoproduction, *Phys. Rev. Lett.* **39**, 737 (1977).
- [48] G. Alexander *et al.*, Total and partial γd , γn and γp cross sections at 7.5 GeV, *Nucl. Phys. B* **68**, 1 (1974).
- [49] S. Aid *et al.* (H1), Measurement of the total photon-proton cross-section and its decomposition at 200 GeV center-of-mass energy, *Z. Phys. C* **69**, 27 (1995), [arXiv:hep-ex/9509001](#).
- [50] G. Vereshkov, O. Lalakulich, Y. Novoseltsev, and R. Novoseltseva, Total cross section for photon nucleon interaction in the energy range $\sqrt{s} = 40 - 50$ GeV, *Phys. Atom. Nucl.* **66**, 565 (2003).
- [51] O. Bartalini *et al.*, Measurement of the total photoabsorption cross section on a proton in the energy range 600 – 1500 MeV at the GRAAL, *Phys. Atom. Nucl.* **71**, 75 (2008).
- [52] J. S. Poucher *et al.* (E049a), High-energy single-arm inelastic ep and ed scattering at 6 and 10 degrees, *Phys. Rev. Lett.* **32**, 118 (1974).
- [53] A. Bodek *et al.* (E049b, E087), Experimental studies of the neutron and proton electromagnetic structure functions, *Phys. Rev. D* **20**, 1471 (1979).
- [54] W. B. Atwood *et al.* (E089a), Inelastic electron scattering from hydrogen at 50 and 60 degrees, *Phys. Lett. B* **64**, 479 (1976).
- [55] M. D. Mestayer *et al.*, The ratio σ_L/σ_T from deep-inelastic electron scattering, *Phys. Rev. D* **27**, 285 (1983).
- [56] S. Stein *et al.* (E061), Electron scattering at 4 degrees with energies of 4.5 – 20 GeV, *Phys. Rev. D* **12**, 1884 (1975).
- [57] L. W. Whitlow, E. M. Riordan, S. Dasu, S. Rock, and A. Bodek, Precise measurements of the proton and deuteron structure functions from a global analysis of the SLAC deep inelastic electron scattering cross-sections, *Phys. Lett. B* **282**, 475 (1992).
- [58] S. Dasu *et al.* (E140), Measurement of kinematic and nuclear dependence of $R = \sigma_L/\sigma_T$ in deep inelastic electron scattering, *Phys. Rev. D* **49**, 5641 (1994).
- [59] L. H. Tao *et al.* (E140X), Precision measurement of $R = \sigma_L/\sigma_T$ on hydrogen, deuterium and beryllium targets in deep inelastic electron scattering, *Z. Phys. C* **70**, 387 (1996).
- [60] K. Abe *et al.* (E143), Measurements of $R = \sigma_L/\sigma_T$ for $0.03 < x < 0.1$ and fit to world data, *Phys. Lett. B* **452**, 194 (1999), [arXiv:hep-ex/9808028](#).
- [61] Y. Liang *et al.* (JLab E94-110), Measurement of $R = \sigma_L/\sigma_T$ and the separated longitudinal and transverse structure functions in the nucleon resonance region, [arXiv:nucl-ex/0410027](#).
- [62] M. Arneodo *et al.* (New Muon), Measurement of the proton and deuteron structure functions, F_2^p and F_2^d , and of the ratio σ_L/σ_T , *Nucl. Phys. B* **483**, 3 (1997), [arXiv:hep-ph/9610231](#).
- [63] A. Benvenuti *et al.* (BCDMS), A high statistics measurement of the proton structure functions $F_2(x, Q^2)$ and R from deep inelastic muon scattering at high Q^2 , *Phys. Lett. B* **223**, 485 (1989).
- [64] C. Adloff *et al.* (H1), Deep inelastic inclusive ep scattering at low x and a determination of α_S , *Eur. Phys. J. C* **21**, 33 (2001), [arXiv:hep-ex/0012053](#).
- [65] S. Chekanov *et al.* (ZEUS), Measurement of the neutral current cross-section and F_2 structure function for deep inelastic $e + p$ scattering at HERA, *Eur. Phys. J. C* **21**, 443 (2001), [arXiv:hep-ex/0105090](#).
- [66] F. James and M. Roos, MINUIT - a system for function minimization and analysis of the parameter errors and correlations, *Comput. Phys. Commun.* **10**, 343 (1975).
- [67] A. Airapetian *et al.* (HERMES), Inclusive measurements of inelastic electron and positron scattering from unpolarized hydrogen and deuterium targets, *JHEP* **05**, 126, [arXiv:1103.5704](#).
- [68] Y. Liang, *Measurement of $R = \sigma_L/\sigma_T$ in the nucleon resonance region*, *Ph.D. thesis*, American University (2003).
- [69] S. Malace, *Measurements of Inclusive Resonance Cross Sections for Quark-Hadron Duality Studies*, *Ph.D. thesis*, Hampton University (2006).

SUPPLEMENTAL MATERIAL

In the figures below we provide a detailed comparison of our model predictions with the hydrogen photoproduction and electroproduction cross section data. Figure 12 shows the total photoproduction cross section vs W^2 . The data points are from the experiments listed in Table III and the legend is given in the figure. The solid line corresponds to our predictions with the best fit parameters (see Sec. IV), while the dotted line shows the background part of the cross section. In Fig. 13 to 42 we show our results (solid line) in comparison with electroproduction cross section data from experiments listed in Table II. The figures are organized in terms of panels of given beam energy and scattering angle whose values are shown in the panels. The data points for the resonance region ($W^2 < 4 \text{ GeV}^2$) and DIS ($W^2 > 4 \text{ GeV}^2$) are marked with different symbols/color. The error bars in the plots are the quadrature sum of statistical and systematic errors of corresponding experiment, the normalization uncertainties of data are not shown.

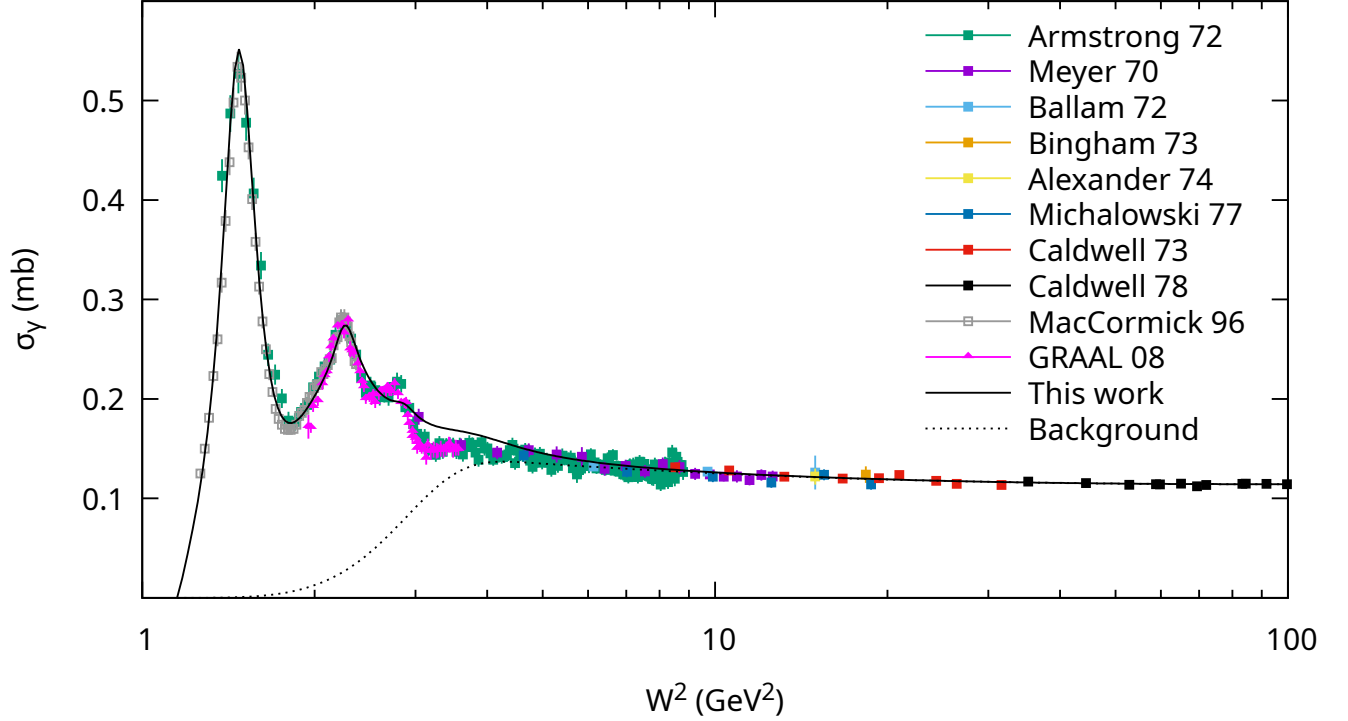


FIG. 12. Model predictions (solid line) in comparison with data on the total photoproduction cross section off hydrogen vs W^2 . The legend of various photoproduction data is given in the figure.

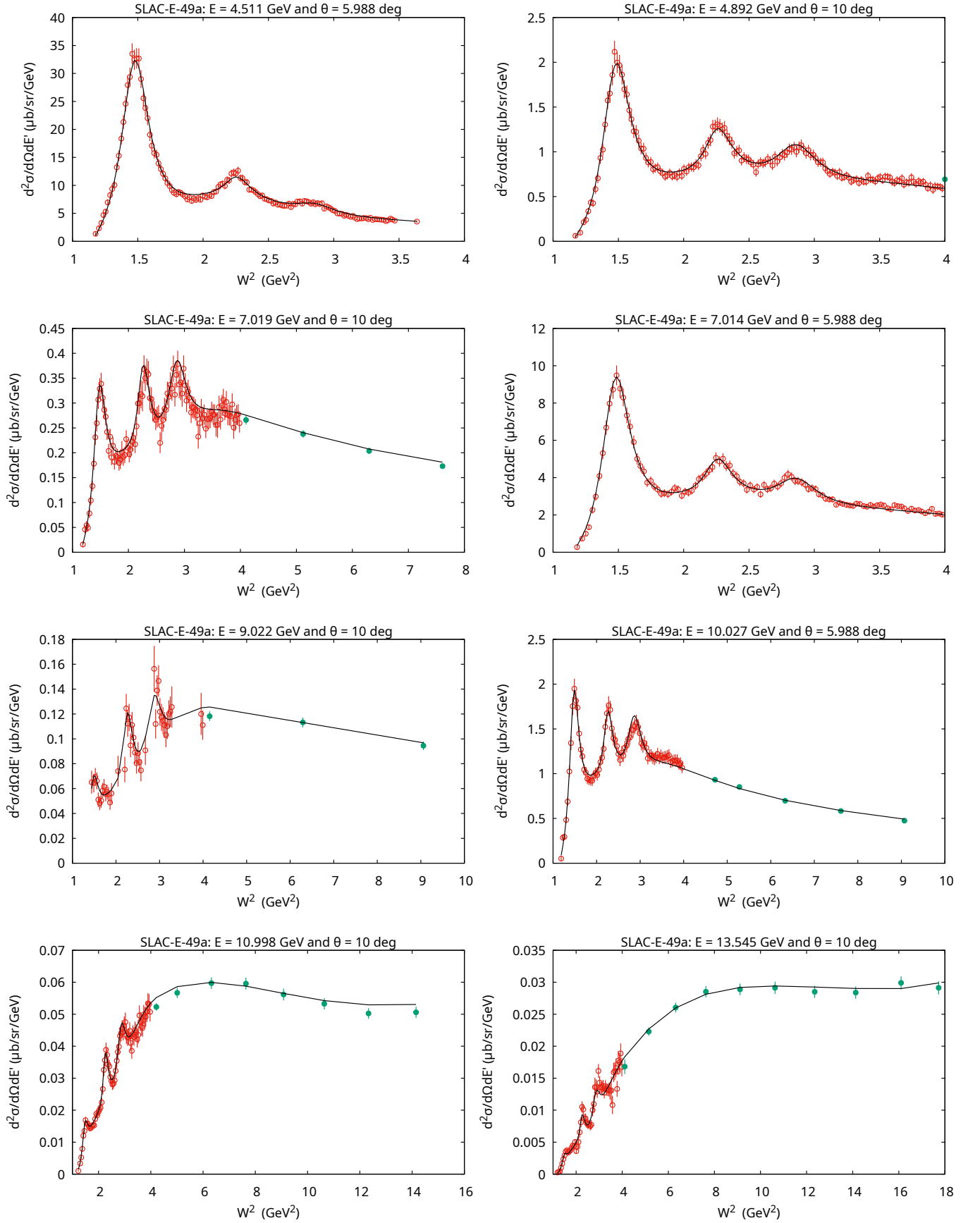


FIG. 13. Model predictions (solid line) in comparison with SLAC-E-49a data on differential cross section $d^2\sigma/(d\Omega dE')$ in $\mu\text{b}/(\text{sr}/\text{GeV})$ vs W^2 in GeV^2 . The values of the beam energy (GeV) and scattering angle (degrees) are given in the figure panels.

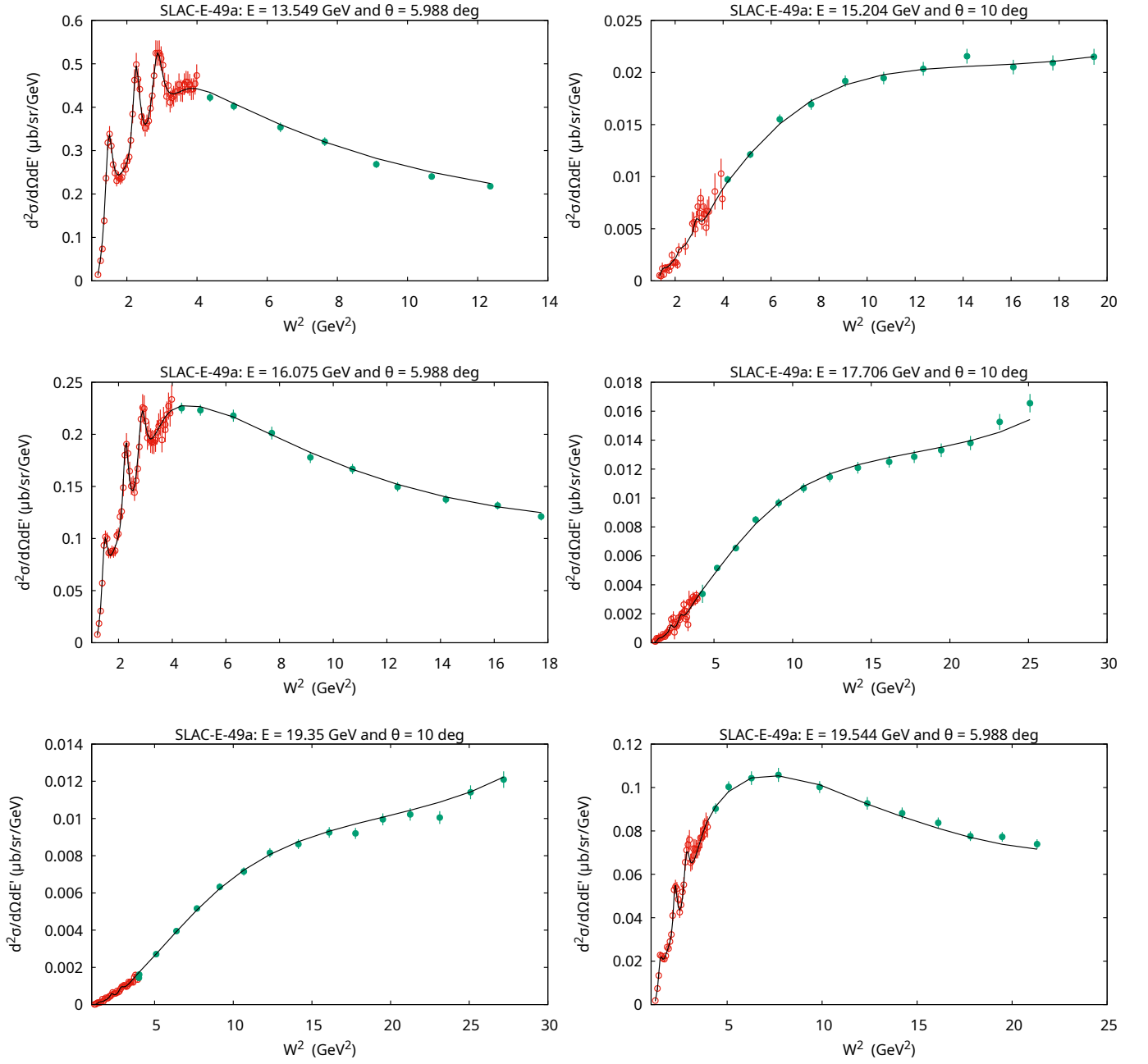


FIG. 14. Similar to Fig. 13.

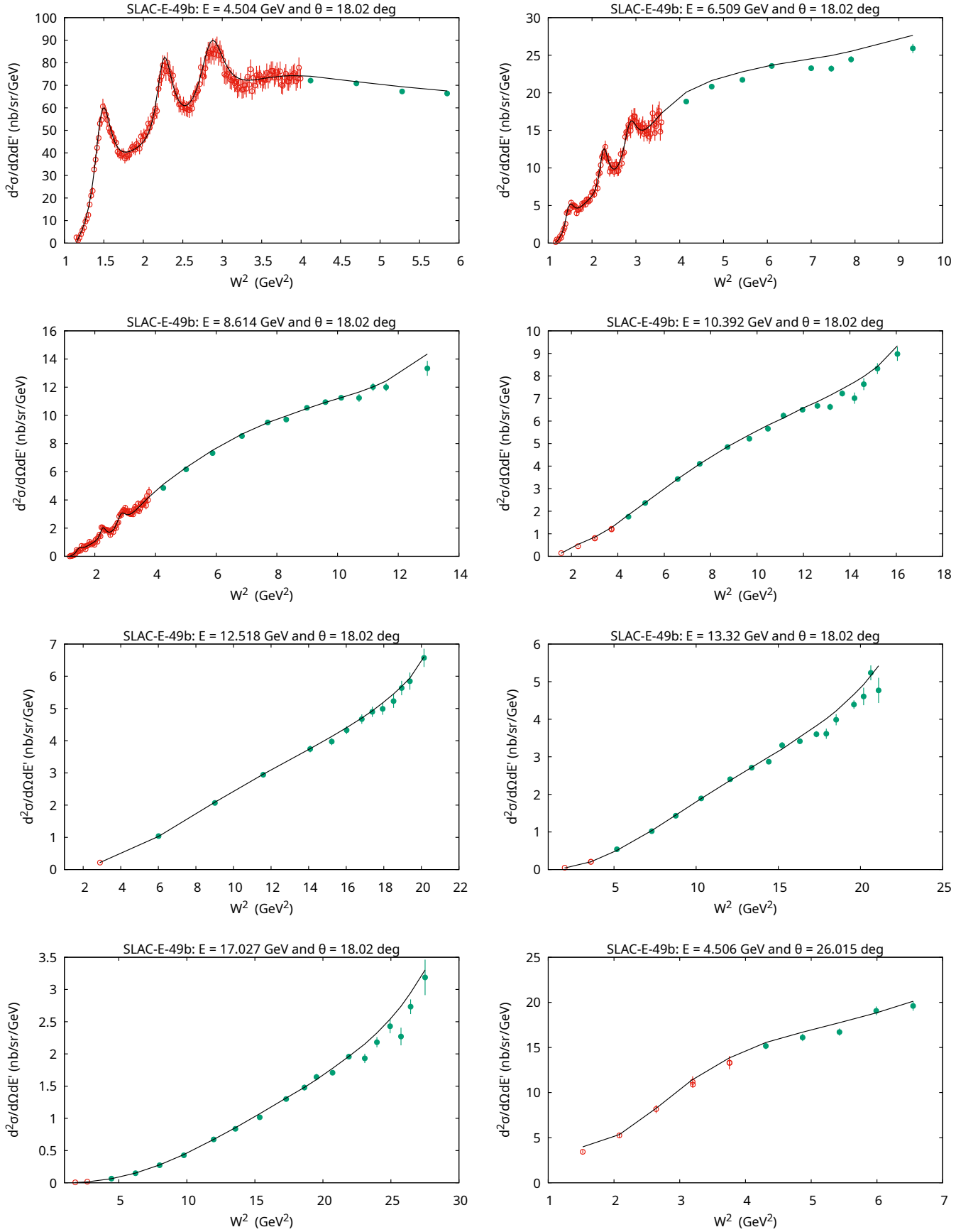


FIG. 15. Model predictions (solid line) in comparison with SLAC-E-49b data on differential cross section $d^2\sigma/(d\Omega dE')$ in nanobarn/(sr GeV) vs W^2 in GeV^2 . The values of the beam energy (GeV) and scattering angle (degrees) are given in the figure panels.

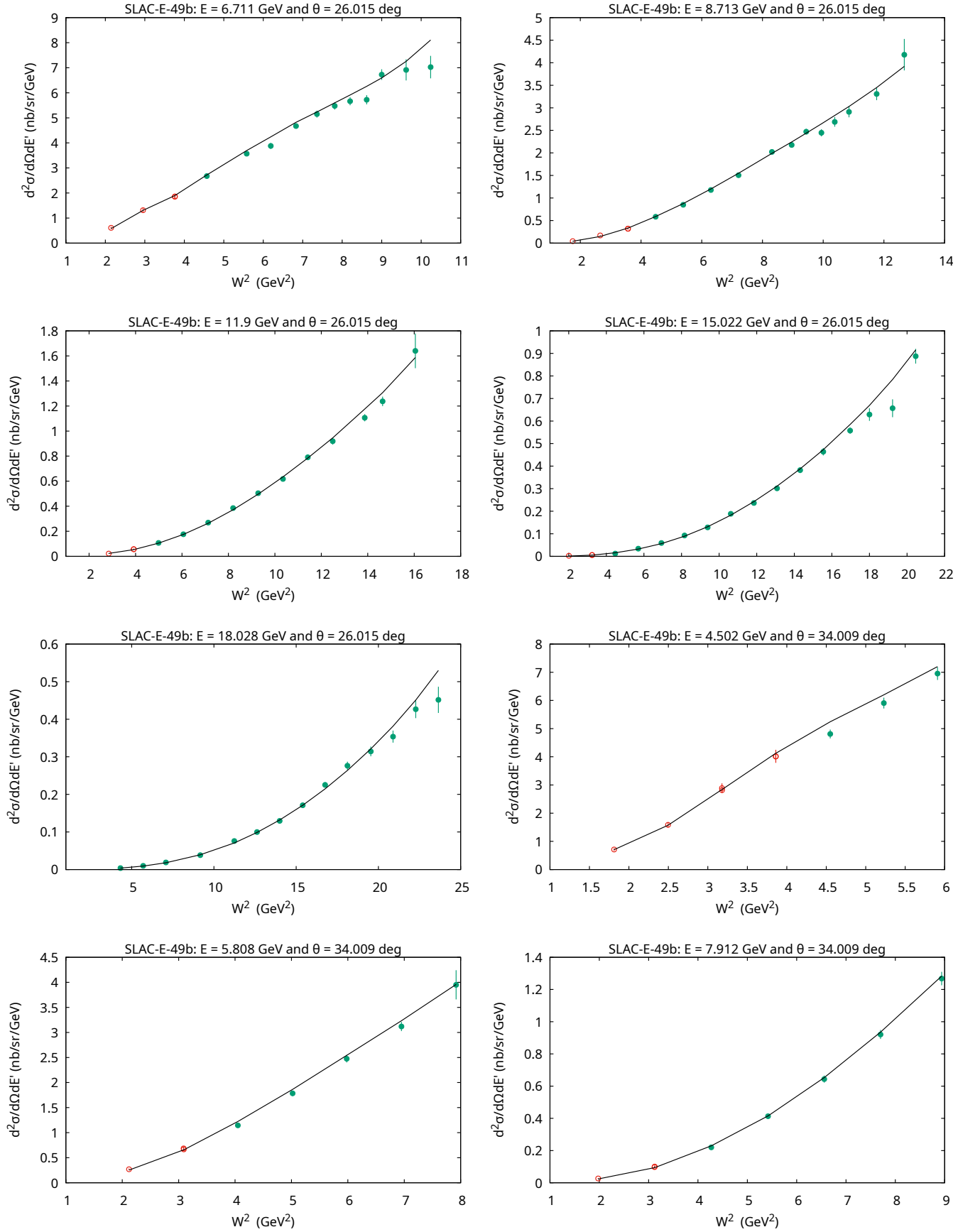


FIG. 16. Similar to Fig. 15.

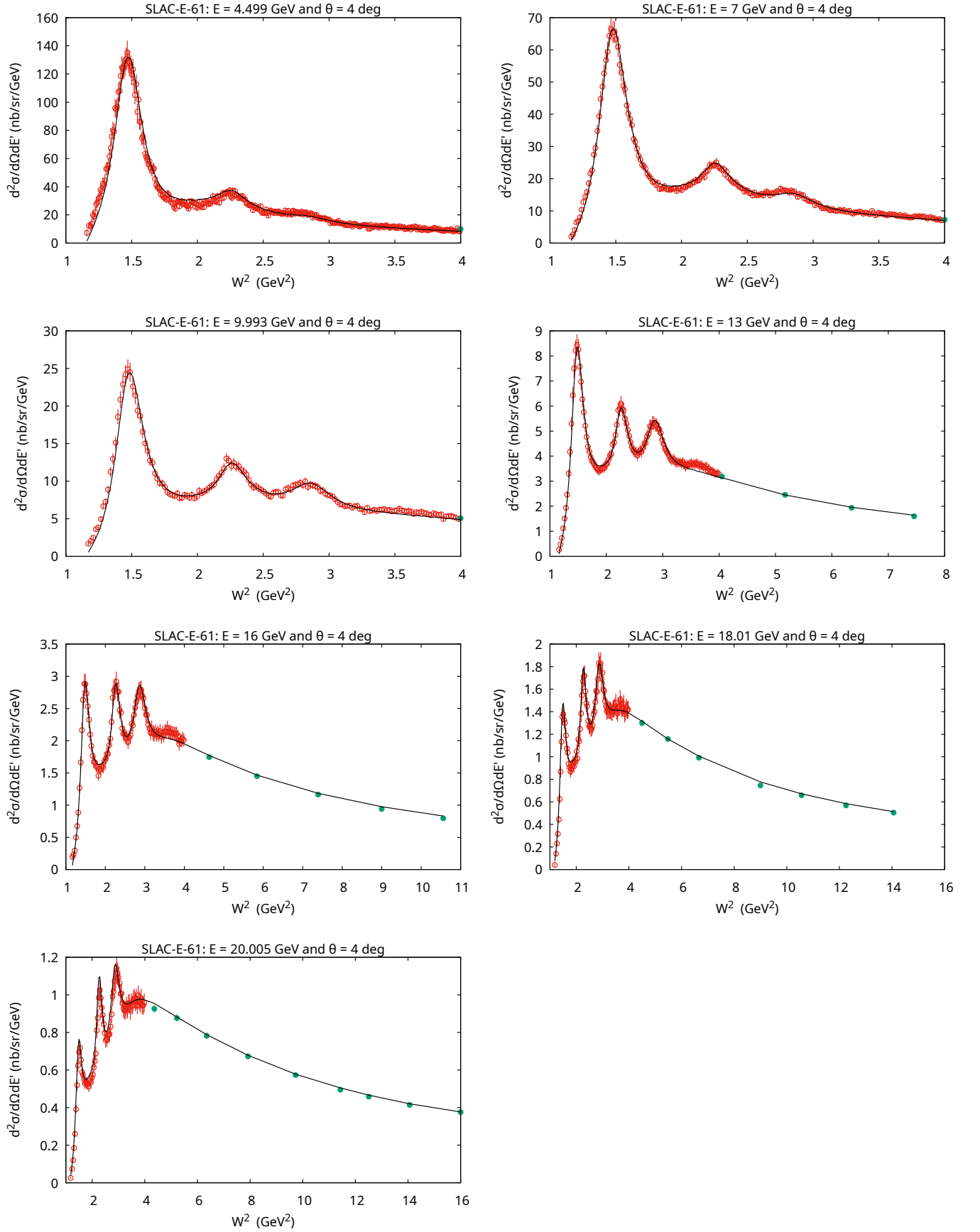


FIG. 17. Model predictions (solid line) in comparison with SLAC-E-61 data on differential cross section $d^2\sigma/(d\Omega dE')$ in nanobarn/(sr GeV) vs W^2 in GeV^2 . The values of the beam energy (GeV) and scattering angle (degrees) are given in the figure panels.

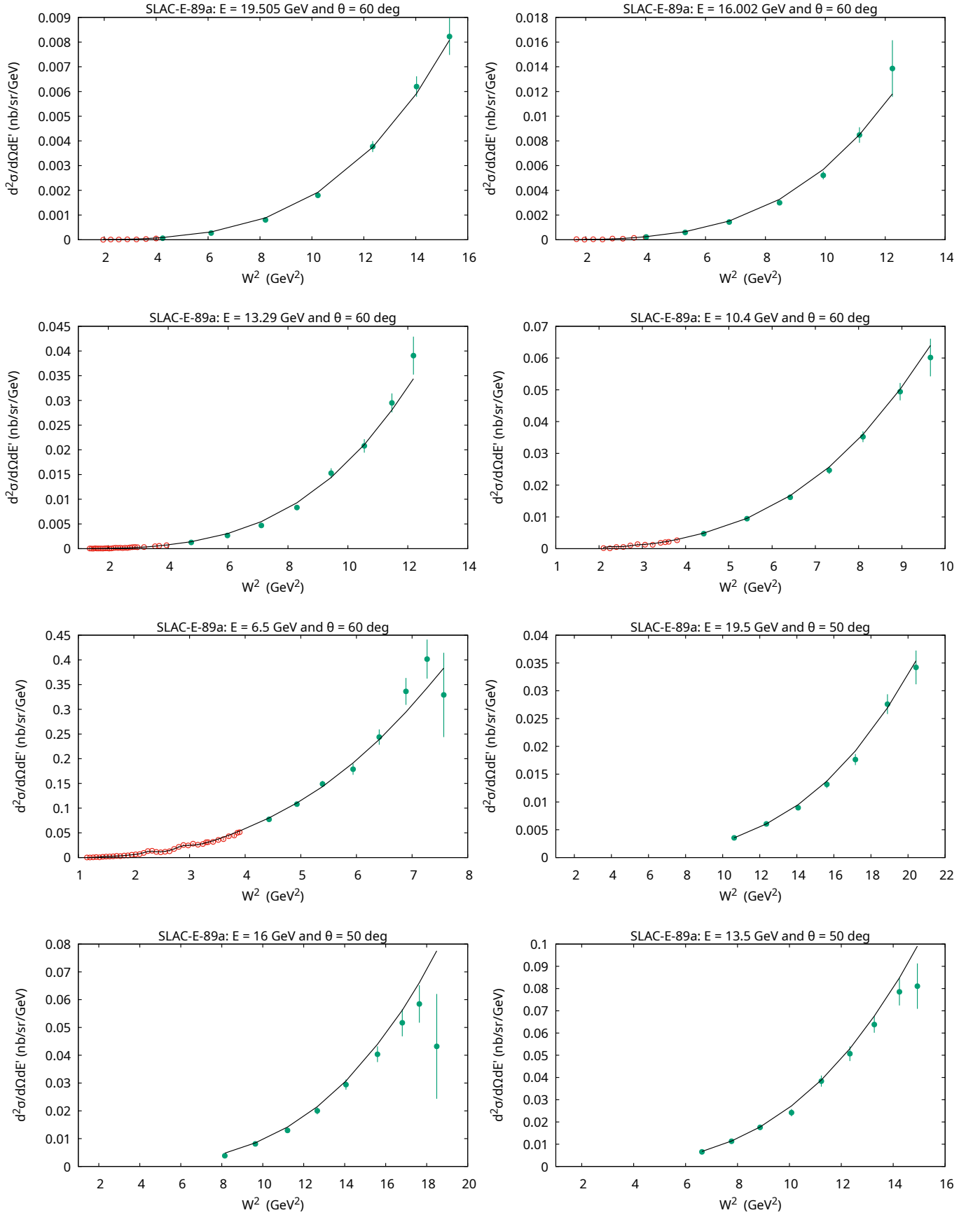


FIG. 18. Model predictions (solid line) in comparison with SLAC-E-89a data on differential cross section $d^2\sigma/(d\Omega dE')$ in nanobarn/(sr GeV) vs W^2 in GeV^2 . The values of the beam energy (GeV) and scattering angle (degrees) are given in the figure panels.

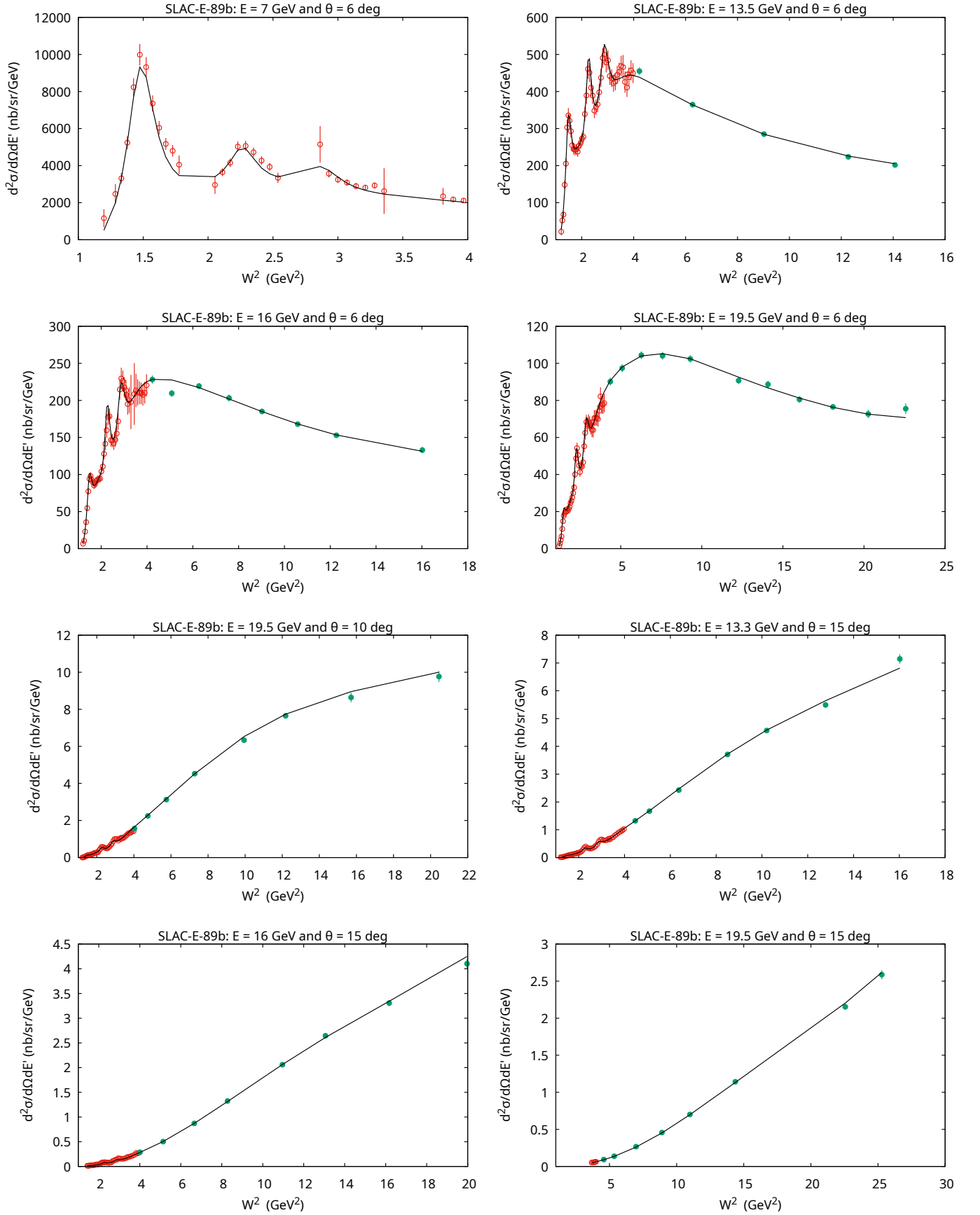


FIG. 19. Model predictions (solid line) in comparison with SLAC-E-89b data on differential cross section $d^2\sigma/(d\Omega dE')$ in nanobarn/(sr GeV) vs W^2 in GeV². The values of the beam energy (GeV) and scattering angle (degrees) are given in the figure panels.

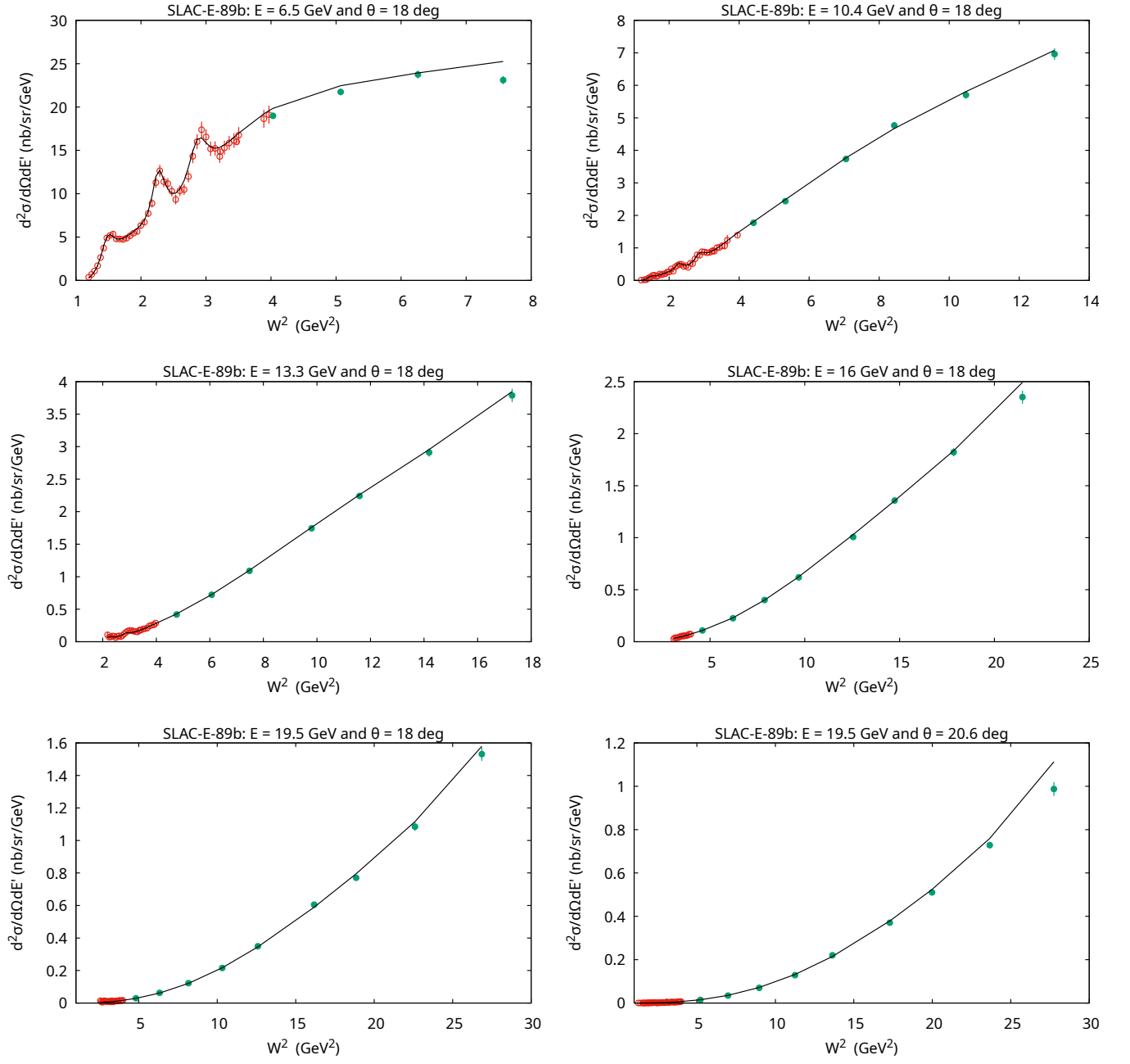


FIG. 20. Similar to Fig. 19.

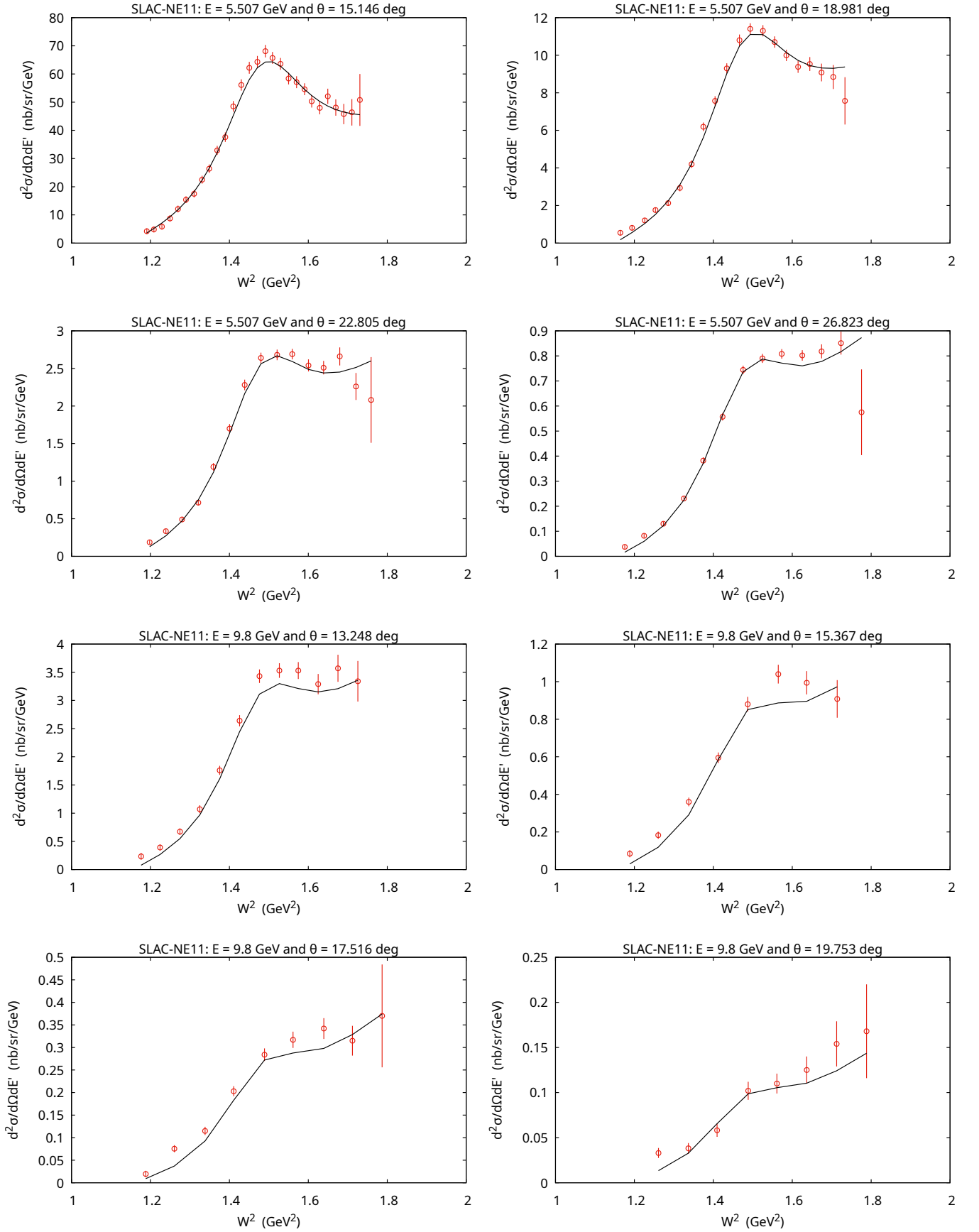


FIG. 21. Model predictions (solid line) in comparison with SLAC-NE11 data on differential cross section $d^2\sigma/(d\Omega dE')$ in nanobarn/(sr GeV) vs W^2 in GeV^2 . The values of the beam energy (GeV) and scattering angle (degrees) are given in the figure panels.

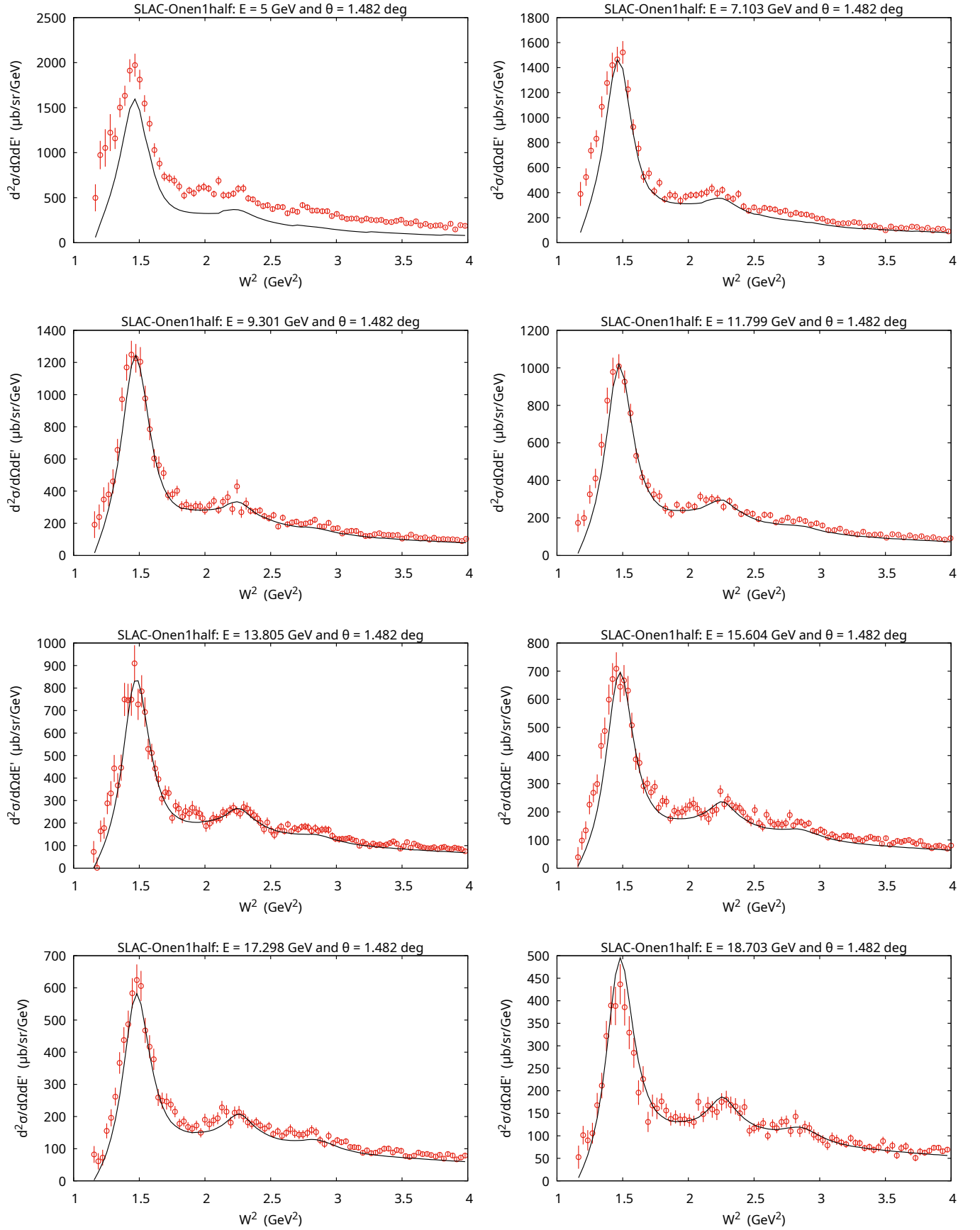


FIG. 22. Model predictions (solid line) in comparison with SLAC-Onen1half data on differential cross section $d^2\sigma/(d\Omega dE')$ in $\mu\text{b}/(\text{sr GeV})$ vs W^2 in GeV^2 . The values of the beam energy (GeV) and scattering angle (degrees) are given in the figure panels.

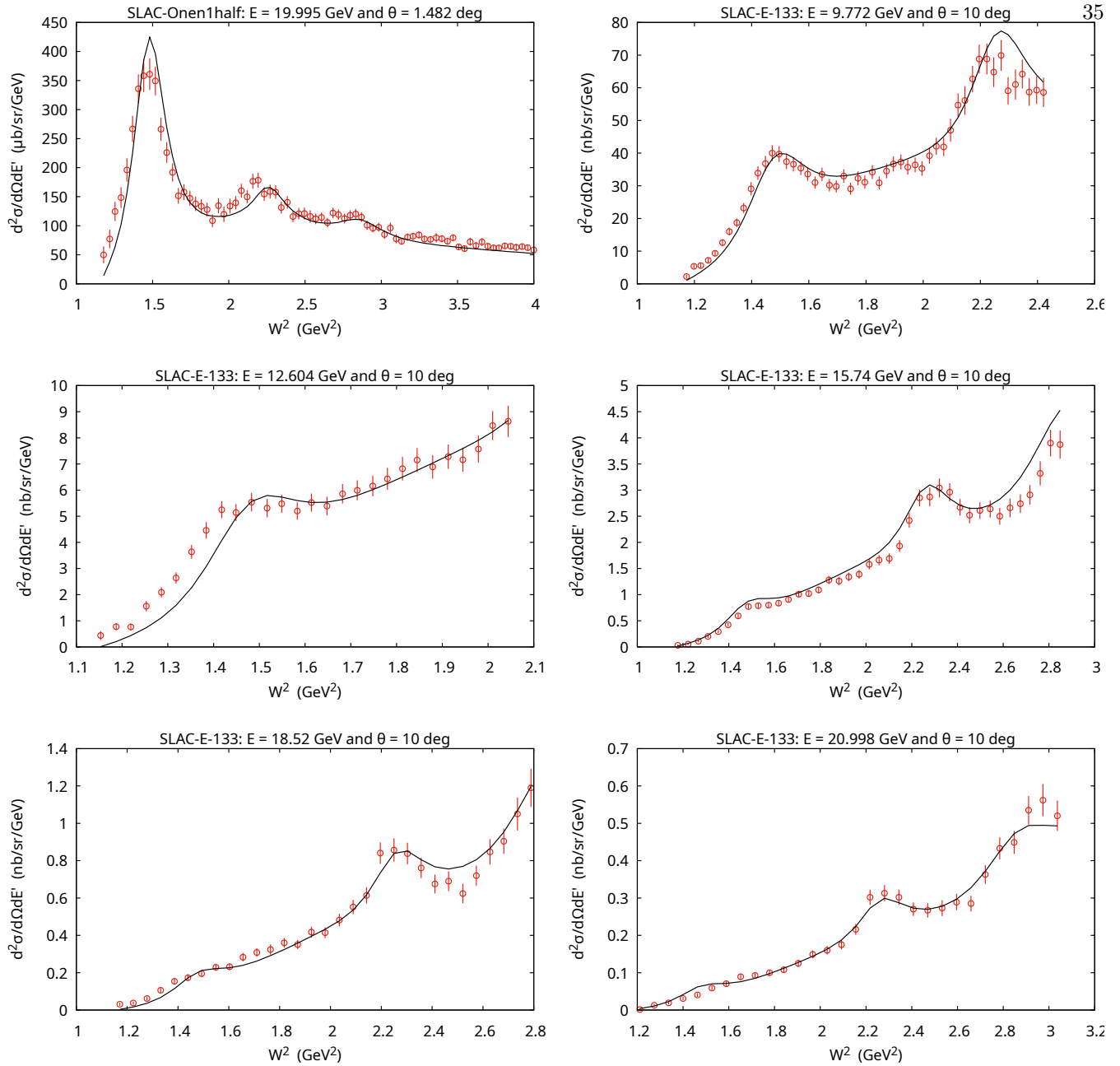


FIG. 23. Model predictions (solid line) in comparison with SLAC-E-133 data on differential cross section $d^2\sigma/(d\Omega dE')$ in nanobarn/(sr GeV) vs W^2 in GeV^2 . The values of the beam energy (GeV) and scattering angle (degrees) are given in the figure panels.

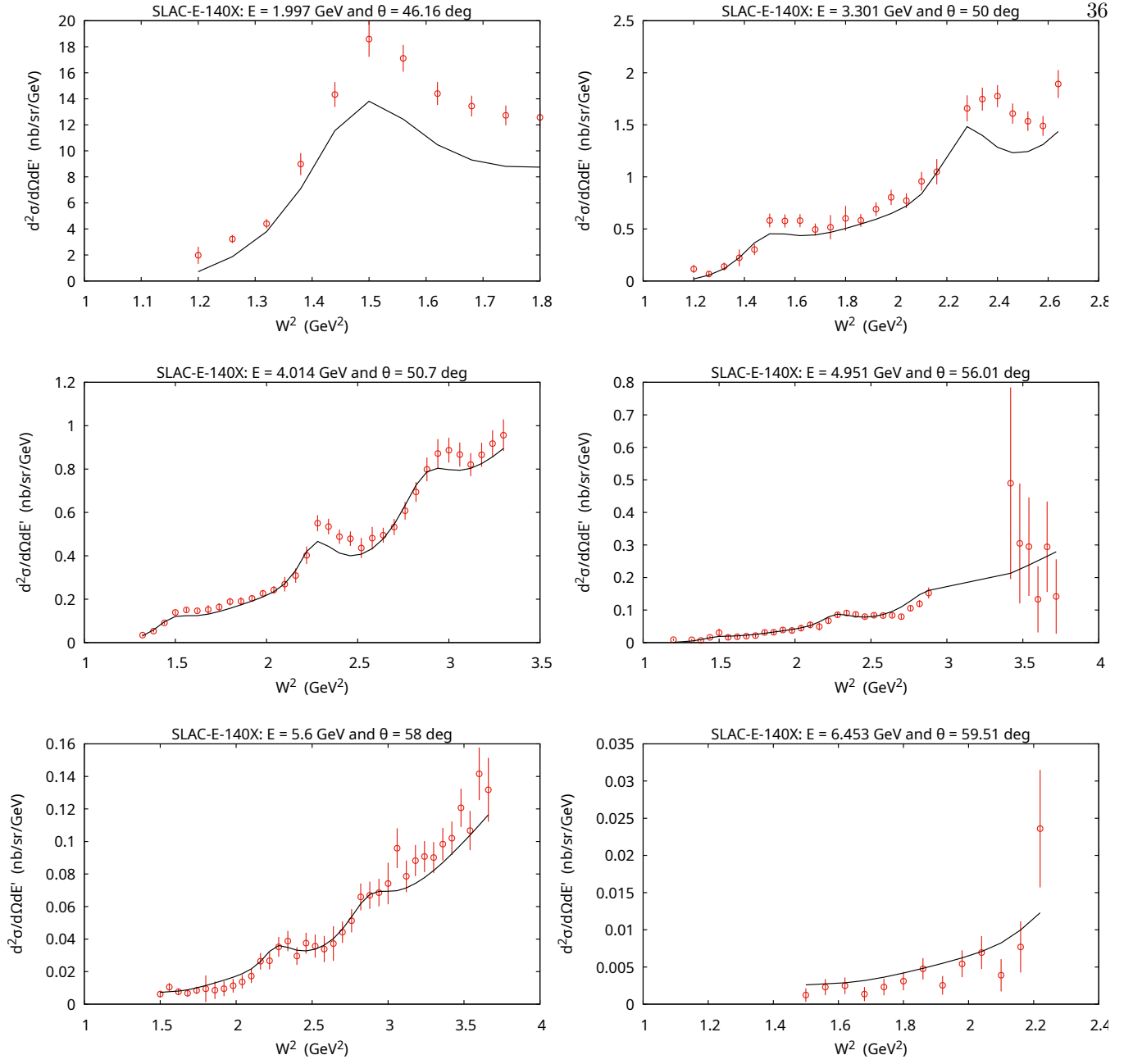


FIG. 24. Model predictions (solid line) in comparison with SLAC-E-140X data on differential cross section $d^2\sigma/(d\Omega dE')$ in nanobarn/(sr GeV) vs W^2 in GeV^2 . The values of the beam energy (GeV) and scattering angle (degrees) are given in the figure panels.

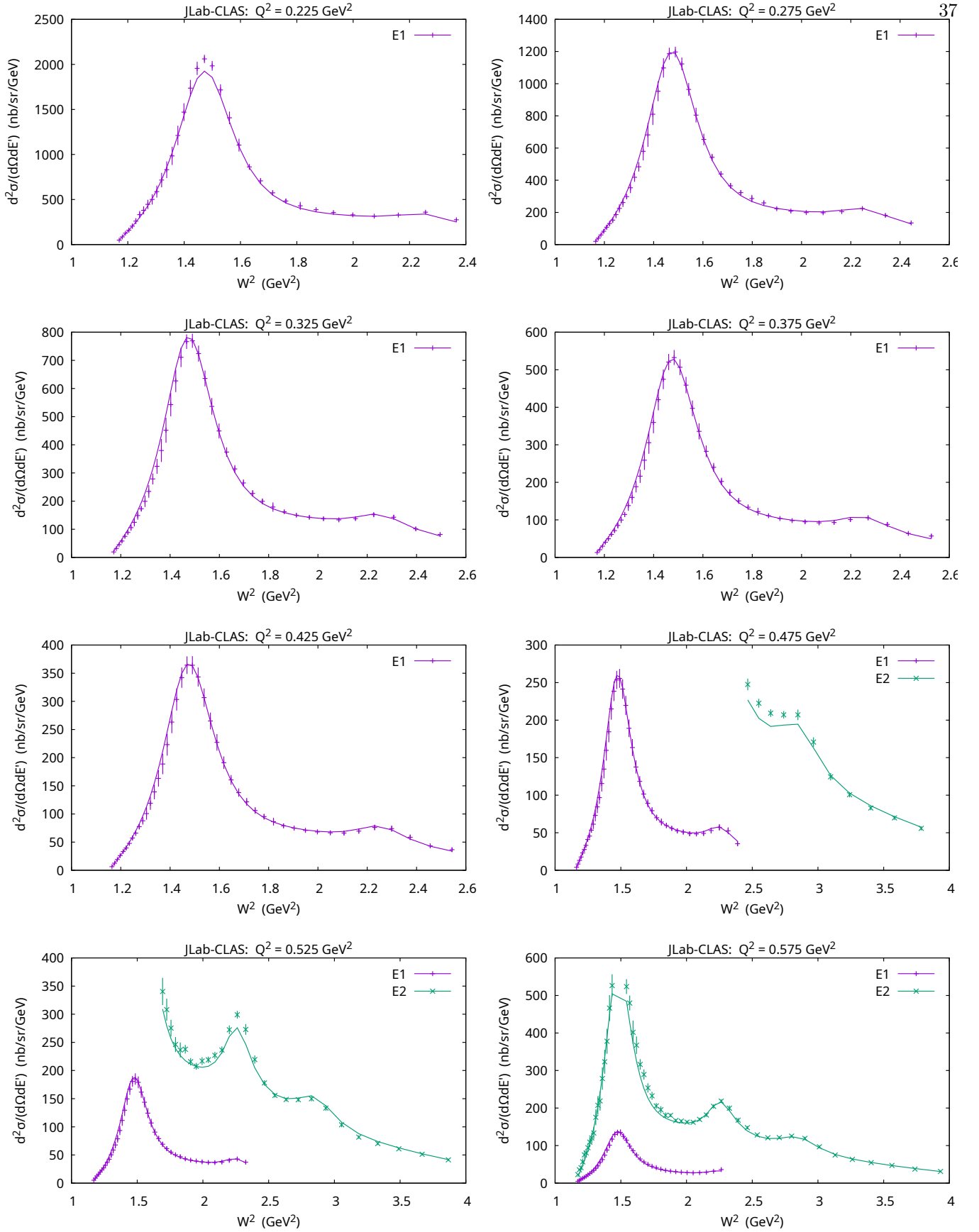


FIG. 25. Model predictions (solid lines) in comparison with JLab-CLAS data on differential cross section $d^2\sigma/(d\Omega dE')$ in nanobarn/(sr GeV) vs W^2 in GeV^2 . The values of Q^2 are given in the figure panels. The data sets E1, E2, E3, E4, and E5 correspond to the beam energies 1.515, 2.567, 4.056, 4.247, and 4.462 GeV, respectively.

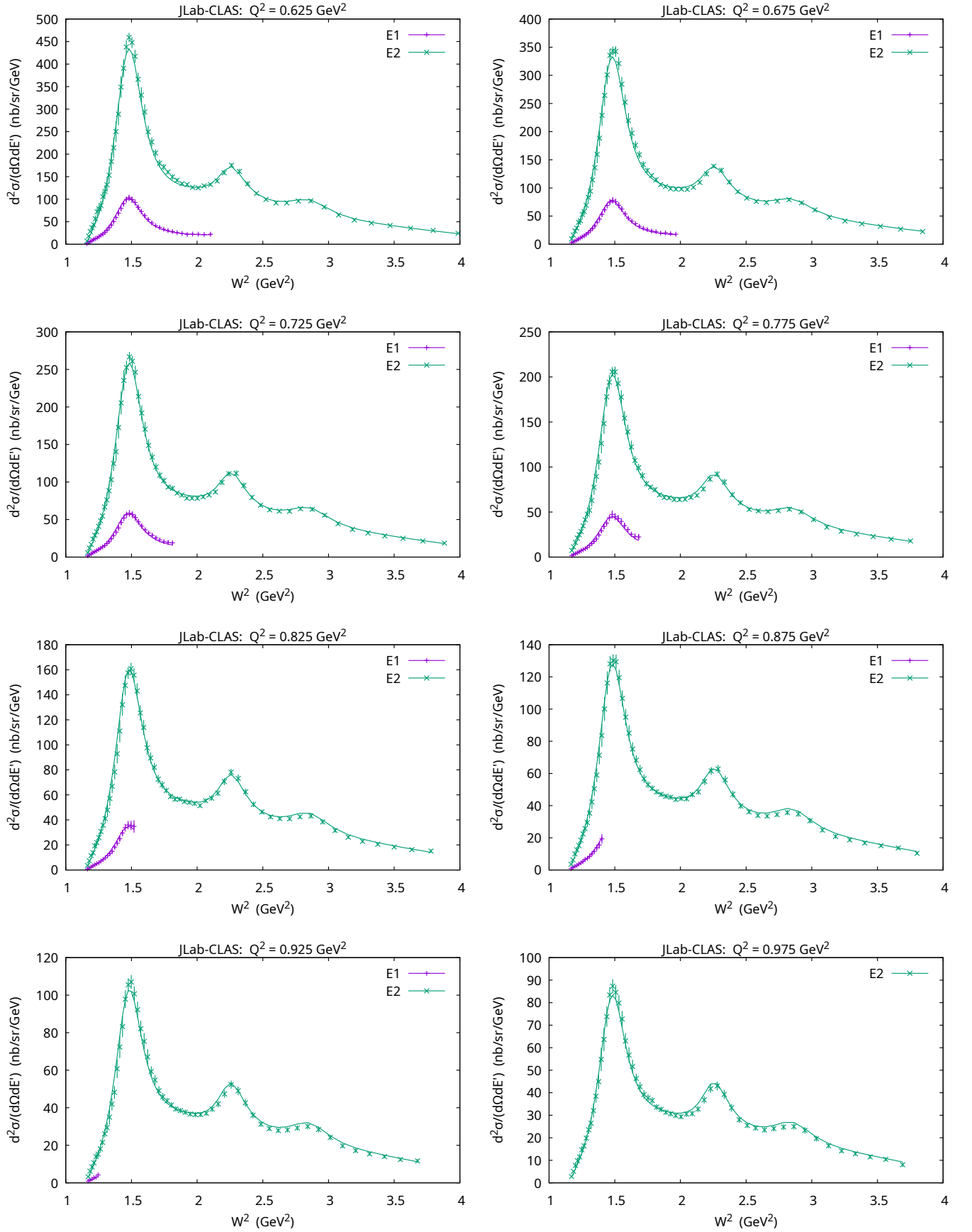


FIG. 26. Similar to Fig. 25.

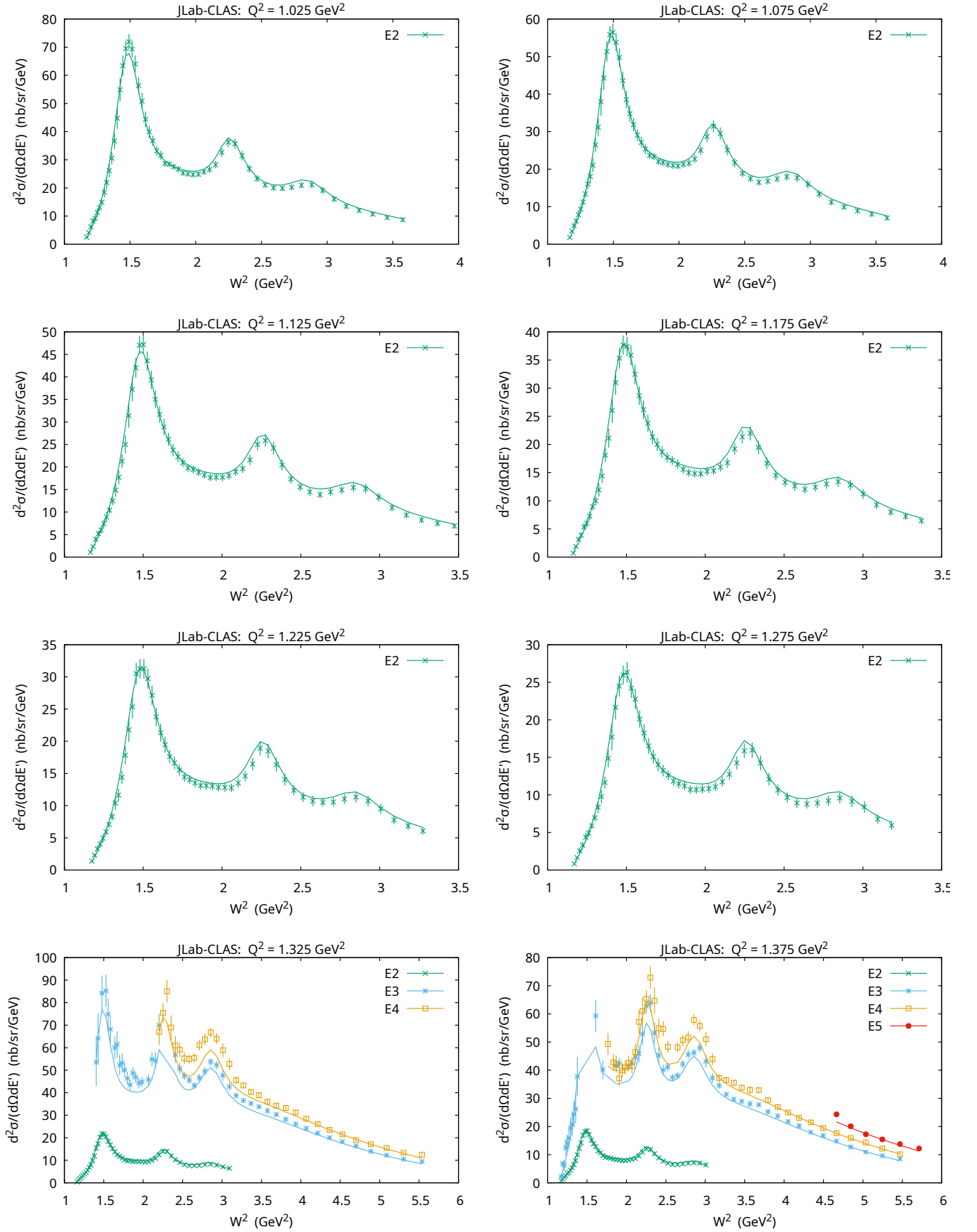


FIG. 27. Similar to Fig. 25.

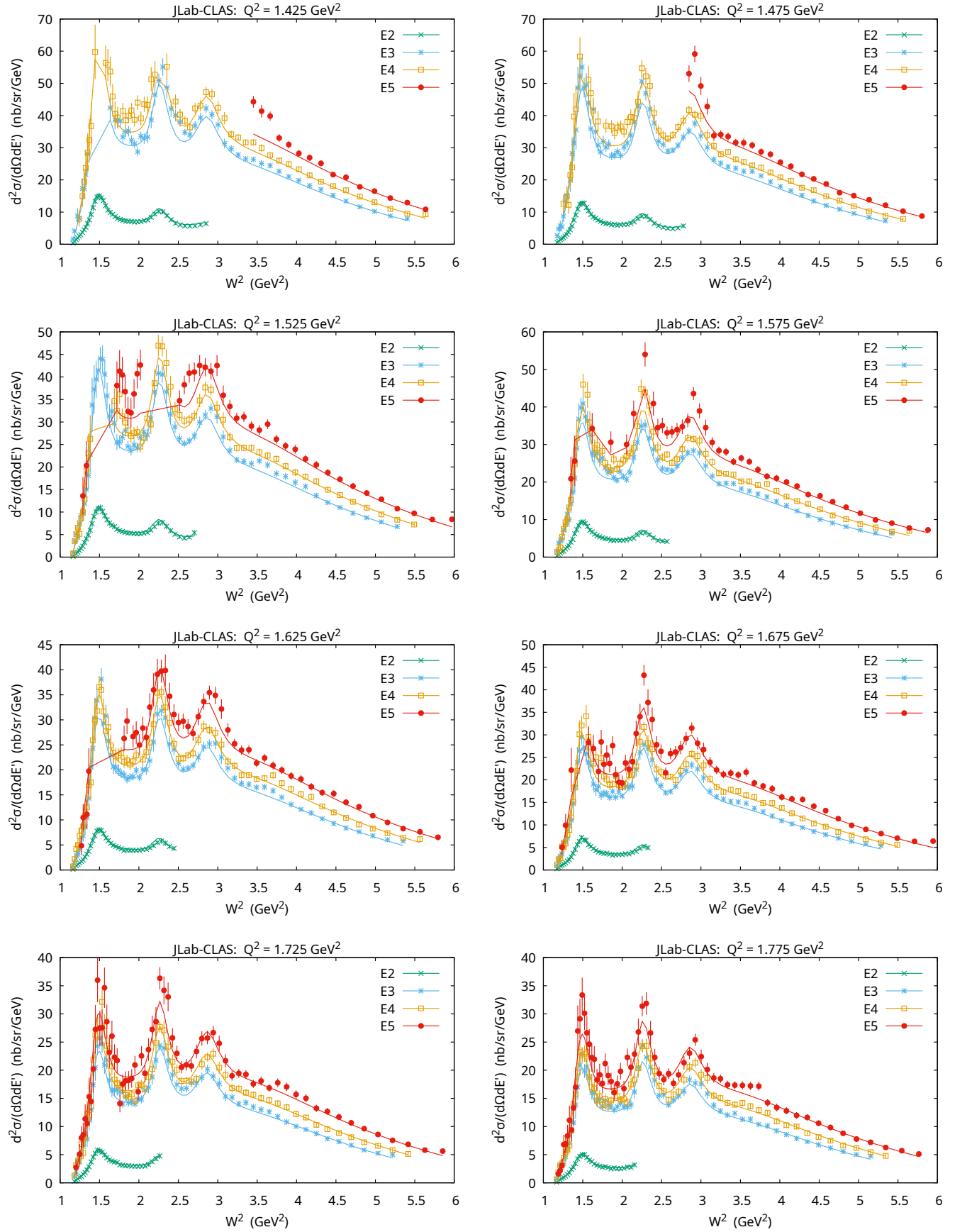


FIG. 28. Similar to Fig. 25.

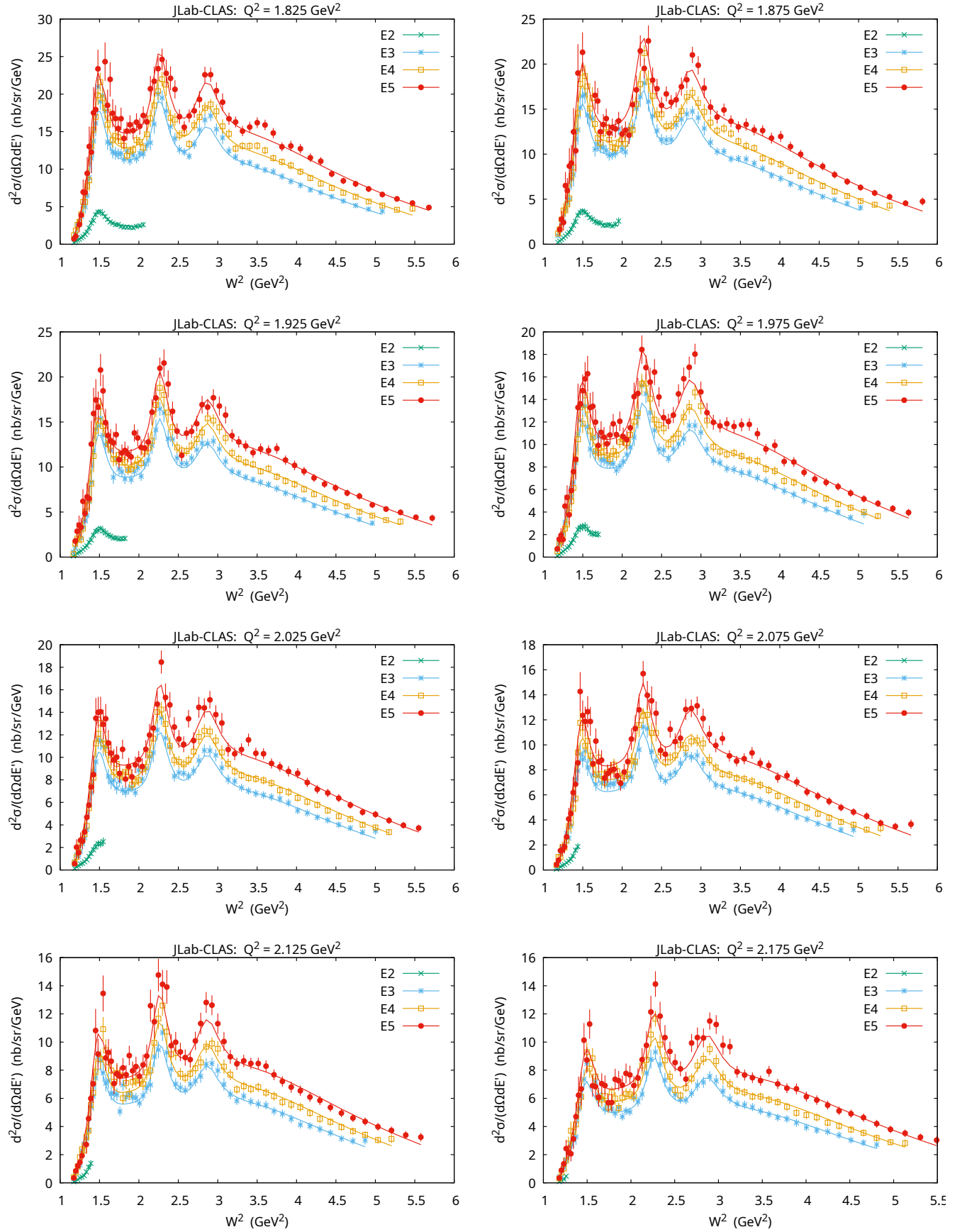


FIG. 29. Similar to Fig. 25.

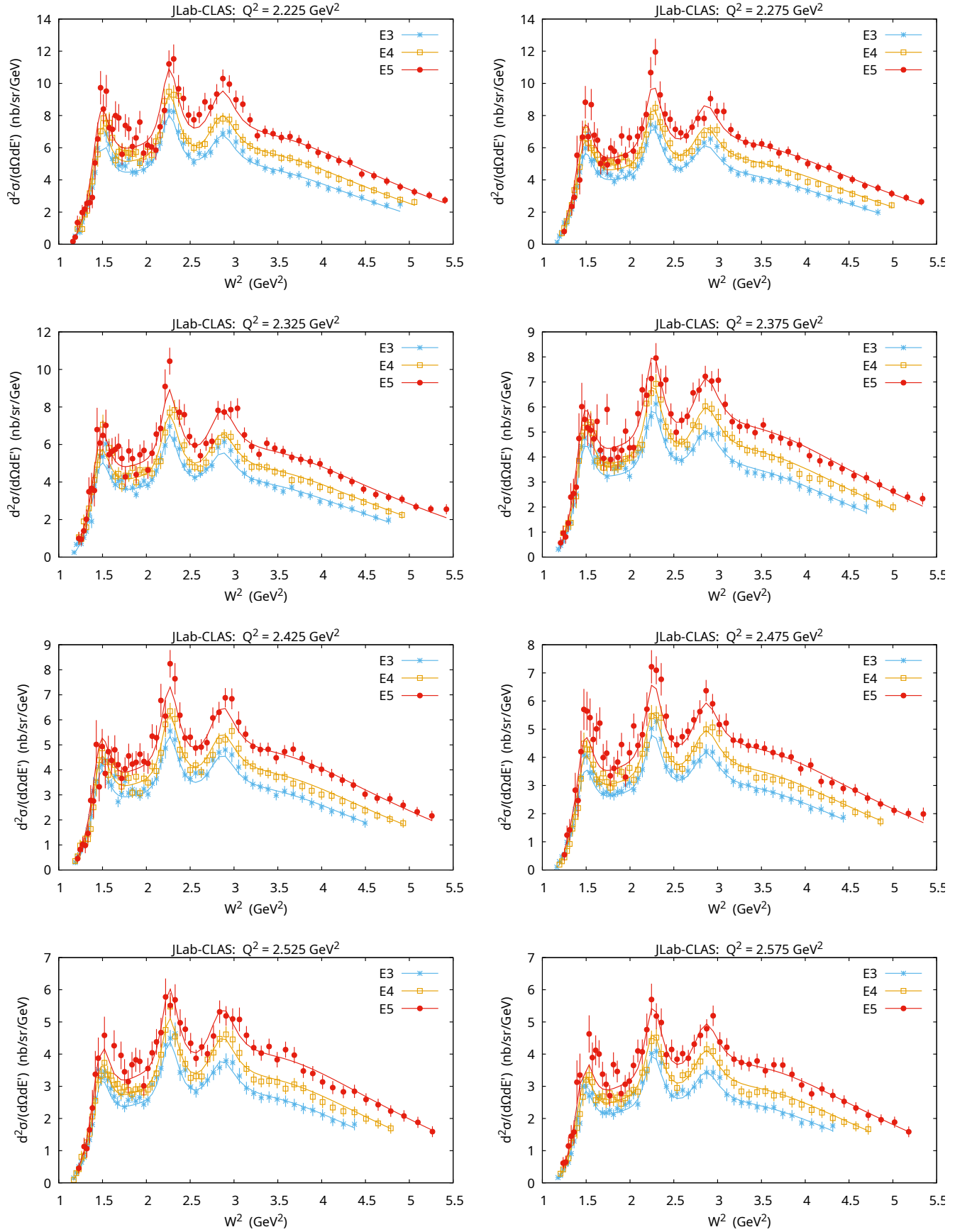


FIG. 30. Similar to Fig. 25.

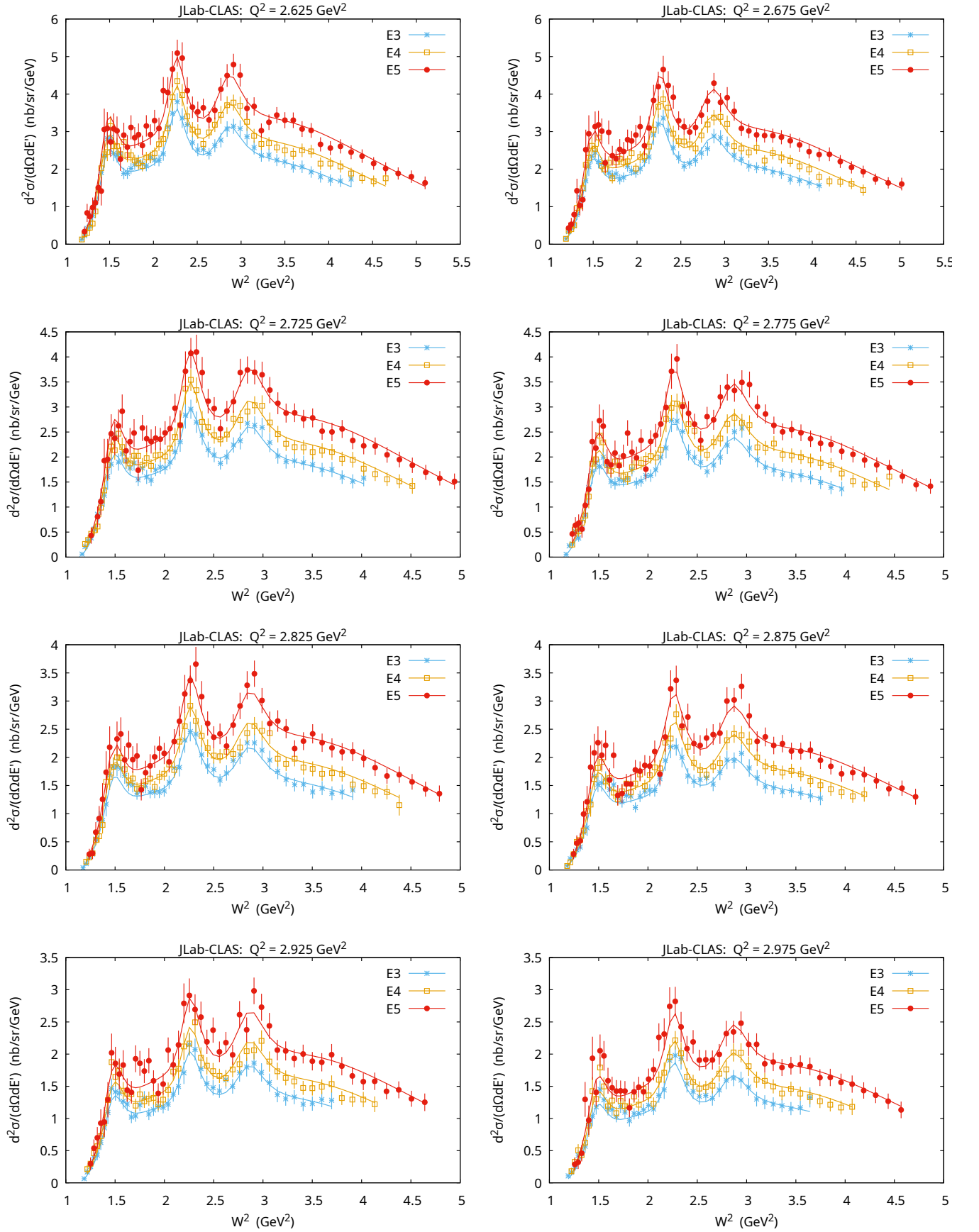


FIG. 31. Similar to Fig. 25.

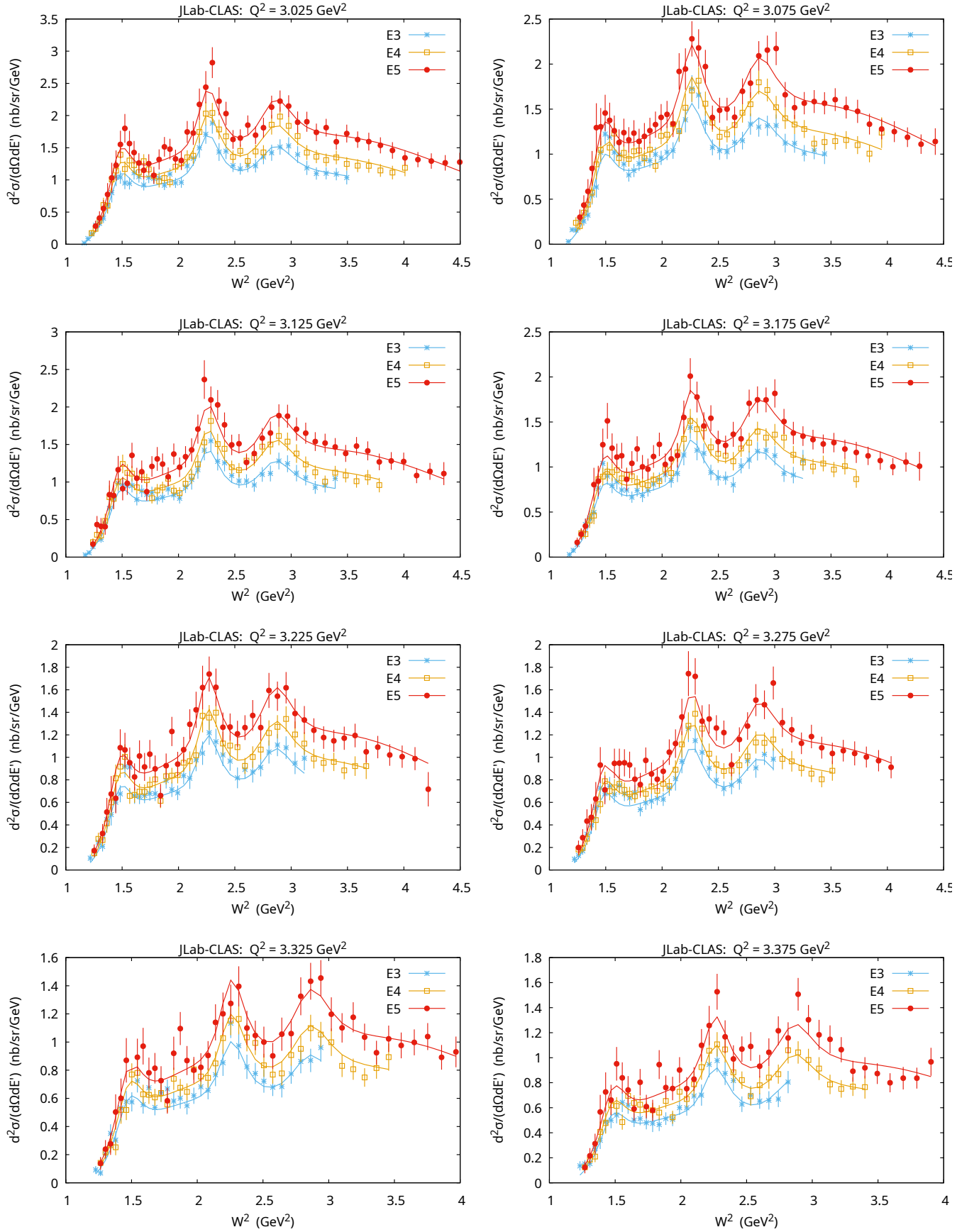


FIG. 32. Similar to Fig. 25.

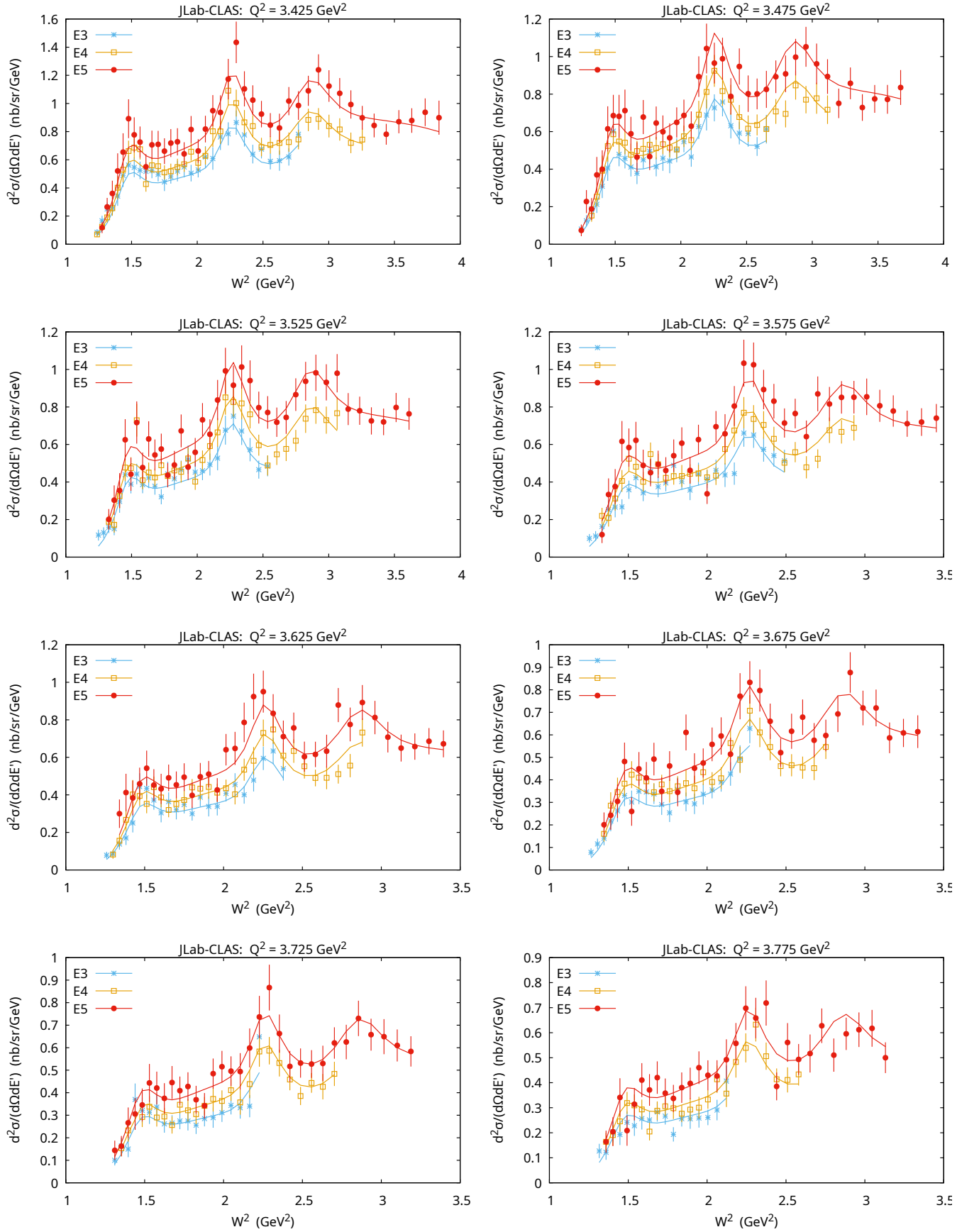


FIG. 33. Similar to Fig. 25.

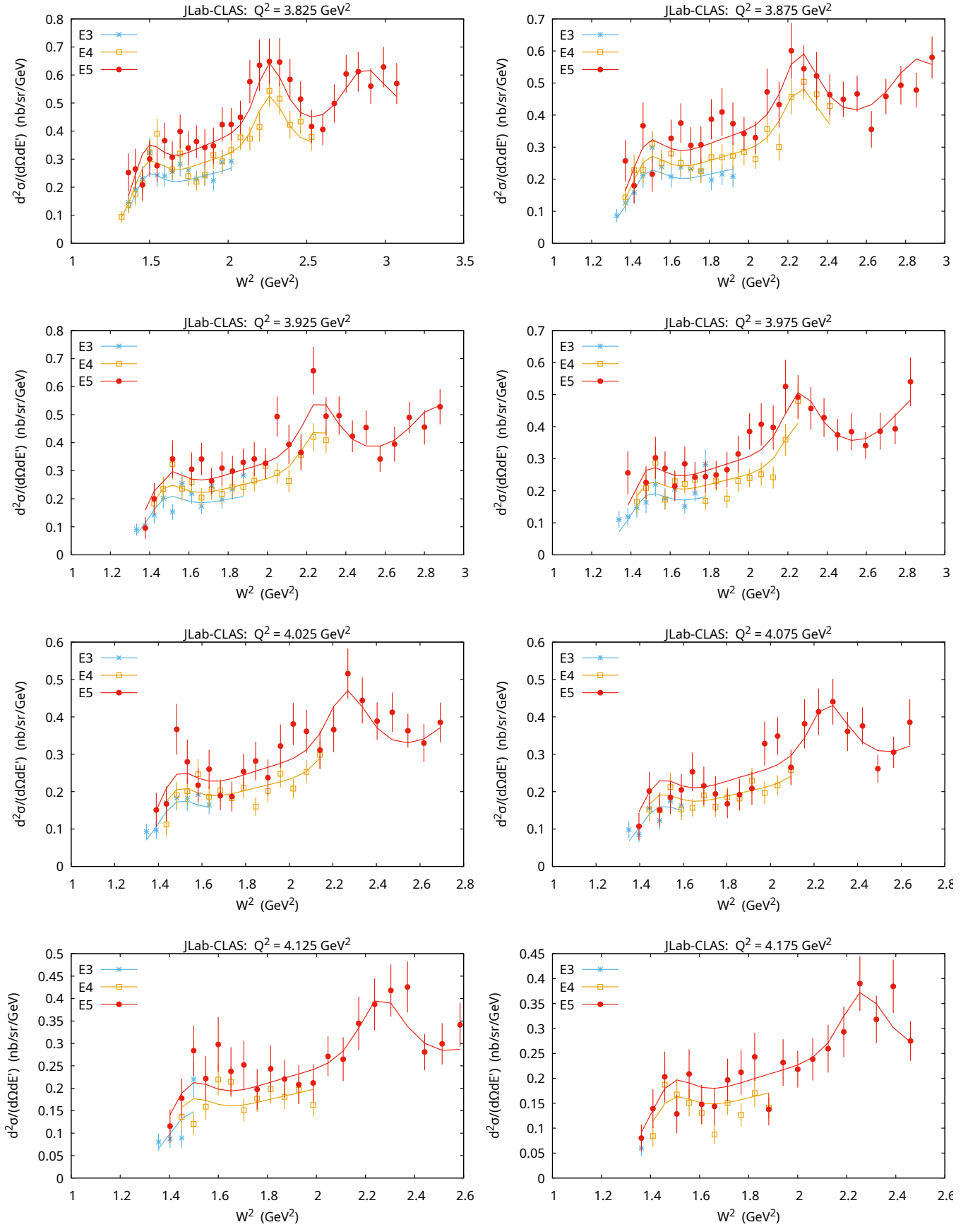


FIG. 34. Similar to Fig. 25.

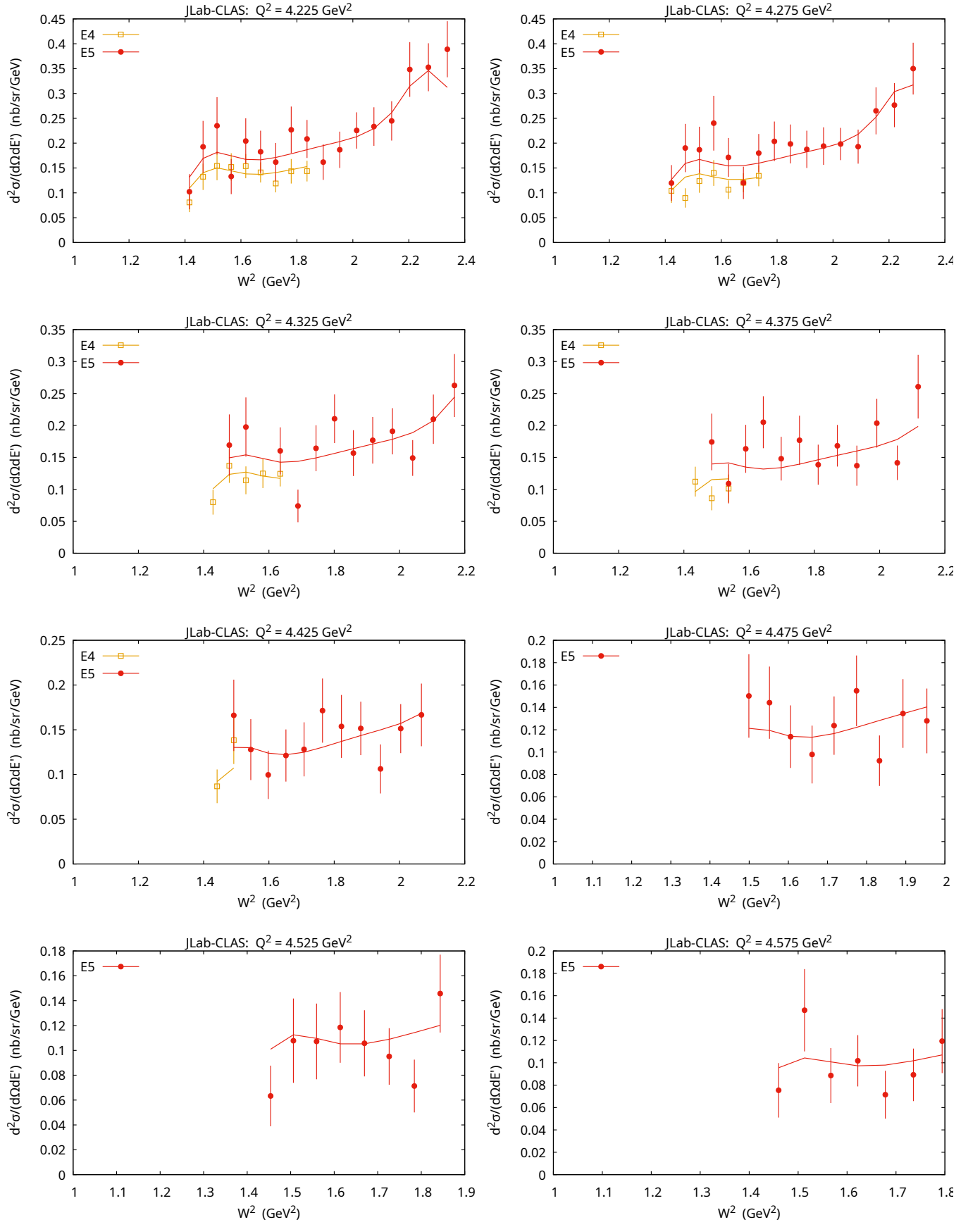


FIG. 35. Similar to Fig. 25.

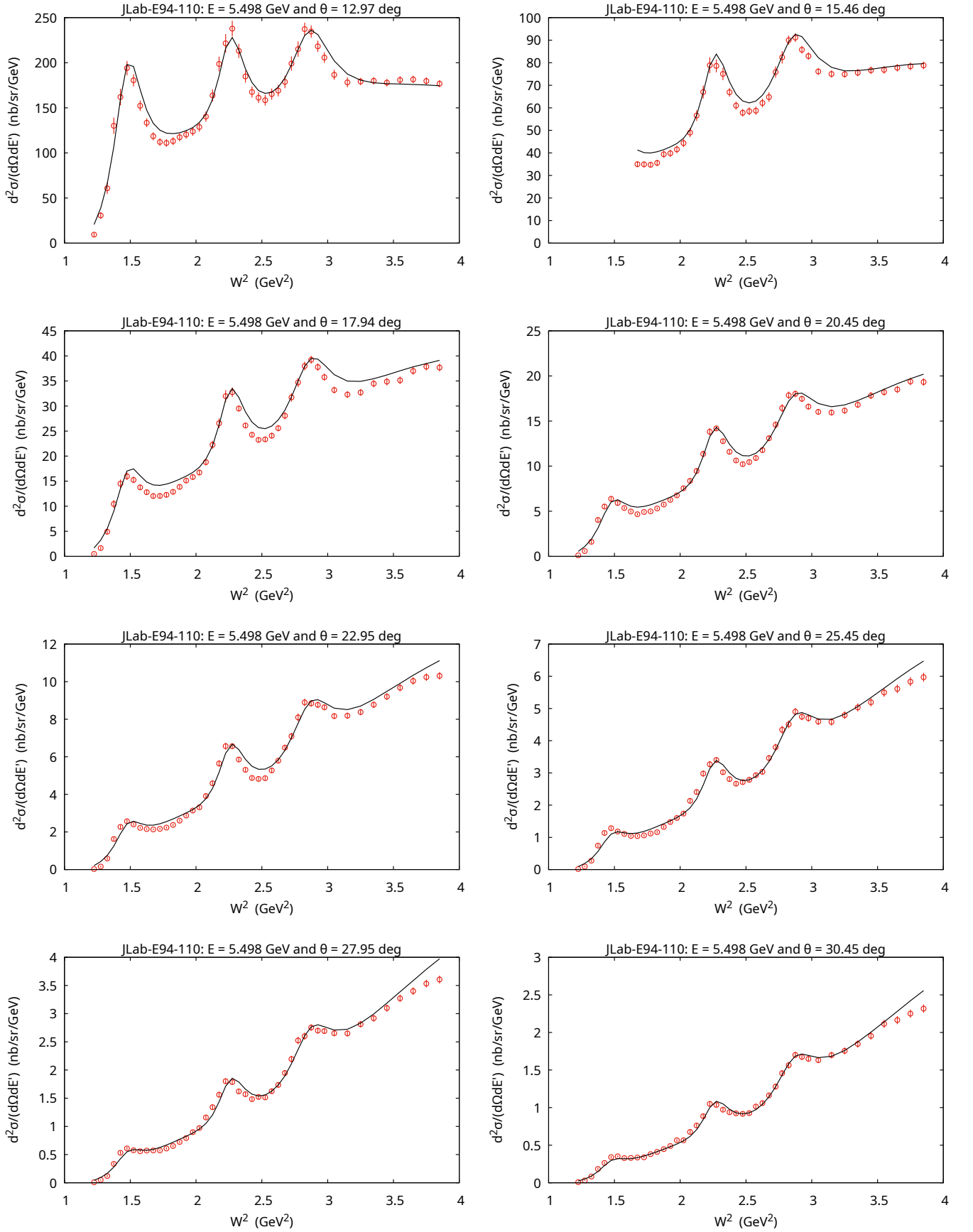


FIG. 36. Model predictions (solid line) in comparison with JLab-E94-110 data on differential cross section $d^2\sigma/(d\Omega dE')$ in nanobarn/(sr GeV) vs W^2 in GeV^2 . The values of the beam energy (GeV) and scattering angle (degrees) are given in the figure panels.

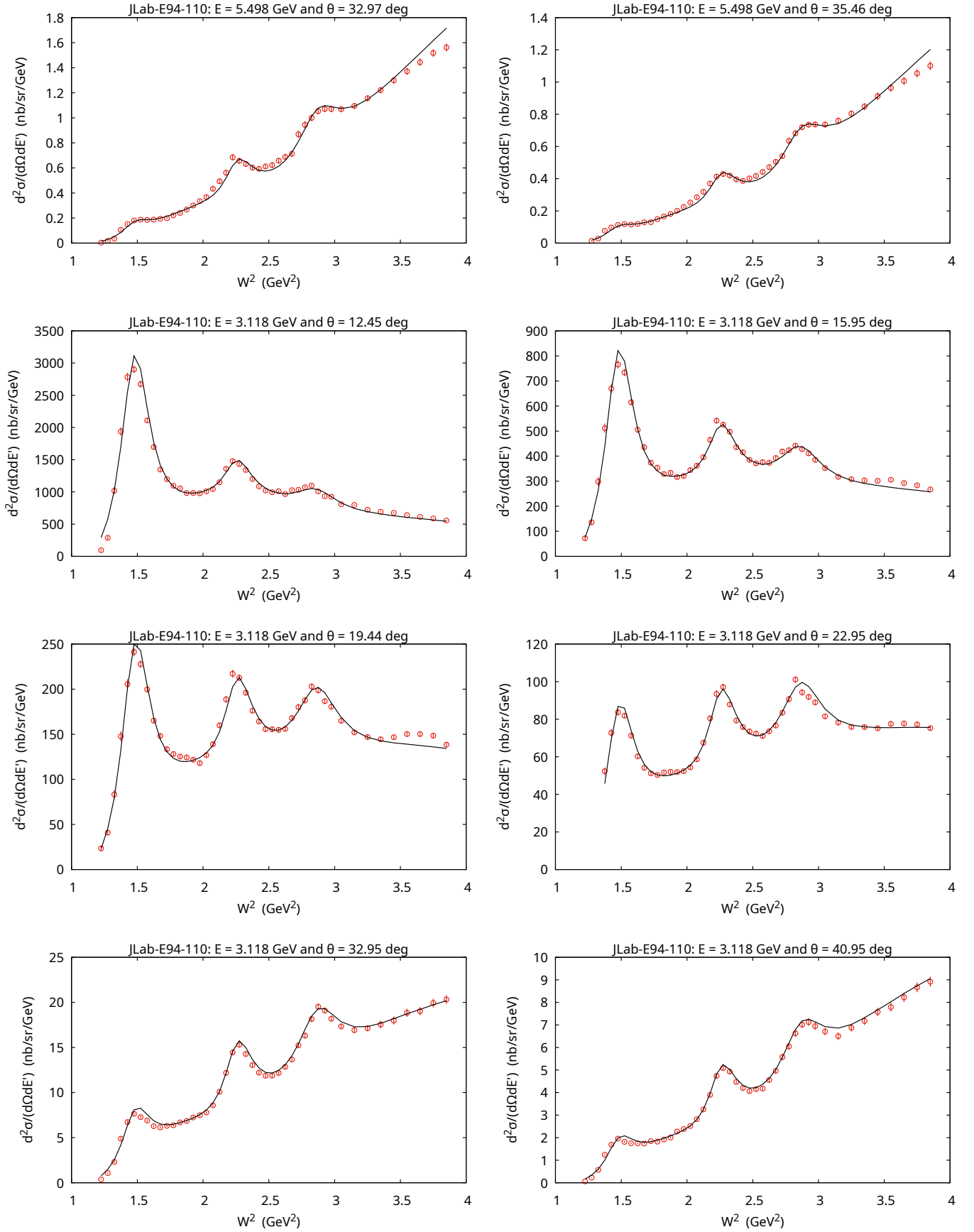


FIG. 37. Similar to Fig. 36.

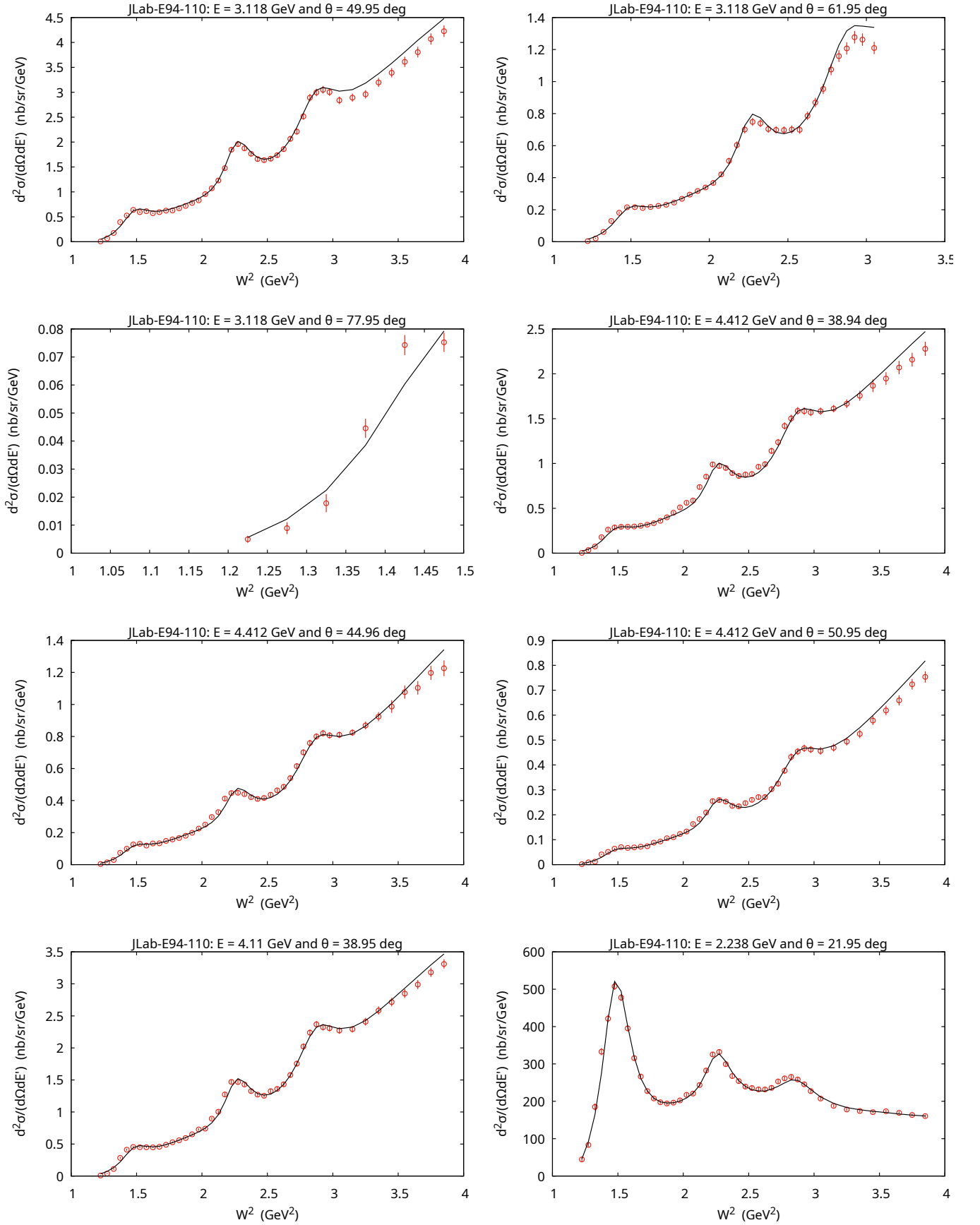


FIG. 38. Similar to Fig. 36.

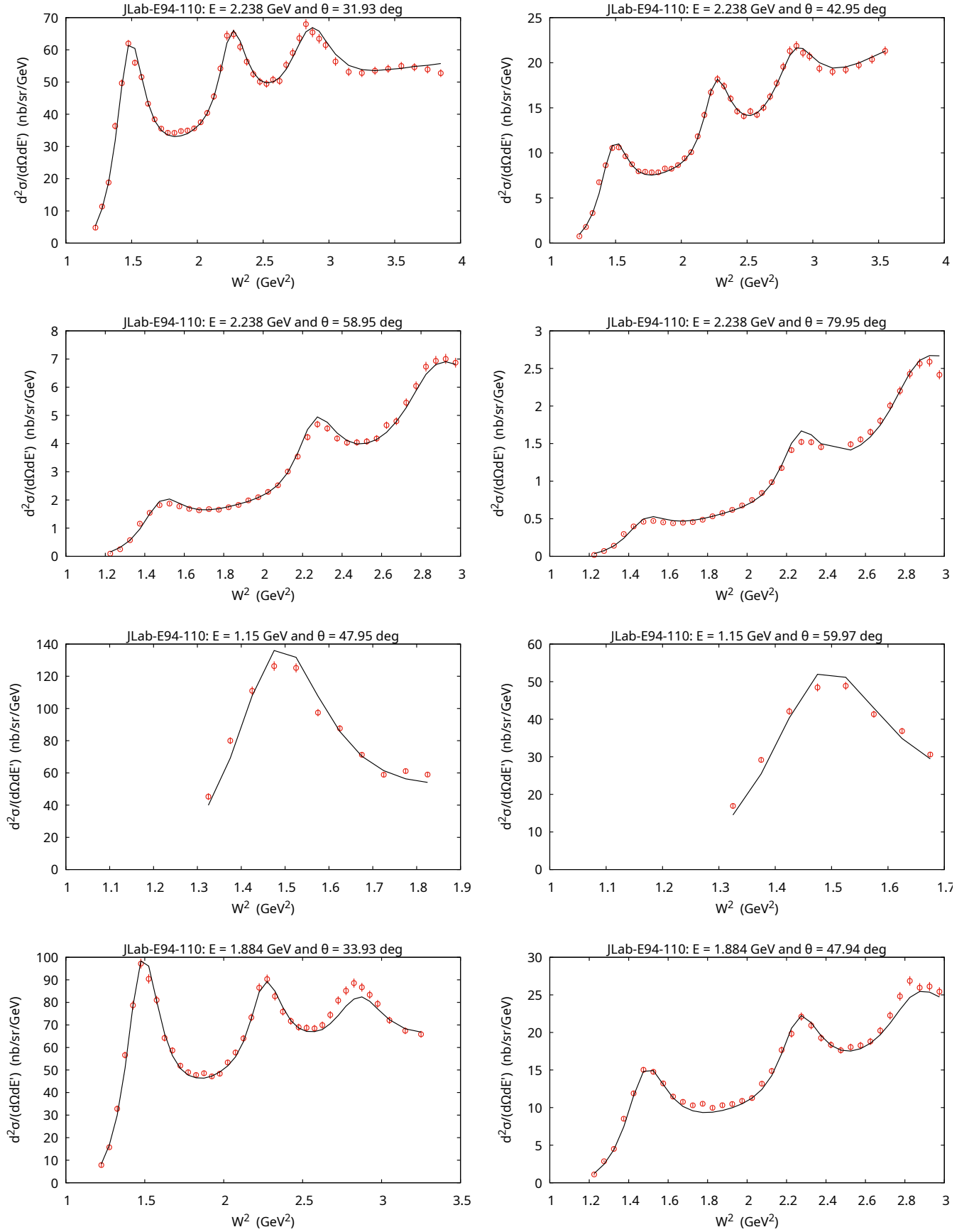


FIG. 39. Similar to Fig. 36.

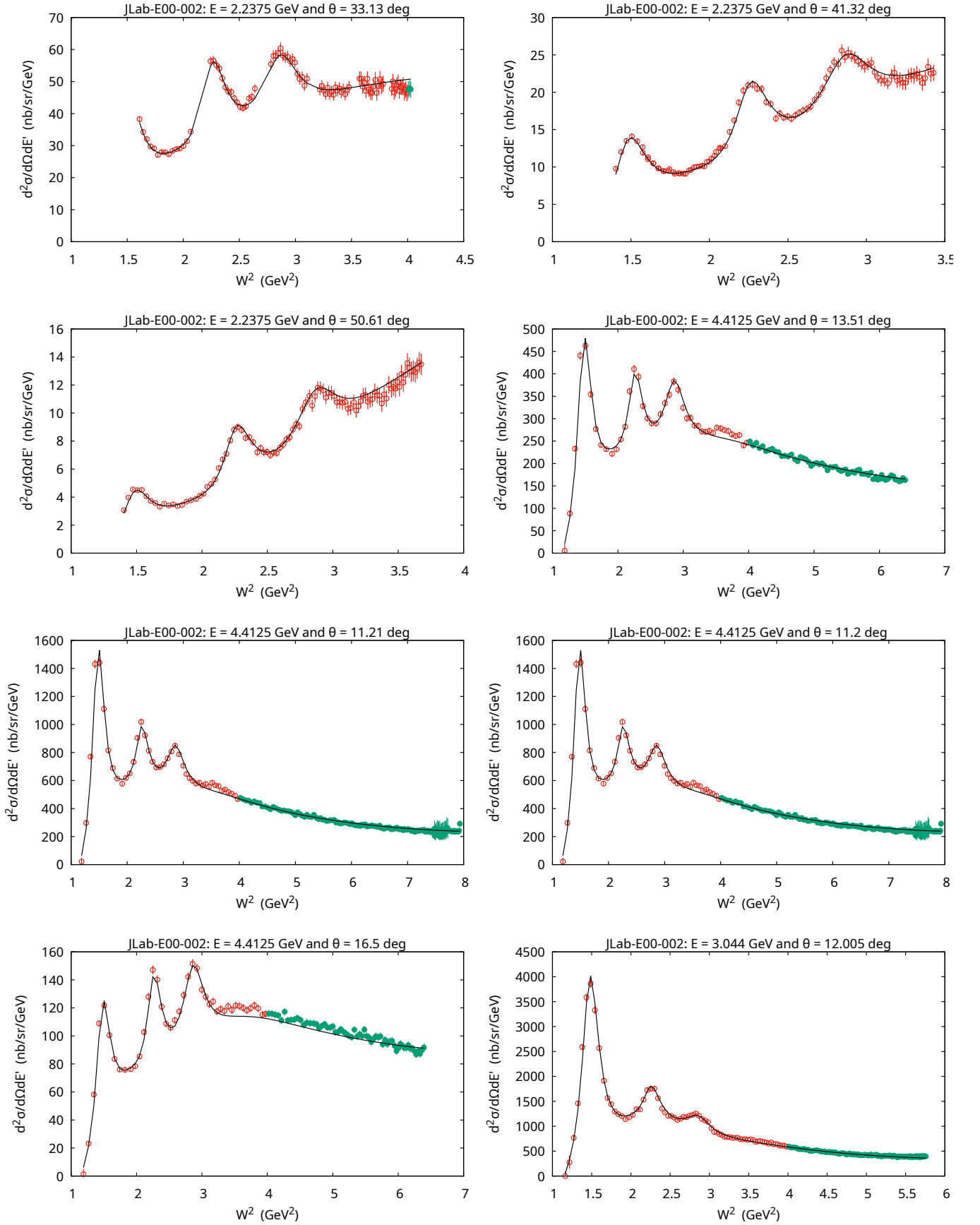


FIG. 40. Model predictions (solid line) in comparison with JLab-E00-002 data on differential cross section $d^2\sigma/(d\Omega dE')$ in nanobarn/(sr GeV) vs W^2 in GeV^2 . The values of the beam energy (GeV) and scattering angle (degrees) are given in the figure panels.

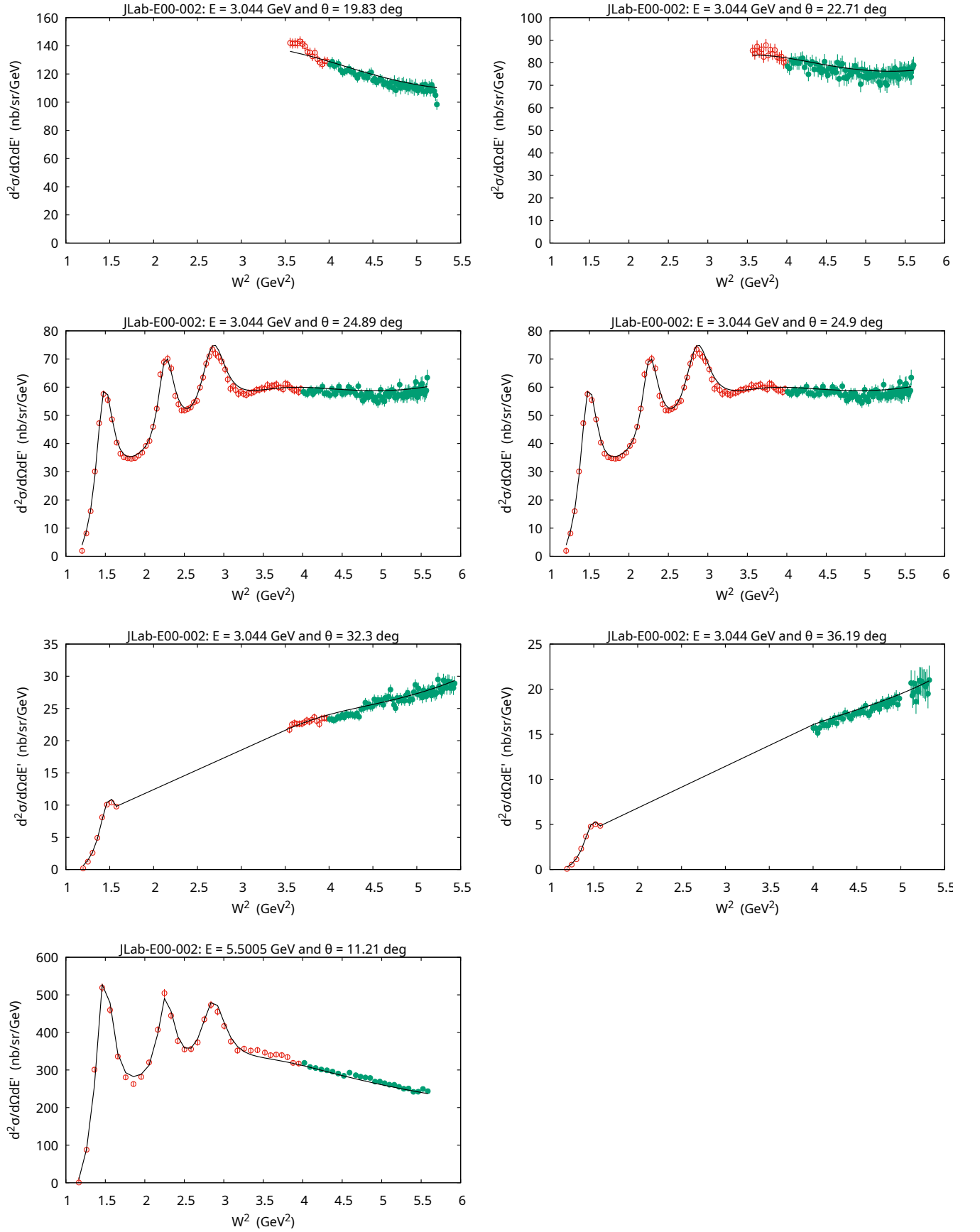


FIG. 41. Similar to Fig. 40.

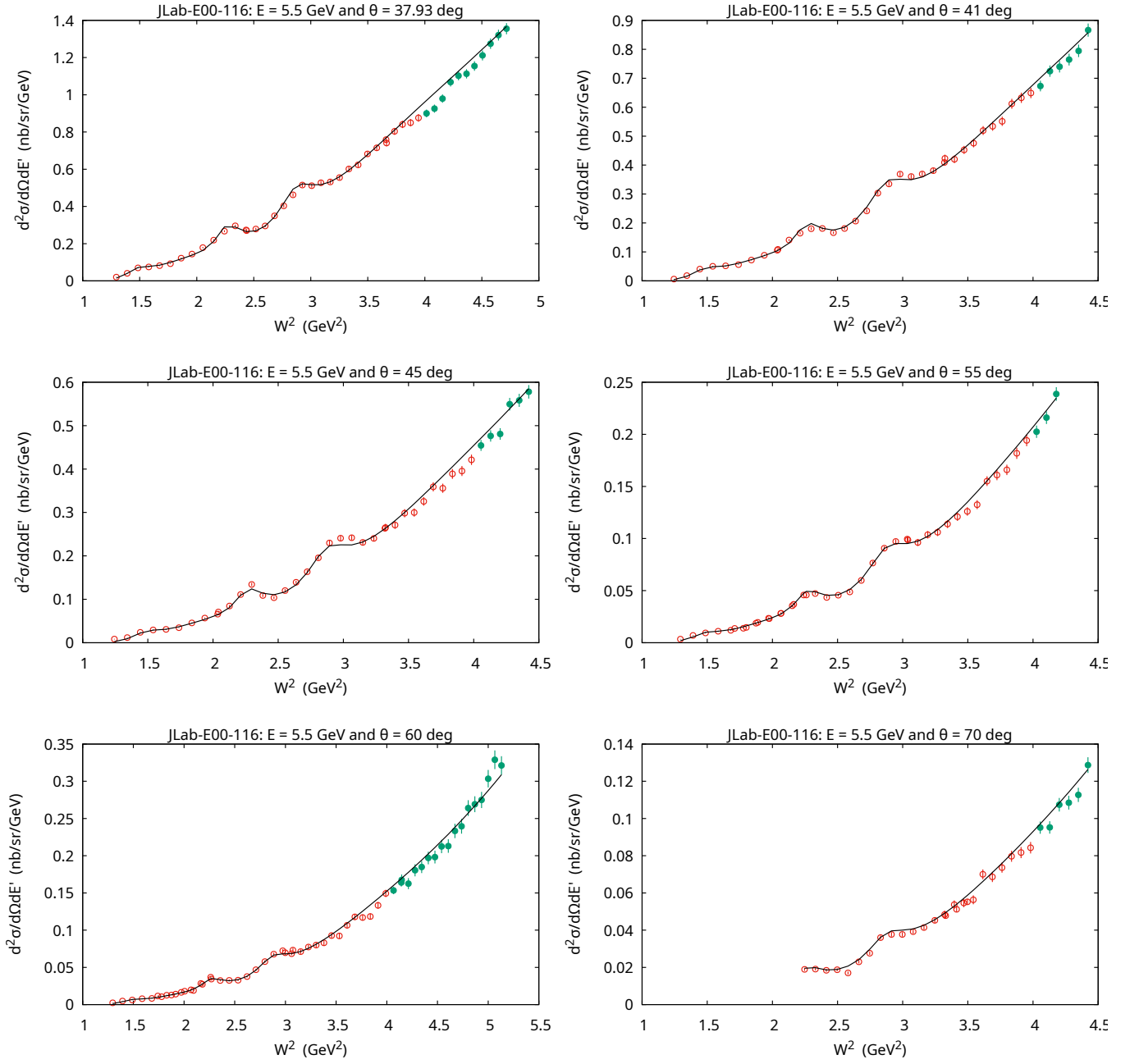


FIG. 42. Model predictions (solid line) in comparison with JLab-E00-116 data on differential cross section $d^2\sigma/(d\Omega dE')$ in nanobarn/(sr GeV) vs W^2 in GeV^2 . The values of the beam energy (GeV) and scattering angle (degrees) are given in the figure panels.